The Thesis Committee for Chiazor Nwachukwu

Certifies that this is the approved version of the following thesis:

Model Selection for Co_2 Sequestration Using Surface Deflection and Injection Data

APPROVED BY

SUPERVISING COMMITTEE:

Supervisor: _____

Sanjay Srinivasan

_____

Kamy Sepehrnoori

Model Selection for Co_2 Sequestration Using Surface Deflection and Injection Data

by

Chiazor Nwachukwu, B.S.

Thesis

Presented to the Faculty of the Graduate School of

The University of Texas at Austin

in Partial Fulfillment

of the Requirements

for the Degree of

Master of Science in Engineering

The University of Texas at Austin

August 2015

Dedication

To God.

To my family.

To my friends.

Acknowledgements

First and foremost, I would like to express my sincerest gratitude to my supervisor, Dr. Sanjay Srinivasan, for his guidance and endless support throughout the tenure of this research. His continuous inspiration and vision for this work drove me to push myself intellectually towards the completion of this project. I feel blessed to have been given the opportunity to learn from him and work under his tutelage. Many thanks to Dr. Kamy Sepehrnoori, for committing himself to reading my thesis and providing valuable feedback.

I would also like to thank the graduate coordinator for the Petroleum Engineering department, Frankie Hart, for always being available to help in whatever capacity she could. Additional thanks to Jin Lee, for her helpful administrative support.

Special thanks to Hoonyoung Jeong and Sayantan Bhowmik for their groundwork on this project, and their willingness to offer advice and provide clarity on many occasions.

I would like to appreciate my research colleagues who have all helped and motivated me throughout my graduate study: Haiyan, Baehyun, Liangping, Harpreet, Morteza, Travis, DJ, Hari, Deji, Mayuri, Henry, Kwangjin, Krupa, James, Colin, Arin, Williams and Sang.

Abstract

Model Selection for Co_2 Sequestration Using Surface Deflection and Injection Data

Chiazor Nwachukwu, M.S.E.

The University of Texas at Austin, 2015

Supervisor: Sanjay Srinivasan

In recent years, sequestration of CO_2 in the subsurface has been studied more extensively as an approach to curb carbon emissions into the atmosphere. Monitoring the fate and migration of the CO_2 plume in the aquifer is of utmost interest to regulators and operators. Current monitoring techniques like time-lapse seismic are expensive and have limited applicability. Moreover, these techniques have little predictive value unless embedded within a feedback-style control scheme.

Provided that field data such as bottom-hole pressures, well rates, or even surface deformation is available, geologic models for the aquifer can be created and used, as an input to a flow simulator, to predict the migration of CO_2. A history matching approach has been developed, within a model selection framework, to select and refine geologic models within a selected set of models until they represent the spatial heterogeneity of the target aquifer, and produce forecast with relatively small uncertainty.

An initial large suite of models can be created based on prior information of the aquifer. Predicting the response from these models however, presents a problem in terms of computational time and expense. A particle-tracking algorithm has been developed to estimate the flow response from geologic models, while significantly reducing computational costs. This algorithm serves as a fast approximation of finite-difference flow simulation models, and is meant to provide a rapid estimation of connectivity of the aquifer models. A finite element method (FEM) solver was also developed to approximate the geomechanical effects in the rock caused by the injection of CO_2. The approach used here utilizes a partial coupling scheme to sequentially solve the flow and geomechanical equilibrium equations.

The validity of the proxies is tested on both 2D and 3D field cases, and the solutions are shown to correlate reasonably well with full-physics simulations. We also demonstrate the application of the model selection algorithm to a 3D reservoir with complex topography. The algorithm includes three main steps: (1) predicting the flow and geomechanical response of a large prior ensemble of models using the proxies; (2) grouping models with similar responses into clusters using multidimensional scaling together with a k-means clustering approach; and (3) selecting a model cluster that produces the minimum deviation from the observed field data.

The model selection procedure can be repeated using the sub-group of models within a selected cluster in order to further refine the forecasts for future plume migration. This entire iterative model selection scheme is demonstrated using the injection data for the Krechba reservoir in Algeria, which is an active site for CO_2 sequestration.

Table of Contents

List of Tables

List of Figures

CHAPTER 1: INTRODUCTION

1.1 Motivation

Increased concern about anthropogenic global climate change has sparked interest in developing methods to curb greenhouse gas emissions into the atmosphere. CO_2 capture and storage is emerging as a viable means to reduce emissions of greenhouse gases. To investigate the large-scale feasibility of this method, field scale projects have been undertaken in regions across the world, including Algeria, the North Sea and the US [Bhowmik, 2012]. To evaluate the feasibility of CO_2 sequestration, we must examine the mechanical integrity of the aquifer under long-term injection of CO_2. Impact of injection on rock deformation, potential leakage from the subsurface, and predicting the eventual destination of the CO_2 plume are areas of particular concern to regulating agencies. Current techniques to monitor the migration of CO_2 (such as time-lapse seismic) only offer information about the instantaneous position of the plume and have no predictive value unless combined with a reservoir model updating scheme and flow modeling. There is consequently a need to incorporate measurements such as seismic data, remote sensing information and routinely measured injection pressure and rate information in a scheme to create and update geologic models that can be used for predicting CO_2 migration in the subsurface. One way to accomplish this is by history matching. History matching is the process of calibrating reservoir models such that they show the best match to available dynamic information [Bhowmik, 2012]. In contrast to traditional model perturbation schemes that can be quite inefficient when attempting to integrate information from multiple sources, an model selection is presented that utilizes diverse information in order to select a subset of models that reflect the observed dynamic characteristics and reduces the uncertainty in forecasts of plume migration.

1.2 Research Objectives

The primary goal is to develop fast approximations (proxies) for the flow and geomechanical response of reservoirs/aquifers subject to injection of CO_2 for sequestration. These proxies are to be used within a model selection algorithm. More specifically, the work presented focuses on achieving the following objectives:

1. Development of a particle tracking proxy to estimate the flow response.
2. Development of an FEM solver to estimate rock deformation.
3. Development of a module to couple the flow and geomechanics proxies and share information between the two solvers in a fully automated manner.
4. Development of a program to cluster the proxy solutions based on response similarities.
5. Full-physics solutions for cluster representatives and selection of a best-fit cluster.

1.3 Thesis Outline

This thesis will include an in-depth description of the model selection algorithm, the development of the flow and geomechanical simulation proxies that were used, and applications of the overall framework to 2D and 3D reservoirs.

Chapter 2 will discuss research work presented in literature as it pertains to methods for assimilating data in subsurface models, as well as existing methods to approximate the flow and geomechanical response of reservoirs. In this chapter, we also explore the different options for coupling between flow and geomechanics simulators.

Chapter 3 presents an introduction into model selection, its individual components, and how these components are integrated to make up the overall framework.

Chapter 4 describes the development of the particle tracking proxy used to approximate full-physics flow simulations. Test cases using 2D and 3D grids will be presented and compared to solutions from the CMG simulator.

Chapter 5 will focus on the development of the FEM solver used to approximate the rock deformation. The mathematical formulation will be discussed, and a computational implementation scheme will be described. This chapter ends with a presentation of verification cases in 2D and 3D reservoirs.

Chapter 6 will demonstrate the application of the full model selection framework to a synthetic reservoir that exhibits complex topography. The effectiveness of the algorithms and procedures will be demonstrated in terms of the improvement in accuracy of prediction of plume migration and the reduction in uncertainty accomplished post-model selection.

Chapter 7 will demonstrate the application of the model selection scheme to a field case, using data and observations from the In Salah CO_2 storage project in Algeria.

Chapter 8 summarizes the key findings of this research.

CHAPTER 2: LITERATURE REVIEW

This chapter presents a review of literature pertaining to established history matching and parameter estimation techniques, implementation of proxies for flow simulation, and methods of coupling flow and mechanical effects in geomechanics simulation. Special emphasis will be placed on CO_2 injection, and the particular techniques that were used for this project - model selection, particle tracking proxies, and partial coupling of flow and geomechanics.

2.1 History Matching

Efficient management of reservoirs requires geologic models that can provide reliable forecasts of future production as well as precise estimates of prediction uncertainty. Reliable forecasts depend on an accurate description of reservoir geology, represented largely by the spatial distributions of permeability and porosity used for simulation. Since these variables cannot be known exhaustively throughout the reservoir, they must be inferred indirectly using reservoir responses such as pressures and flowrate, and using parameter estimation procedures such as history matching or Bayesian estimation [Jafarpour, 2008]. History matching can be described as the process of updating representations (models) of the subsurface region under study, such that forecasted simulations of these representations are a close match to observed field data. The critical assumption in this process is that if the simulated results match the observed data, the model is deemed a close enough approximation to the actual subsurface reservoir and can thus be used to reliably predict future performance [Bhowmik, 2014]. In the next subsections, we will present some traditional history matching techniques that have been used to refine reservoir properties.

2.1.1 Gradual Deformation

Gradual deformation is a traditional history matching technique, introduced by Hu in 2000, in which the modeler seeks to create gradual, continuous perturbations of a prior model realization, such that the perturbations produce output that better match some reference data [Caers, 2007]. The basis for this technique is the exploitation of a well-known property of Gaussian variables: a standard Gaussian variable X can be written as the linear combination of two or more standard Gaussian variables X_i and X_{i+1} to form the relationship [Johansen, 2008]

$$X = \sum_{i=1}^{N} w_i X_i, \tag{2.1}$$

where the subscript *i* denotes the *i*th realization, *N* is the total number of realizations, and w_i is a weighting factor assigned to X_i.

Hu [2000] proposed that if the realizations X_i all have the same variogram, then the variogram will be conserved if the following constraint is met

$$\sum_{i=1}^{N} {w_i}^2 = 1. \tag{2.2}$$

It's easy to realize that if the perturbation is formed from two prior realizations, Equation 2.1 must take the form

$$X = X_1 \cos(p) + X_2 \sin(p), \tag{2.3}$$

where *p*, called the deformation parameter, can take on any value, and is used to deform the resulting realization. For $p = 0$, X will be equal to X_1, and for $p = \pi/2$, X will be equal to X_2. That is, the chosen value of p results in a perturbation that is some combination of the prior realizations [Johansen, 2008]. As p is "gradually" increased from zero, the outcome X will slowly become different from X_1; likewise, as we approach the limit case $p = \pi/2$, the outcome gradually becomes X_2 [Caers, 2007]. In the context relevant to this work, the

variable X would be a spatially distributed property of the reservoir, such as permeability or porosity.

As explained above, the gradual deformation technique provides a way to generate equiprobable realizations of a Gaussian distributed field. The technique can be used in the formulation of a history-matching problem of the form [Johansen, 2008]

$$k = Argmin[E(k)], \tag{2.4}$$

where *k* represents the permeability field, and *E* is an objective function to be minimized that quantifies the error in the matched data. Recall that from Equation 2.1, the permeability field can be represented by a vector of deformation parameters and a set of equiprobable prior models. Since the permeability fields will be generated by a geostatistical simulator and are fixed, the only parameter to be adjusted is the vector of deformation parameters [Johansen, 2008]. The history-matching problem is thus reduced to a search for optimum deformation parameters that minimize the data mismatch.

$$p = Argmin[E(p)]. \tag{2.5}$$

2.1.2 Probability Perturbation

Probability perturbation is a stochastic search algorithm introduced by Caers in 2003 and further developed by Kashib and Srinivasan in 2003 as a method to integrate dynamic data into the construction of geologic models. This method exploits the algorithmic structure of sequential simulation, and can be applied to history matching of reservoirs with complex geology [Johansen, 2008]. In sequential simulations, an unknown property at a grid node is determined by sampling from a locally constrained probability function, $P(A|B)$ where A is the outcome to be simulated and B represents the data in the neighboring grid nodes. Secondary data can be incorporated into the simulation to further condition the outcome of a realization. $P(A|C)$ denotes the probability of an outcome conditioned to the secondary information. We can combine two conditional probabilities using the τ-model [Journel, 2002]

$$\frac{x}{a} = \left(\frac{b}{a}\right)^{\tau_1} \left(\frac{c}{a}\right)^{\tau_2}, \tag{2.6}$$

where

$$x = \frac{1 - P(A|B,C)}{P(A|B,C)},$$

$$b = \frac{1 - P(A|B)}{P(A|B)},$$

$$c = \frac{1 - P(A|C)}{P(A|C)},$$

$$a = \frac{1 - P(A)}{P(A)}. \tag{2.7}$$

In the probability perturbation method, τ_1 and τ_2 are typically set equal to 1 [Caers, 2007]. If we set $\tau_1 = \tau_2 = 1$, we can reconstruct the above equations to give

$$P(A|B,C) = \frac{1}{1+x} = \frac{a}{a+bc}\,. \tag{2.8}$$

From a history matching perspective, we can incorporate the data mismatch as secondary information during simulation using the following expression [Caers, 2003; Kashib and Srinivasan, 2003; Johansen, 2008]

$$P(A|C) = (1 - r_c)i + r_c P(A), \tag{2.9}$$

where C in this case represents the production data, i denotes a realization of binary variables for a certain property (say facies), and r_c is a free parameter. We can thus repeat the sequential simulation, this time conditioned to $P(A|C)$. When r_c is equal to 0, the perturbed realization will be identical to i. If r_c is equal to 1, the conditional probability becomes the unconditional probability $P(A)$, and the simulation will result in a new realization equiprobable to i. When r_c is between 0 and 1, the simulation results in a realization that is a mix between i and another equiprobable realization [Johansen, 2008]. We can therefore assume r_c to be a free parameter that dictates the production data, and consequently the data

mismatch [Caers, 2007]. The optimum choice of r_c is that which minimizes the production data mismatch.

2.1.3 The Ensemble Kalman Filter (EnKF)

The ensemble Kalman filter (EnKF) is an effective method for reservoir history matching. Developed by Evensen [1994], it is a process for updating the state variables of a system, by progressively integrating any available data [Bhowmik, 2014]. The underlying principle is that an initial ensemble of stochastic models can be used to compute the covariance (sensitivity) between the state variables (permeability, fluid saturation etc.) and the observed dynamic response and this sensitivity can be subsequently used to update the models using measured responses as they become available [Tavakoli et al., 2013]. These measured values could be bottom-hole pressures, well rates, or surface deformation. In a review paper, Aanonsen et al. [2009] present a summary of EnKF applications for history matching in reservoir engineering. Naevdal [2003] summarizes the steps involved in EnKF:

1. Create an initial ensemble of models. Define the state variables – static variables such as porosity and permeability as well as dynamic variables such as saturations and pressures.
2. Run forward full-physics simulation to the first update step when observations are available.
3. Create a correlation matrix that relates the state variables to the corresponding simulated responses.
4. Compute the mismatch between the simulated responses and the actual well observations.
5. Update the state vector, guided by this mismatch.

6. Run the models forward using the updated state vector, to the next timestep when observations are available.
7. Repeat steps 3-5 until the end of the time-record is reached.

When applying EnKF to nonlinear history-matching problems, we consider the vector of reservoir model parameters, such as porosities and permeabilities, m, the vector of state variables, such as pressures and saturations, p^n, and the vector of predicted data, d^n, to make up an augmented state vector, y^n [Tavakoli et al., 2013; Evensen 2007, 2009]. The simulated well responses that have to be compared to the observation data can be extracted from this state vector by applying the transformation

$$d^n = \boldsymbol{H} y^n, \tag{2.10}$$

H is a binary matrix with identity values corresponding to the well response locations. The EnKF update equation for each ensemble member j is then given by [Tavakoli et al., 2013]

$$y_j^{n,a} = y_j^{n,f} + C_Y^{n,f} H^T \left(H C_Y^{n,f} H^T + C_{D^n}\right)^{-1} \left(d_{uc,j}^n - d_j^{n,f}\right). \tag{2.11}$$

Here, $C_Y^{n,f}$ denotes the covariance matrix of the forecast state vector $y_j^{n,f}$; $d_{uc,j}^n$ is a sample from the normal distribution N(d_{obs}^n, C_{D^n}); d_{obs}^n represents observed data; and C_{D^n} denotes the data covariance matrix at time *n*. The superscript f denotes the forecast or predicted data, the superscript *a* denotes the assimilation step, and the superscript *uc* denotes an unconditional perturbation of observed data.

EnKF is an attractive option for model updating, however, it has some major drawbacks:

The implementation of EnKF requires that the relationships between the state variables be defined in a covariance matrix. The covariance function can adequately represent

the multivariable relationships only if the state values exhibit a Gaussian nature [Bhowmik, 2014]. Another caveat is that the relationship between the state variables and observation data must be linear. EnKF is ineffectual for representing the posterior probability when the data is bi-modal [Zafari, 2007]. For non-Gaussian state variables, Emerick [2012] proposed the combination of EnKF with efficient sampling techniques, such as MCMC (Markov Chain Monte Carlo), to ensure proper sampling of the reservoir parameters in the posterior distribution. This process is however time consuming due to the iterative nature of MCMC [Bhowmik, 2014].

Moreover, it has been shown by several authors that in EnKF, because of the sequential nature of the algorithm, the history matches at prior time steps progressively get violated with the assimilation of subsequent data. As a result, several authors (Tavakoli, et al. 2013) propose an iterative implementation of EnKF whereby the prior history matches are re-assessed when the models are updated and the updates resulting in least deviation from the observed history over all time-steps are retained. This render the EnKF to be computationally expensive and motivates the development of fast approximations to predict the responses for all models in the ensemble.

2.1.4 Model Selection

It is often necessary to develop not just a single model, but a suite of equiprobable models that captures the variability of the reservoir and the uncertainty associated with describing it, based on current information. As discussed in the previous section, history matching based on performing grid-node updates to reservoir parameters and subsequently repeating that process to develop multiple reservoir models, can be computationally expensive and sometimes impractical. It is thus useful to interpret the process of history matching as an effort to find the most suitable candidates for the reservoir under study based

on the observed responses. That is, history matching becomes a process to select best-fit models for the reservoir [Bhowmik, 2014].

The process starts with an initial large ensemble of reservoir models that reflect the prior uncertainty in reservoir description, including all plausible geologic scenarios. These models are presumed to be conditioned to the available static data. In the absence of production data all prior reservoir models are equally probable, thus the model selection algorithm is applied to select a few reservoir models that are more consistent with the observed production characteristics [Mantilla and Srinivasan, 2011]. A quick assessment of the models must then be performed to evaluate their dynamic characteristics and flow connectivity. Usually, this involves estimating the shape of the CO_2 plume, or the vertical displacement at the top of the reservoir. A method is then implemented to group the models into clusters, based on similarities in the estimated responses. The posterior model set is chosen as the cluster that produces the minimum deviation from the observed field data.

Given that the end product of model selection is a small set of equiprobable models (posterior models that are more representative of the reservoir than the prior larger population of models), the residual uncertainty associated with the prediction of future performance can be quantified using the simulated forecasts from these posterior models. Therefore, this algorithm provides a probabilistic approach to assessing the migration of the CO_2 plume in the aquifer and quantifying the risk associated with sequestration projects. This scheme was applied by Singh in 2012, and by Singh and Srinivasan in 2013. The model selection scheme used by Bhowmik [2014] is illustrated in Figure 2.1. The entire process is described in detail in Chapter 3.

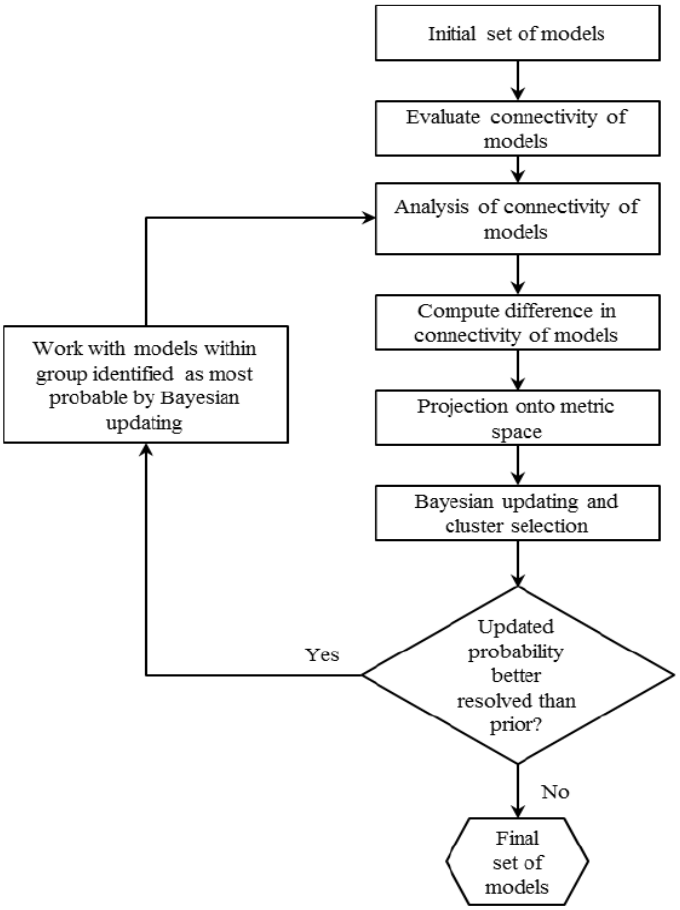

Figure 2.1: Schematic of the model selection algorithm used by Bhowmik [2014]

2.2 Implementation of Proxies for Flow Simulation

Typically, reservoir simulation requires a numerical solution of the mass and momentum balance equation that define flow in porous media. Recent innovations and advancements in computing technology have facilitated the use of full-physics simulators to produce production forecasts for oil and gas reservoirs. However, as detailed in the previous section, the model selection algorithm requires solutions for numerous models in the prior ensemble. The computational time required to produce these forecasts makes it impractical to employ a full-physics simulator for this task. Therefore, our objective is to address this problem by replacing commercial simulators with a proxy that can produce estimates with

reasonable accuracy. This section discusses two existing methods of proxy formulations that have been implemented prior to this project.

2.2.1 Connectivity Analysis

Hirsch and Schuette [1999] utilized principles of graph theory to quantify the connectivity of reservoir models. Their method quickly approximates the fluid migration paths in the reservoir under consideration. In this scheme, the connections between grid blocks are represented using edges; each edge is then assigned an "edge weight", calculated by parameters that influence reservoir connectivity, such as permeability and porosity [Jeong, 2014]. Once the edge weights for the entire flow grid have been calculated, breakthrough times are then assigned to each grid block based on the shortest path (in terms of edge weights) from the injector. Fluid migration is simulated by filling up the pore volume of the grid blocks, proceeding from smaller breakthrough times to larger ones.

2.2.2 Particle Tracking

Particle tracking algorithms have been used in tracer flow simulations as useful alternatives to full-physics solvers. This approach relies on replacing the moving fluid in a reservoir by moving particles through a grid. The particular particle tracking approach used here is random walker particle tracking (RWPT). As opposed to combining convection and physical dispersion into a single equation, RWPT moves the particles using an underlying velocity field, and adds uncertainty to represent dispersion. Bhowmik [2014] implemented an RWPT strategy that stochastically moves the particles according to a calculated transition probability distribution. The target grid block to which movement occurs is established by performing a Monte Carlo sampling of the transition probability distribution. This process is repeated until a stopping criterion has been met for all particles in the flow grid. Detailed formulation of this algorithm is given in Chapter 4.

2.3 Accounting for Geomechanical Effects

Geomechanical effects induced by reservoir production or injection can be particularly pronounced in stress-sensitive reservoirs, such as weakly compacted and fractured reservoirs [Longuemare et al., 2002]. While the majority of reservoirs are located in stable rock formations that do not undergo significant deformation, there are many reasons to investigate coupled flow and geomechanics. Coupled flow and stress calculations are useful for predicting well failures and guiding well product and placement; reservoirs may also experience "settling" during production [Minkoff et al., 2003]. Frequently, the geomechanical effects are approximated in a conventional reservoir simulator through the rock compressibility term. However, the stresses in the reservoir and surrounding rocks may not be in equilibrium with the pore pressure, if the geomechanical behavior is not considered.

The ideal solution for modelling the coupled flow and geomechanical response of reservoirs is to introduce the geomechanical effects through the stress analysis solution and to implement a scheme that assures that the governing laws of flow simulation and stress analysis are obeyed simultaneously at each time step [Inoue and Fontoura, 2009]. However, this renders the computation scheme difficult and in many cases intractable because the flow and geomechanical behaviour manifest at different time scales. Therefore there are different degrees to which coupling between the flow and geomechanics models may be implemented. The degree of coupling may affect the accuracy of the solution as well as the computational efficiency; therefore, trade-offs may be made to optimize simulation times [Settari and Walters, 2001]. To understand how the different degrees of coupling are implemented, let us first consider the general formulation of the coupled problem. After space-time discretization, the coupled problem can be written as [Settari and Walters, 1999]

$$\boldsymbol{K}\Delta_t u + \boldsymbol{L}\Delta_t p = F\ , \tag{2.12}$$

$$\boldsymbol{L}^T \Delta_t u + \boldsymbol{E} \Delta_t p = R \,. \tag{2.13}$$

Equation 2.12 accounts for the geomechanical equilibrium whereas Equation 2.13 accounts for the fluid mass balance equation. Here, $\boldsymbol{K}$ is the stiffness matrix, $\boldsymbol{L}$ is the coupling matrix between mechanical and flow unknowns (here, displacement and pore pressure), F is the vector of force boundary conditions, $\boldsymbol{E}$ is the flow matrix, and R is the source term for the flow problem. The decomposition $\boldsymbol{E} = \boldsymbol{T} - \boldsymbol{D}$ is used where $\boldsymbol{T}$ is a symmetric transmissibility matrix and $\boldsymbol{D}$ is the accumulation diagonal matrix. Finally, Δ_t represents a change in time such that $\Delta_t u = u^{n+1} - u^n$ and $\Delta_t p = p^{n+1} - p^n$ where n is the index of time discretization. To simplify the presentation, the stiffness matrix $\boldsymbol{K}$ and the flow matrix $\boldsymbol{E}$ are considered here to be linear operators. In general, however, $\boldsymbol{K}$ and $\boldsymbol{E}$ can be nonlinear operators accounting for nonlinear elasticity [Longuemare et al., 2002].

2.3.1 Full Coupling

In the fully coupled approach, the flow and geomechanics system of Equations 2.12 and 2.13 are solved simultaneously using the same discretization, by either the finite-difference method or the finite-element method. The fully coupled approach has the advantage of internal consistency [Settari and Walters, 2001]. The problem with full coupling however, is that it has very high computational costs and more importantly, the issue of tractability because of the disparate time-scales of the flow and geomechanics phenomena.

2.3.2 Partial Coupling

A variety of partial coupling approaches have been developed to circumvent the high computational expense of full coupling. In the partially coupled approaches, the geomechanics and flow equations are solved separately and sequentially, usually with two different simulators each implemented with a optimum discretization scheme, and

information is exchanged between the simulators at least once every common timestep [Settari and Walters, 2001]. Generally, the fluid flow problem is solved based on the finite-difference method, while the stress equilibrium equation is solved using a finite-element model [Amirlatifi, 2013]. Starting with the flow equation, we can solve for the pressure at the next timestep assuming fixed displacements

$$[\boldsymbol{T} - \boldsymbol{D}]\Delta_t p = R - \boldsymbol{L}^T \Delta_t u \,. \tag{2.14}$$

Then, using the pressure solution, the displacements can be solved by

$$\boldsymbol{K}\Delta_t u = F - \boldsymbol{L}\Delta_t p \,. \tag{2.15}$$

One major benefit of this method is that it profits from the best solver approach for each phenomenon (flow and geomechanics). Several proofs for convergence of the iterative coupling approach exist [Settari and Mourits, 1998; Longuemare et al., 2002; Settari and Walters, 2001] for various boundary conditions and solver schemes. As will be seen in Chapters 4 and 5, we employed the use of a particle tracking proxy to solve the flow equation, and developed an FEM solver for the stress problem. The reduced computational cost associated with a partial coupling scheme makes it an attractive option for use in this study. The partial coupling scheme can be further divided into two subdivisions: one-way and iterative (two-way) coupling. Figure 2.2 shows the scheme for one-way and iterative partial couplings.

One-way coupling

In the one-way coupling approach, a reservoir simulator carries out fluid flow calculations at each timestep; however stress-displacement calculations are only carried out at coarse timesteps, depending on the magnitude of pore pressure and pore space changes. That is, if the difference in pore volume over a certain time step is not substantial, the time step

size is increased. Once the change in pore volume exceeds a threshold, the stress-displacement analysis is carried out [Amirlatifi, 2013; Minkoff et al., 2003; Settari and Walters, 1999] and the resultant displacements feed-back into the flow equations. This approach can significantly reduce the computational cost of the coupled analysis through reduced number of stress-displacement simulation runs, but may result in unstable solutions and loss of accuracy due to the coupled nature of the processes [Amirlatifi, 2013; Dean et al., 2006].

Iterative coupling

This method consists of repeatedly solving the flow and stress equations in sequence during each timestep until convergence is reached. In this scheme, the coupling parameters are exchanged between simulators multiple times at each timestep. At convergence, this method becomes equivalent to a fully coupled approach. Settari and Mourits [1998] demonstrate the use of an iterative coupling approach to problems involving flow in porous media. Mikelic and Wheeler [2012] formally proved the convergence of this scheme to the fully coupled solution.

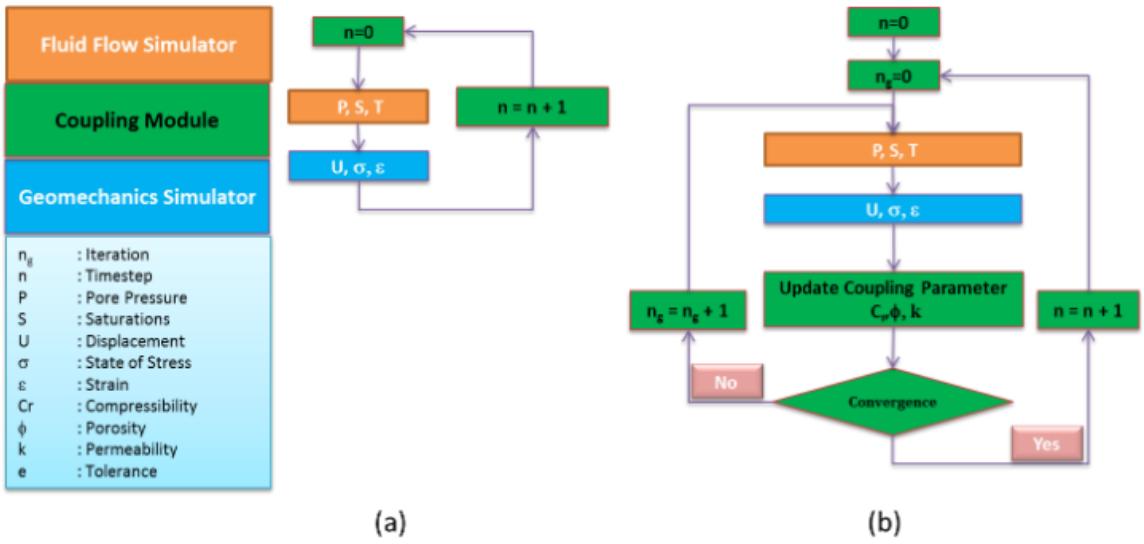

Figure 2.2: Partial coupling techniques: (a) One-way coupling (b) Two-way coupling [Amirlatifi, 2013]

2.4 Chapter Summary

In this chapter we presented relevant literature concerning established techniques of history matching, the implementation of proxies for the quick estimation of the flow response and methods of coupling between flow and geomechanics simulations. In Chapter 3, we will introduce, in exhaustive detail, the model selection scheme and the individual components that constitute the algorithm.

CHAPTER 3: THE MODEL SELECTION ALGORITHM

In reservoir modeling, it is often desired to tweak a set of geologic or numerical models such that the predicted output matches closely with the observation data; this process is called history matching. In model selection on the other hand, instead of iteratively perturbing the reservoir model to best-fit the available dynamic data, a small suite of best-fit models are selected from a much larger prior ensemble using the dynamic data as a guide. This algorithm ensures that the selected models have some common geologic characteristics, thus reducing the uncertainty in the forecast. The steps undertaken during model selection are detailed as follows:

1. **Generate an ensemble of stochastic models.**

   This is a crucial step in the model selection process. It is essential that the initial ensemble of models represent the prior uncertainty associated with the reservoir under question. That is, the set of models should consider all possible variations in interpretations and depositional scenarios conditioned to the reservoir specific information such as well logs, core information etc. To illustrate the importance of prior variability, consider the realizations shown for the fluvial system in Figure 3.1. There is uncertainty associated with the channel locations, channel orientation and the facies distribution within the individual distributaries. To represent this uncertainty, the initial model set would need to include the various possible channel layouts and distributions.

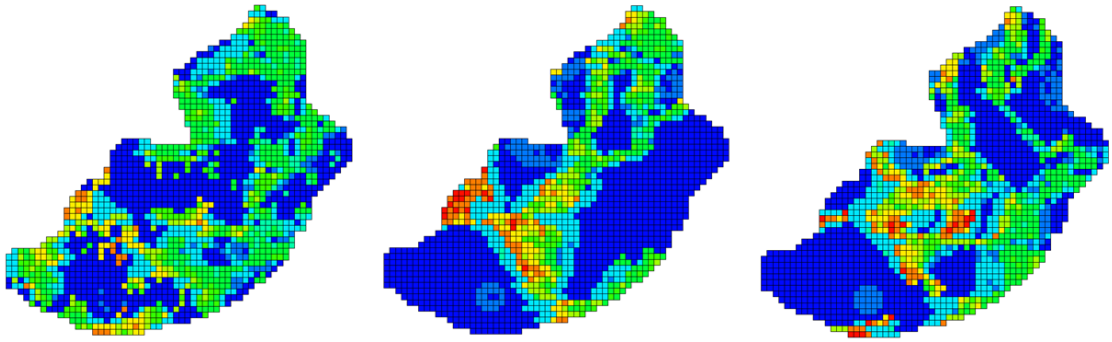

Figure 3.1: Multiple realizations showing various possible layouts of channel and facies distribution for the same slice of a reservoir model

2. **Predict the flow and geomechanics response.**

   The next step is to evaluate the flow connectivity and structural behavior of the models. Having specified well locations and CO_2 injection rates, the flow and geomechanics equations can be solved for each model in the ensemble. Ideally, a full-physics simulator would be best served for this purpose; however, the computational cost of performing such calculations for numerous models necessitate the substitution of a full-physics simulator with a fast approximation (proxy). For this work, we developed a particle tracking proxy to solve the flow problem and an FEM solver for the geomechanics problem. The goal in this step is to rapidly estimate the response from each model so that we can group models that exhibit similar responses into clusters. The responses predicted using the proxy serve as a means for characterizing the flow connectivity and structural behavior of the models.

3. **Project the model responses onto a reduced dimensional space**

   The difference between the responses of pairs of models is non-metric and consequently the models cannot be grouped on the basis of distance from each other. Before the models can be grouped into clusters, the model responses must be projected into a lower dimension metric space, such that a cluster can be represented

as a set of model responses enclosed within a defined region in space. To resolve this problem, we invoked an established technique called multidimensional scaling.

Multidimensional Scaling

The objective of multidimensional scaling is to transform observations from a non-metric space into a metric space such that we can be able to provide a visual representation of the proximity between the observations. Usually, this involves the computation of metric distances, or a dissimilarity array between the observations. In this work, we have chosen the Euclidean metric space as our target space. Given an m-by-n matrix of responses whose rows correspond to m individual models and whose columns contain n simulated responses, a dissimilarity array of Euclidean distances between each pair of models can be computed. Consequently, the size of this dissimilarity array is given by (m-1) + (m-2) + (m-3) + … + 2 + 1 = m*(m-1)/2. It should be noted that the columns in the response matrix could include a combination of outputs like surface deformation and saturations, and in such a case the original dimensionality will be increased. Having computed the dissimilarity array, our objective is to select points on a lower dimensional space such that models with smaller dissimilarities between them are perceived to be closer to each other in space.

In mathematical terms, this requires an optimization algorithm that minimizes the error between the pairwise dissimilarities in the original and transformed dimensions. Kruskal [1964] showed that this optimization problem involved the minimization of a stress function given by Equation 3.1

$$Stress = \left[\frac{\sum_{i,j}\left(d_{i,j} - \delta_{i,j}\right)^2}{\sum_{i,j} {d_{i,j}}^2}\right]^{\frac{1}{2}}, \qquad (3.1)$$

where, $d_{i,j}$ represents pairwise distances between points in the transformed space, and $\delta_{i,j}$ represents the corresponding dissimilarities in the original space.

For a better understanding of the concept of multidimensional scaling, we present an example in Table 3.1. Consider the stress tensor response at some node at the same location in four different models lettered A, B, C, and D. Since the stress tensor contains 6 unique elements, the solution for each model can be represented by six observations. There is no way to visualize, or gauge the proximity in space between the model responses, as they do not yet belong to any defined metric space.

Table 3.1: Stress tensor components for a specified node at the same location in four different models lettered A to D

	σ_{xx}	σ_{yy}	σ_{zz}	σ_{xz}	σ_{xy}	σ_{yz}
A	9.474	-3.293	-6.908	4.352	1.362	-2.712
B	10.144	-7.869	3.206	5.7	-7.523	-5.098
C	7.509	-0.787	5.686	5.752	-1.195	-6.208
D	-7.827	-1.197	0.422	0.848	-5.235	-0.015

To resolve this problem, we first compute the Euclidean distances between each pair of models, treating each observation as a value corresponding to each axis in a six-dimensional Euclidean space. For 4 models we can compute 6 unique distances to make up the dissimilarity matrix shown in Table 3.2.

Table 3.2: Matrix showing mutual dissimilarities between models

	A	**B**	**C**	**D**
A	0	0.507	0.437	1.078
B	0.507	0	0.100	1.100
C	0.437	0.100	0	0.886
D	1.078	1.100	0.886	0

We now invoke the multidimensional scaling algorithm to translate the dissimilarities onto a two-dimensional space, such that model pairs with small dissimilarities appear closer to each other on the map.

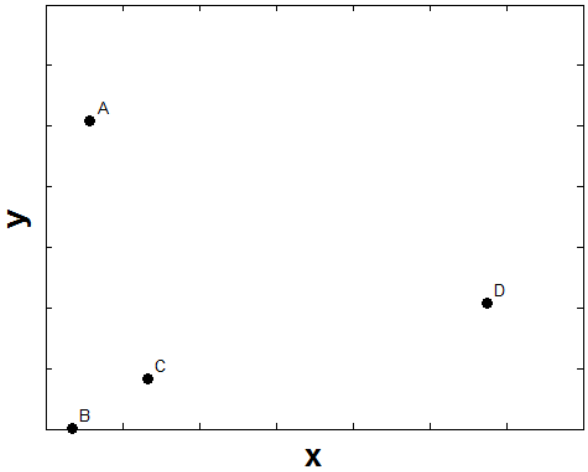

Figure 3.2: 2D map produced by MDS

Figure 3.2 shows the results of MDS for the 4 models projected on a two-dimensional space. Models B and C, for example, have the smallest dissimilarities and as such, are placed closest together in space. Likewise, B and D exhibit the largest dissimilarities, and are therefore furthest from each other on the resulting map. It is evident that the algorithm is capable of representing the dissimilarities as spatial proximities such that similar models can be perceived as being closer together on a map.

4. **Group models into clusters and select representative models.**

This step is highly consequential to the entire process. Now that the models have been projected onto a lower dimension space such that they can be visualized easily, an algorithm to cluster models based on proximity must be implemented. For this purpose we adopted the well-established k-means clustering algorithm.

k-means clustering, also known as Lloyd's algorithm, is a clustering method where observations are assigned to one of n clusters that have been defined by selected

centroids. The cluster centroids are determined such that the sum of the square distances between the observations in a cluster and the cluster centroid is minimized. This would fundamentally also result in the distance between cluster centroids being maximized. In essence, k-means clustering provides the solution to an optimization problem and thus could produce different clustering combinations with each implementation.

The algorithm proceeds as follows:

1. Choose *n* initial centroids.
2. Compute point-to-cluster-centroid distances for all observations in each centroid.
3. Assign each observation to the cluster with the closest centroid.
4. Recompute the cluster centroids as the average of the observations in each cluster.
5. Repeat steps 2 to 4 until cluster assignments do not change.

Notice that implementation of the steps listed above requires that the number of clusters, *n*, be previously defined. Choosing an ideal number of clusters however, is a bit complicated. Bhowmik [2014] for example, implemented a trial-and-error method to maximize an "effectiveness of clustering" parameter, which is a measure of the ratio of distances between cluster centroids to distances within a single cluster. This is also similar to the "silhouette" measure presented by Rousseeuw in 1987 and implemented by Hotho et. al [2002]. A general rule of thumb is that the number of clusters, n, be equal to the square root of half the number of observations, m, as shown in Equation 3.2.

$$n = \sqrt{\frac{m}{2}}\,. \tag{3.2}$$

5. Select best-fit cluster.

At this point, we have produced clusters, each of which contains a significantly smaller ensemble of models than the prior population. After comparison with

observed field data, one of these clusters will be selected as the posterior ensemble and used to predict the reservoir performance and associated uncertainty. In order to compare the clusters, one representative is chosen for each cluster. In this work the model closest to the centroid is chosen as the representative model. The representative models are then evaluated with a full-physics simulator. Notice that by implementing proxies, we reduced the number of times a full-physics simulator is employed from *m* to *n* (*n* << *m*, see Equation 3.2). The sum of the squares of errors between the simulated forecasts and the observed data can be calculated. The best-fit cluster is established as the one that produces the minimum deviation from the observed results.

6. **Model Expansion.**

Due to the composition of the model selection and clustering framework, it is very possible to arrive at an ensemble that possesses forecast with a larger deviation from the observed data than is desired. In such cases it is recommended to perform another cycle of model selection. In the approach used by Bhowmik [2014], the selected cluster from each model selection cycle is taken as the prior ensemble for subsequent cycles. The problem with this approach is that after 2 or 3 cycles, the number of models would have dwindled drastically and the model ensemble would be insufficient to perform any meaningful clustering. One solution would be to expand the selection of models within the selected cluster by generating a new population of models that share the common characteristics of the models within the selected cluster. This is the primary concept of model expansion. As mentioned earlier, the models within a cluster will possess similar geologic characteristics in those regions of the reservoir where the influence of geologic architecture on the response is most significant (usually regions close to the wells). It is therefore crucial to preserve these high probability geologic features, since they can be interpreted to be representative

of the geology of the actual reservoir. In model expansion, we locate additional "hard" data locations that occur repeatedly in the models belonging to the selected cluster. . The obtained hard data can then be used to generate a new suite of models using the same geostatistical modeling technique that was used to create the previous ensemble.

The six steps detailed above outlines the model selection algorithm as it was used specifically in this work. Figure 3.3 shows a schematic of the algorithm.

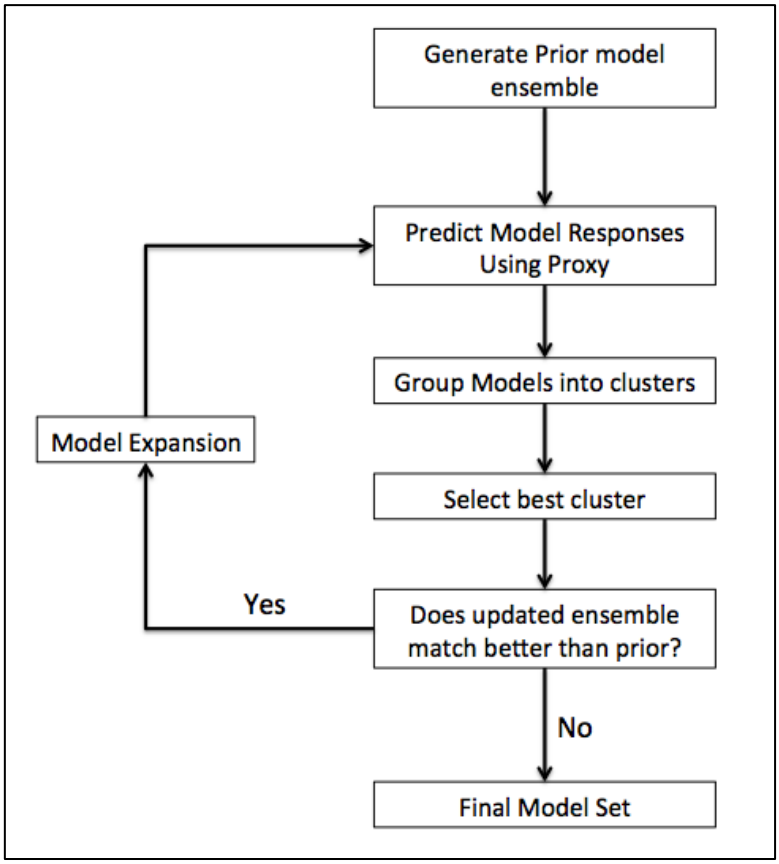

Figure 3.3: Schematic of the model selection algorithm used

Chapter Summary

In this chapter, we detailed the model selection algorithm as it was used in this project. We introduced the individual components of the scheme shown in Figure 3.3. The

multidimensional scaling and k-means clustering methods used to group the models into clusters were presented and explained. In Chapter 4, we present the formulation of the proxy used to produce a fast approximation of the flow response.

CHAPTER 4: RANDOM WALKER PARTICLE TRACKING

As discussed in chapter 2, the effectiveness of the model selection algorithm hinges on the implementation of a fast proxy to estimate the flow response of the ensemble of prior models. The use of a full physics coupled simulation is impractical for this task, due to the computational time required for execution. In this chapter, we detail the formulation and implementation of the proxy developed, and compare the results to full physics simulations.

4.1 Formulation

The idea of representing a continuous volume of fluid with discrete particles is fairly common in tracer tests and simulations. In Random Walker Particle Tracking (RWPT), a number of particles are introduced into the grid system at the injector locations at each timestep. The movement of a particle through the grid is dependent only on the properties of its current and prospective grid blocks. The particles are "tracked" by keeping count of the number of particles in each grid block after every particle movement.

In a traditional RWPT scheme, the displacement of a particle is given by [Gardiner, 1990]

$$X_p(t+\Delta t) = X_p(t) + \left[\boldsymbol{u}\left(X_p,t\right) + \nabla\cdot\boldsymbol{D}\left(X_p,t\right)\right]\Delta t + \boldsymbol{B}\left(X_p,t\right)\cdot\xi(t)\sqrt{\Delta t}\,, \qquad (4.1)$$

where Δt is a step change in time, $X_p(t)$ is the position of a particle at time t, $\boldsymbol{u}$ is the velocity, $\boldsymbol{B}$ is the displacement matrix, **D** is the dispersion tensor and $\xi(t)$ is a vector of independent, normally distributed random variables with mean 0 and variance 1 [Bhowmik, 2014]. Lichtner et. al [2002] demonstrated that the displacement matrix *B* is related to the dispersion tensor by the relation: $\boldsymbol{B}\boldsymbol{B}^T = 2\boldsymbol{D}$. Note that the above formulation does not contain any grid-based parameters, and as such, the application of this method is not restricted to a gridded system.

In the implementation of the RWPT method in this work the particle movement is governed by a single transition probability term. In the composition of the transition probability however, we have incorporated parameters to mimic the advection and dispersion terms in Equation 4.1. For a particle at location A, the probability of transition to a location B is given as [Bhowmik, 2014]

$$P_{transition}\big(A(t) \rightarrow B(t+\Delta t)\big) = \Delta N_{A(t)\rightarrow B(t)} + k_{avg,A,B} \cdot e^{\Delta P_{A\rightarrow B}}\,, \qquad (4.2)$$

where $\Delta N_{A\rightarrow B}$ is the difference in particle count between the current and target grid blocks, $k_{avg,A,B}$ is the average permeability, and $\Delta P_{A\rightarrow B}$ is the static pressure difference between A and B. ΔN mimics the dispersion term in Equation 4.1, while $k \cdot e^{\Delta P}$ represents the velocity term. As written, the transition probability obtained from Equation 4.2 is not mathematically constrained between 0 and 1; however, the transition probabilities calculated to all candidate locations from the current block A will be normalized such that the values add up to 1, and are thus legitimate probabilities. The formulation of the transition probability is better understood with a more detailed introduction of the terms in Equation 4.2.

Particle count

The number of particles contained in a grid block is analogous to a fluid concentration (in the case of component transport) or saturation (in the case of multi-phase flow) parameter. The difference in particle count between two grid blocks is thus representative of the saturation or concentration gradient at that location in the reservoir. Higher saturation and concentration gradients contribute to a higher potential of fluid flow in the subsurface; likewise, a larger difference in particle count increases the transition probability, facilitating the movement of particles between the grid blocks in question.

Permeability

The permeability term is calculated as a harmonic average between the current and potential grid blocks. This is the most important term in dictating the orientation of flow, as it conveys the main geologic characteristics of the reservoir. In reservoir simulators, higher permeability values correspond to higher grid transmissibilities, allowing for enhanced flow. In the particle tracking scheme, an increase in permeability induces a corresponding increase in transition probability, thus heightening the likelihood of particle movement between two grid blocks.

Static pressure difference

The static pressure gradient contributes to the movement of the fluid between blocks that are at different vertical depths. This term therefore conveys the effect of reservoir topography and buoyant characteristics of the injected fluid to the simulation. While this term is trivial in two-dimensional (areal) grids, it is highly significant in three-dimensional grid structures and controls the vertical flow of a buoyant gas. A calibration factor (not shown in Equation 4.2) can be assigned to the exponential factor in cases where the buoyancy effects are even more pronounced. For simple grids, the static pressure can be easily calculated by constraining the pressure at an arbitrary reference horizontal datum. For more complex grid structures and topographies, it may be more practical to obtain these values from the initialization step of a reservoir simulator.

To ensure that fundamental physical requirements for fluid flow in porous media are met, it is essential to implement some additional constraints in the particle-tracking algorithm. First, let us designate a number of particles to represent a specific volume of fluid: if a fluid injection rate of q bbl/day is represented in the proxy by N particles/day, then the particle-to-volume ratio is N/q particles/bbl. This ratio is specific to a particular simulation and should

be chosen such that the proxy can sufficiently reproduce the physical characteristics of the fluid and provide reasonable results. It is up to the modeler to choose the number of particles that would represent a certain volume. The choice of N/q is quite delicate and consequential to the simulation; it is recommended that different values be tested using a sample model to ensure that the fluid flow is reasonably represented. The constraints on particle movements through the grid are detailed below:

1. **Maximum grid block accommodation.** We set an upper threshold on the number of particles a grid block can hold. This constraint is intended to represent the volumetric limitation of the pore space in the grid blocks and is dependent on grid block bulk volume, porosity, and particle-to-volume ratio. The maximum grid block accommodation, $N_{A,max}$, can be calculated as

$$N_{A,max} = \frac{V_b \cdot \phi}{q/N}\,, \tag{4.3}$$

where the subscript A signifies the grid block in question, V_b is its bulk volume, ϕ is porosity and q and N are as previously defined. Recalling that the particle-to-volume ratio, $PVR = N/q$, Equation 4.3 can be rewritten as

$$N_{A,max} = V_b \cdot \phi \cdot PVR\,. \tag{4.4}$$

To enforce this limitation, we set the transition probability to a target grid block equal to zero if it has reached its maximum particle count.

2. **Fluid compressibility.** We also implemented a way to account for the fluid compressibility i.e. we defined the probability that the particle does not transition from a grid block. This probability is a function of the difference between the current particle count and the maximum allowable count for the grid block (i.e. $N_{A,max}$-N). The larger this difference, the higher the non-transition probability, or "staying power". This non-transition probability introduces the current grid block as a potential

future location of the particle. That is, in a computational framework, it is acceptable to translate this as the probability of transition of a particle to its current grid block.

3. **Minimum grid block accommodation.** We set a lower threshold on the particle count for every grid block. This constraint is established to mimic the effect of residual saturation on fluids in porous media. The minimum grid block accommodation can be calculated as

$$N_{A,min} = V_b \cdot \phi \cdot PVR \cdot S_r \,, \tag{4.5}$$

where S_r is the residual saturation of the injected fluid. If the current particle count of a grid block is less than or equal to its minimum allowable particle count, we set the probability of transition out of that grid block equal to zero. Consequently, the non-transition probability becomes 1.

We have now discussed all the factors and constraints needed to simulate particle movement through the grid. To illustrate how the transition probabilities are used to predict migration, let us now concentrate on a movable particle in a grid block, surrounded by six neighboring blocks (four neighboring blocks in a two-dimensional grid) as shown in Figure 4.1(a). The transition probabilities for the six target blocks can be calculated, in addition to the probability of remaining (non-transition) in the current block. These probabilities are normalized and combined to construct a cumulative density function (*cdf*) as shown in Figure 4.1(b), with the current and potential grid blocks expressed as discrete random variables on the horizontal axis.

Next, we generate a random number from a uniform distribution and perform a Monte-Carlo sampling of the constructed *cdf*. In the example presented in Figure 4.1, the generated random number was 0.6, corresponding to a sampled value of 3; we thus move the particle to grid block 3.

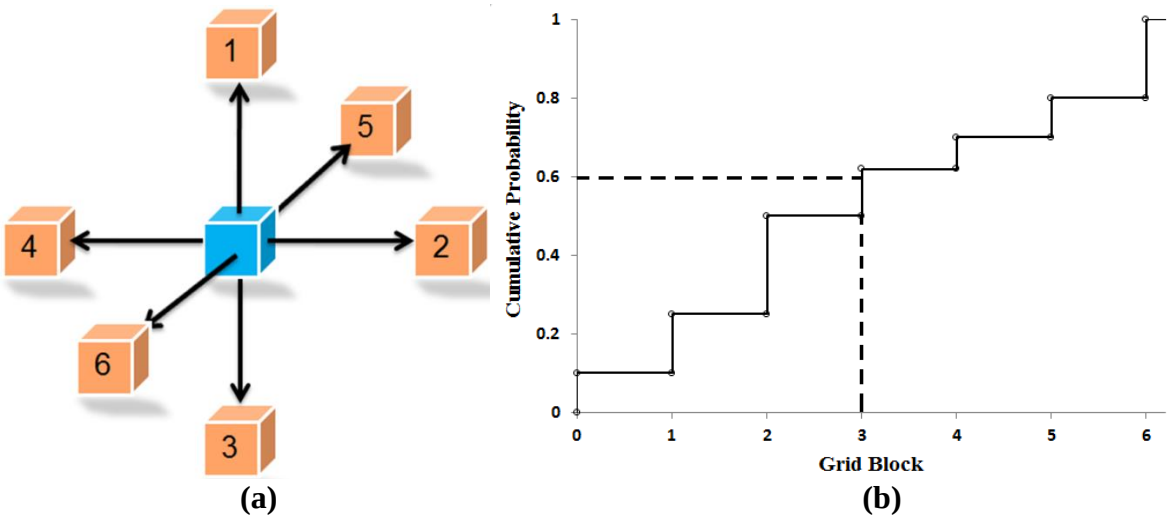

Figure 4.1: (a) Current particle location (blue) and the six neighboring grid blocks. All seven blocks are candidates for the target location of the particle. (b) Cumulative density function constructed from the transition probability for the seven blocks [Bhowmik, 2014]

Having detailed the procedure of moving a single particle, we can now focus on the large-scale migration of multiple particles and their interactions throughout the grid. At the start of first timestep, we introduce a set of particles into the injector location on the grid. For every particle introduced, it is transported through the grid until it reaches a location where the particle count is less than N_{min} or the transition probability is sampled such that it remains in its current block; these are the stopping criteria during this timestep. The movement can be regarded as a domino effect, where the moving particle migrates into a neighboring block and "pushes" another particle away. The sequence is then stopped when the probability for transitioning to a nearby block becomes too low to displace another particle from its destination block. We then proceed to moving the next particle from the injector grid block, and continue the sequence until all the movable particles that were initially contained in the injector grid block have met a stopping criterion; this indicates the end of the timestep. The particles can then be counted in every grid block and the relative count serves as a measure of concentration or saturation.

For the initial timestep, we considered the movable particle source to be only the injector location, and tracked the particle movements from there until they stopped at some final grid location. However, such an approach if continued for subsequent injection timesteps will not reflect fluid flow in the reservoir. This is because it is not only the injected fluid that moves through the reservoir, but rather all available mobile fluid [Bhowmik, 2014]. To resolve this problem, we define a source as all locations that contain mobile fluid; that is, all grid blocks containing a particle count greater than N_{min}. This is done only during the interval between two timesteps. At the start of a timestep, we establish all source locations and induce transition for all the movable particles contain in these grid blocks. Again, once all particles have reached their destination blocks, the particle count in the entire grid is regarded as a saturation analog. A summary of the overall procedure for implementing the proxy is shown in Figure 4.2.

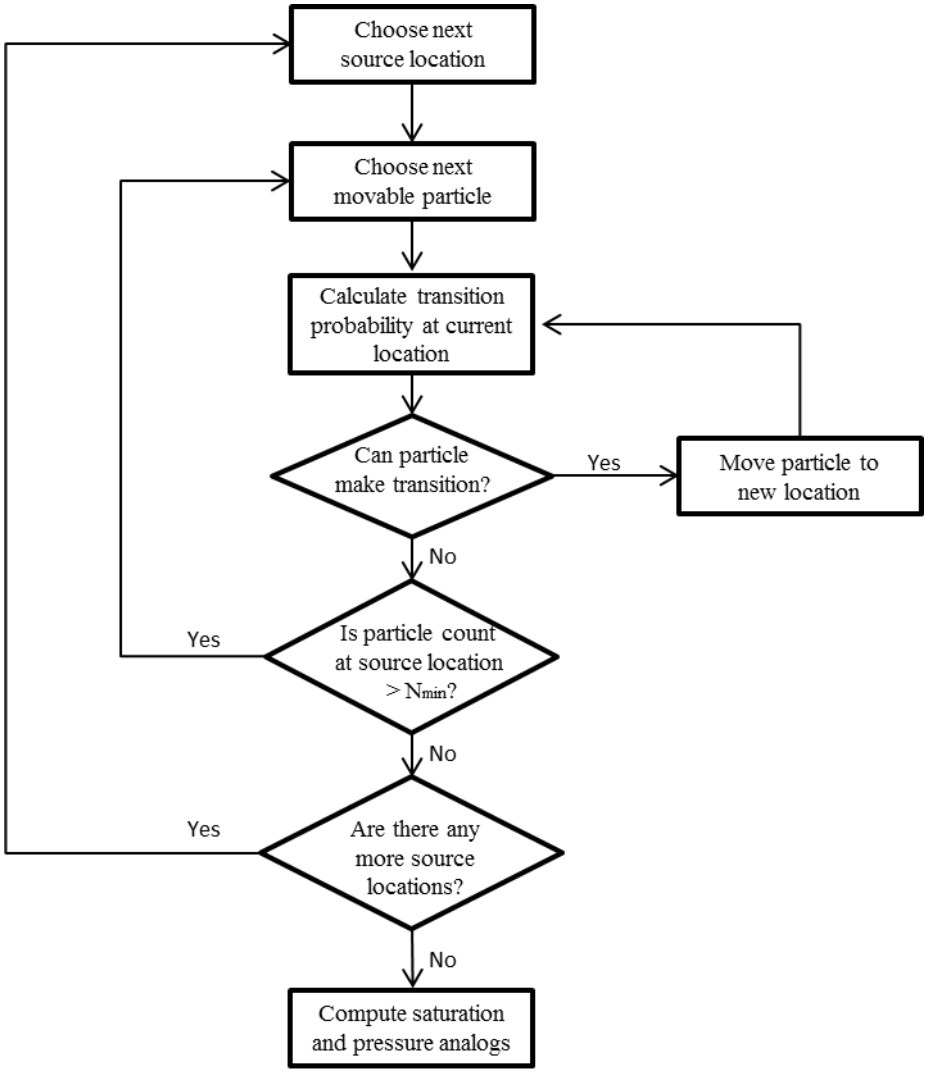

Figure 4.2: Flowchart showing the implementation of the particle tracking proxy for a single timestep [Bhowmik, 2014]

4.2 Pressure Estimation

In the previous section, we presented a procedure to approximate the saturation response for the reservoir. Before any geomechanical responses can be calculated however, we must devise a method to estimate the resulting pressure field due to the injection of CO_2. This is because rock deformation only arises as a result of implicit forces or external loads imposed on the matrix. In this case, the force imposed on the rock matrix manifests as a change in pore pressure with time.

In order to accomplish this task of estimating the field pressure response, we first recognize that the injected fluid contributes to the pressure build up at all locations in the reservoir. The magnitude of the pressure change at any location can be defined according to some function that is inversely proportional to the square of its distance from the injection location. This concept is similar to the pressure solution of the diffusivity equation at a radial distance away from an injector, which is given as

$$\Delta P = \frac{qB\mu}{4\pi kh} \ln\left(\frac{4kt}{\phi\mu c_t r^2}\right). \tag{4.6}$$

In our formulation, the "pressure" at a grid block is calculated as a sum of the particle count, weighted by distance, in all other blocks. The pressure P_i at a location *i* is expressed mathematically in Equation 4.7 [Bhowmik, 2014]

$$P_i = \sum_j N_j \cdot \ln({d_{ij}}^{-2}) \quad \forall j \in grid\ blocks\ where\ N_j > 0\,, \tag{4.7}$$

where N_j is the number of particles at location *j*, and d_{ij} is the distance between locations *i* and *j*.

4.3 Comparison of Proxy Response to Full-Physics Simulations

We tested the validity of the proxy by comparing results to full physics simulations for 2D and 3D synthetic models. The model used below is for a two-dimensional synthetic reservoir with high permeability channels embedded in a shale matrix. This sharp permeability contrast was used to ensure that the simulation results would offer a clear visual comparison with the full physics model. Figure 4.3 shows the 100 x 100 model, with a single injector at the center of the grid. The channels (colored in red) have a permeability of 250 mD, while the matrix has a low permeability of 1 mD.

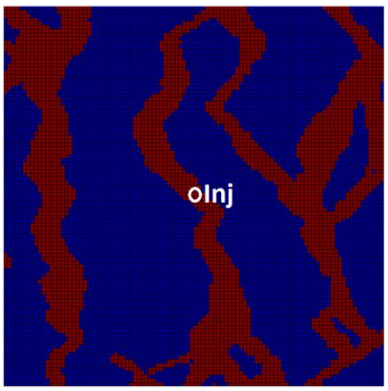

Figure 4.3: Synthetic model showing high permeability channels in a low permeability matrix, with a CO_2 injector at the center of the reservoir

The saturation responses for the proxy and the full physics simulation are shown in Figure 4.4; the results look reasonably comparable. It is evident that the flow migration occurs primarily through the high permeability pathways in both simulators. However, one major difference occurs at the boundary between the main migration path and the low permeability regions. In the full-physics simulation result produced by CMG, the contrast at this boundary is remarkably sharp as compared to the more graded contrast produced by the proxy. This is because, in the particle tracking approximation the contribution of the $\Delta N_{A(t)\rightarrow B(t)}$ term in Equation 4.2 is slightly more, as compared to the $k_{avg,A,B}$ and $\Delta P_{A\rightarrow B}$ terms. Notwithstanding, the results show that the proxy approximates the shape of the CO_2 saturation response well, and can adequately capture the differences in the migration pathways between multiple models in the prior ensemble.

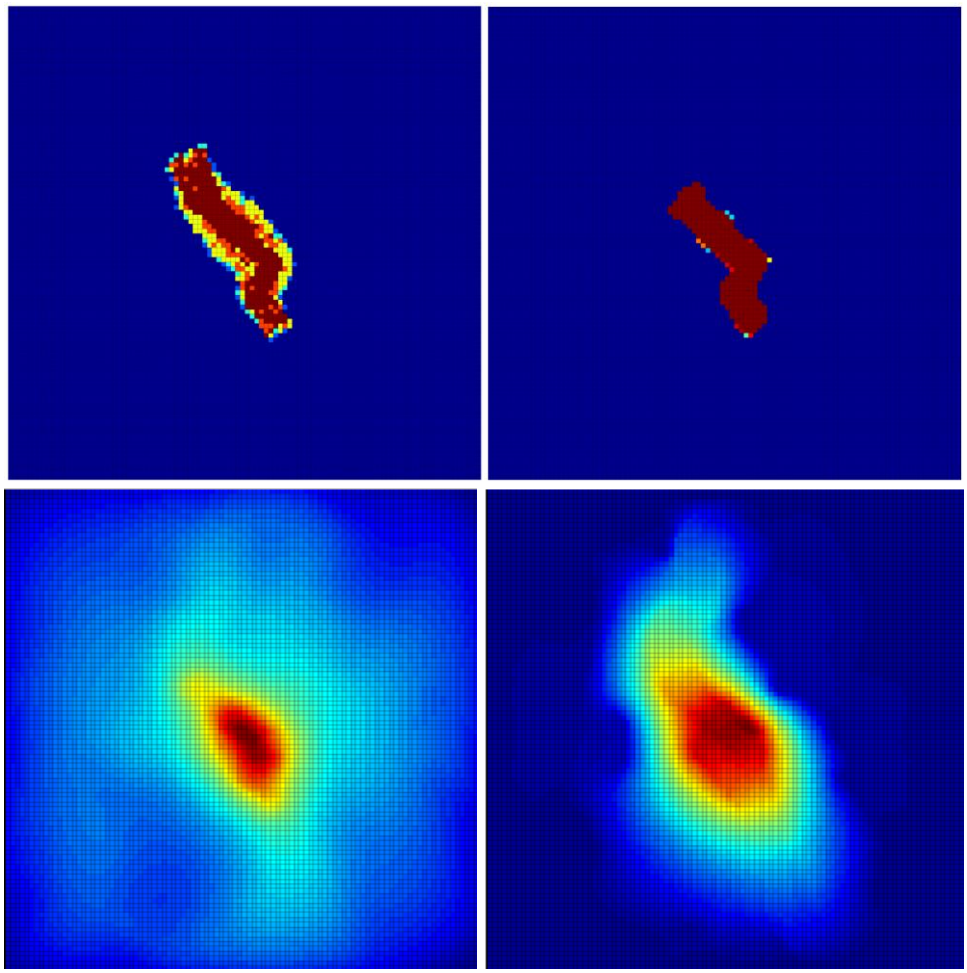

Figure 4.4: Simulation results showing the shape of the CO_2 plume migration (top) and pressure distribution (bottom) for the particle tracking proxy (left) and CMG simulator (right)

We also applied the proxy to three-dimensional synthetic models. A question we sought to answer was whether or not the proxy adequately represents buoyancy. In reality, as CO_2 is much less dense than the aquifer brine, migration of the injected plume occurs primarily upwards, before it spreads out laterally at the top of the aquifer.

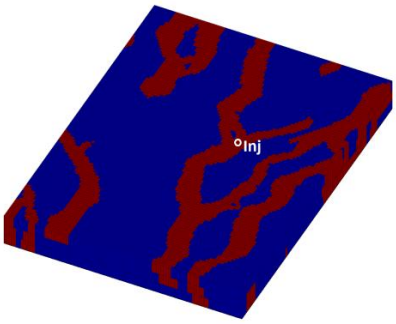

Figure 4.5: Synthetic 3D model showing high permeability channels embedded in a low permeability matrix, with a CO_2 injector at the bottom layer of the reservoir

Figure 4.5 shows the three-dimensional synthetic reservoir model. Again, we used high contrast in permeability between the channels and the surrounding mudstone in order to allow for an easier visual comparison of results. The channels have a 250 mD permeability while the matrix has a permeability of 1 mD. The model shown is a 100 x 100 x 3 grid, with injection in the bottom layer of the structure.

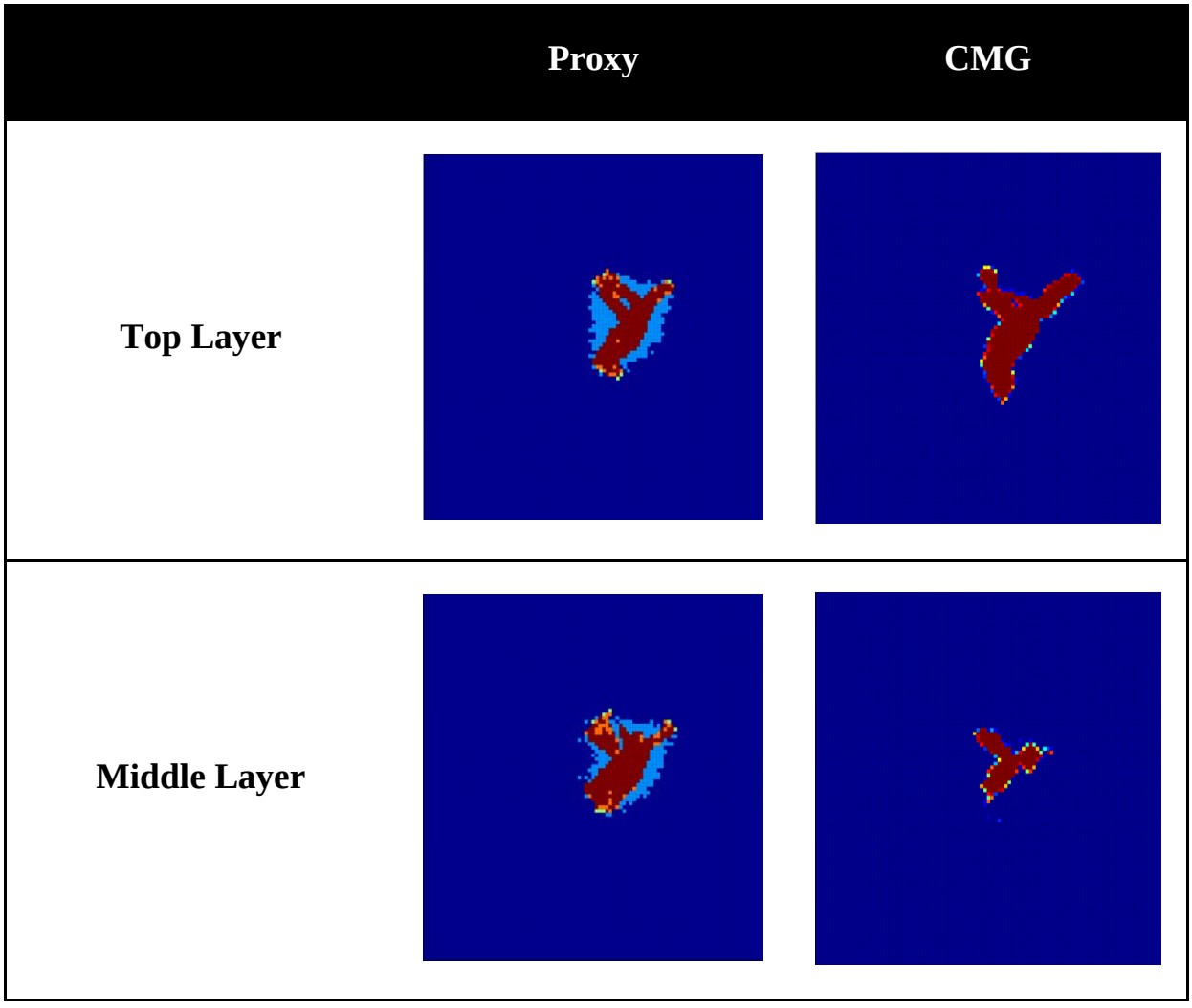

Figure 4.6: Comparison of CO_2 migration results for a 3D synthetic model, with equal weights assigned to the viscous and gravity terms

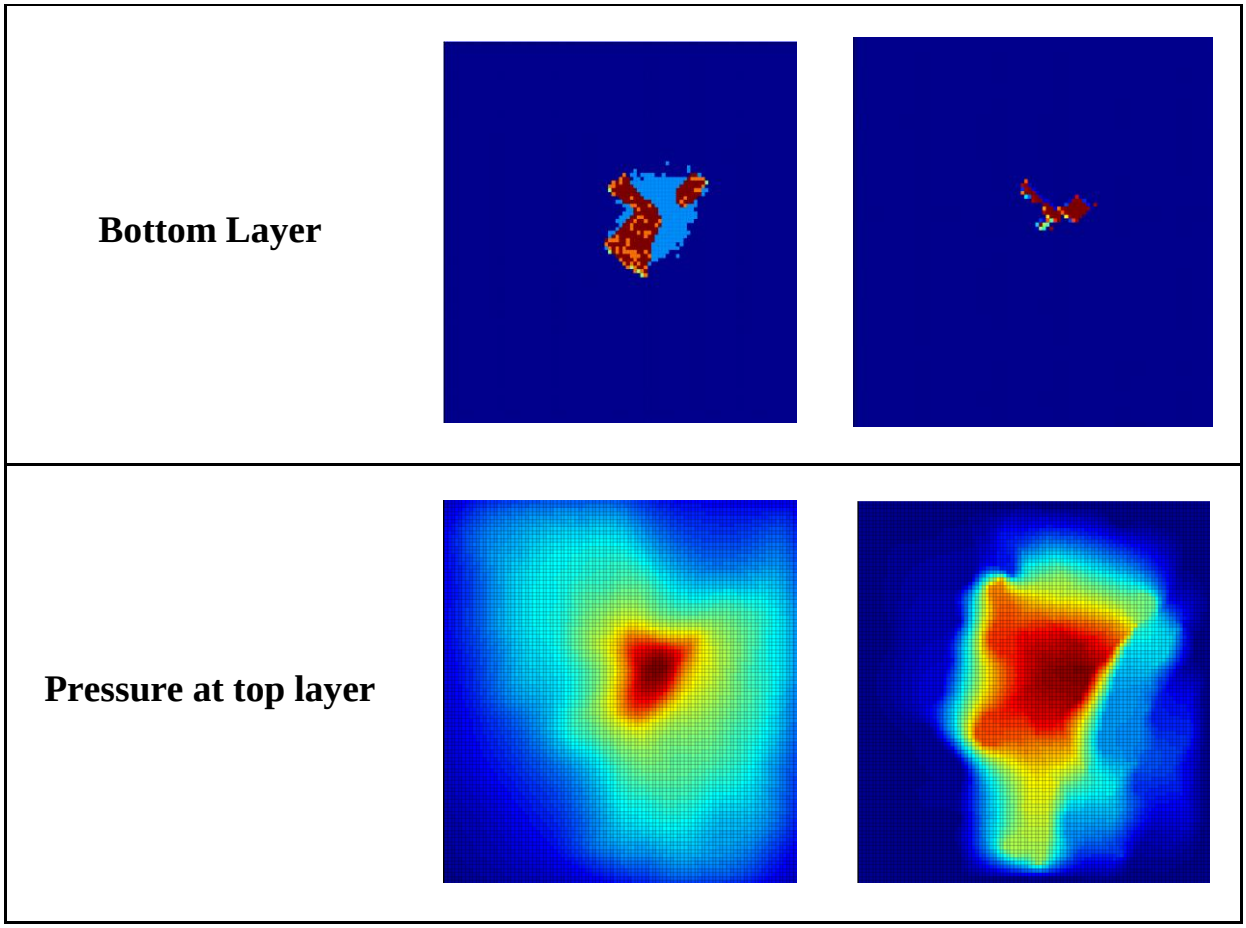

Figure 4.6, cont.

Simulation results are shown in Figure 4.6. The left part of the figure shows the particle count calculated by the proxy for each layer in the model. In comparison to the CMG simulation results on the right, it is clear that the buoyancy effects in the proxy are not as pronounced as they should be. The proxy results show that the bottom and middle layers of the model containing a significantly larger amount of CO_2 than the full physics simulation predicts. Because of this, the lateral migration of the plume in the top layer is not as much and the CO2 does not travel as far through the channels.

It can be interpreted that with the current formulation of the transition probability, the viscous forces dominate the gravity forces. To ensure that the gravity effects are more pronounced in 3D models, we have assigned a larger weight to the $\Delta P_{A\rightarrow B}$ term in Equation 4.2. We establish the magnitude of this weight by trial and error on a similar sample model

until buoyancy is reasonably portrayed in the simulation output. We then repeat the proxy simulation for the model shown in Figure 4.5. With a newly weighted formulation, it is expected that the CO_2 plume migrates primarily upwards before spreading out through the high permeability channels in the top layer. Results are shown in Figure 4.7.

The result obtained from the weighted formulation conforms more to the expected behavior of the plume. The extent of the lateral spread of the CO_2 plume in the bottom and middle layers is significantly reduced. Consequently, the CO2 plume migrates more through the high permeability channels in the top layer. These results imply that the particle tracking proxy can satisfactorily characterize the shape of the migration pathways and the flow connectivity in both 2D and 3D models, provided that we can apply appropriate calibration factors to the viscous and gravity terms. The shape of the plume serves as an estimate of CO_2 saturation profile and the results can now be used to produce a measure of the field pressure response due to injection.

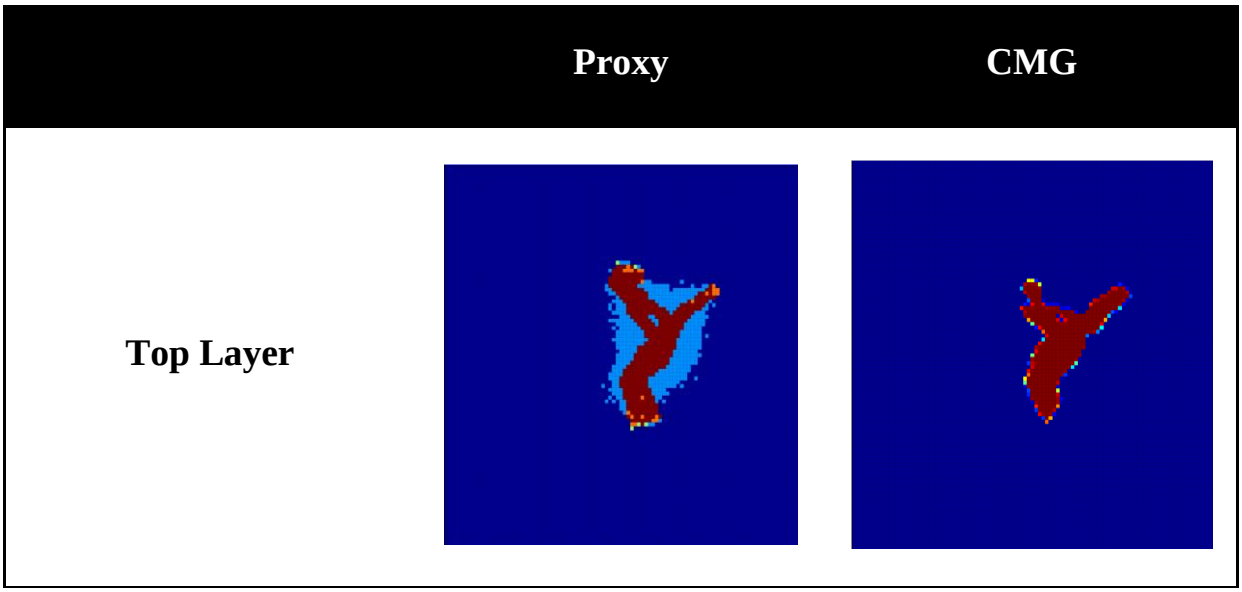

Figure 4.7: Comparison of CO_2 migration results for a 3D synthetic model, with larger weights assigned to the gravity term

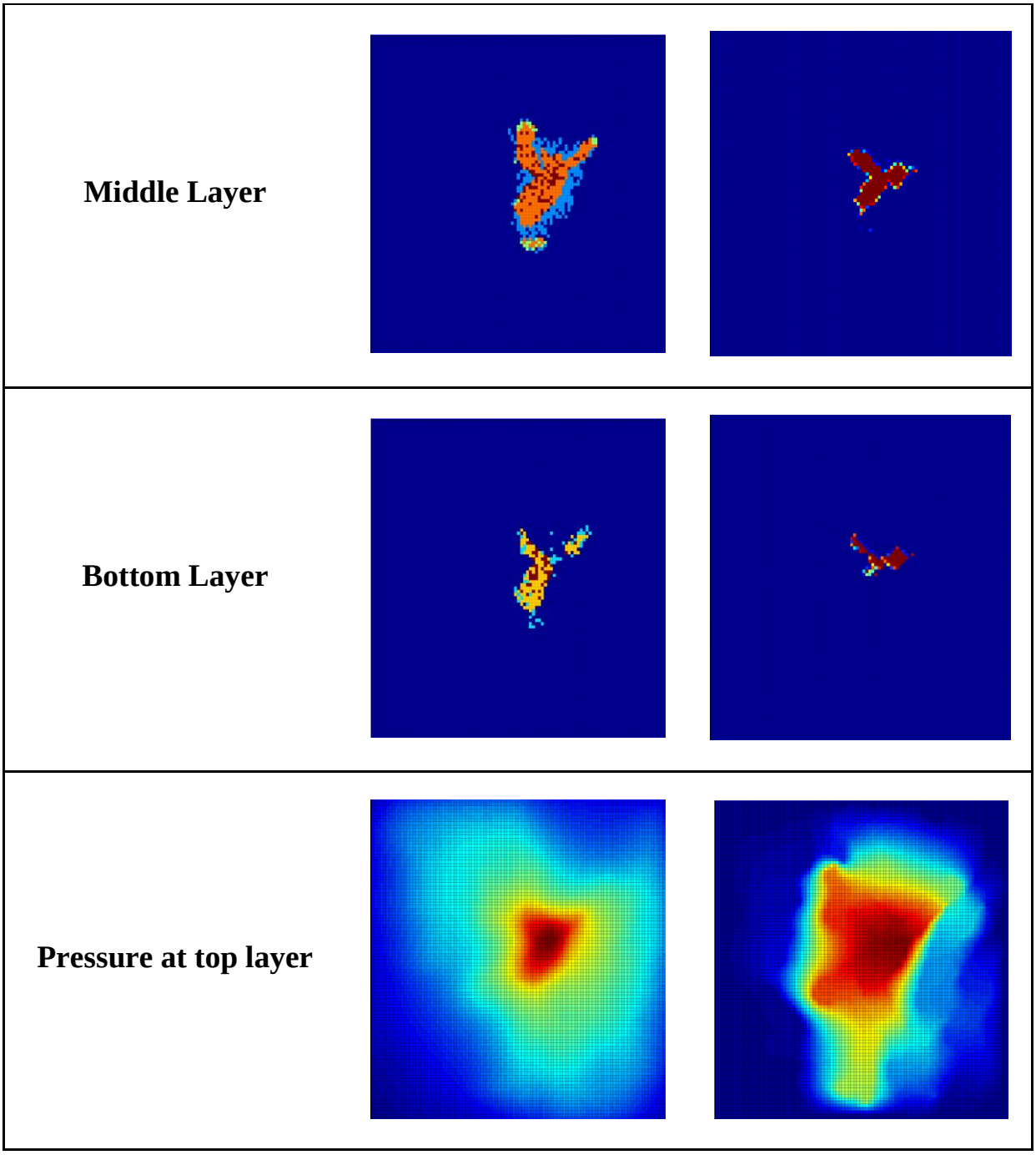

Figure 4.7, cont.

4.4 Simulation Time Comparison.

It is instructive to compare the computational time expended to generate the results presented in preceding sections. Table 4.1 shows a summary of simulation times.

Table 4.1: Comparison of Execution Times for Proxy and Full Physics Simulations

	PROXY	CMG
2D	**1.09 s**	**3.76 s**
3D	**14.10 s**	**184 s**

The proxy consequently results in significant speed up especially in the case of 3D models. It is also important to note that the proxy will not yield a response exactly the same as that from a full physics simulation. However, because the intent is to discriminate between the models in the prior suite in terms of their flow and geomechanical response, the performance of the proxy is sufficient for that purpose.

4.5 Chapter Summary

In this chapter, we demonstrated the implementation of a particle tracking proxy that determined particle migration based on a sampling from a cumulative density function. The proxy results are shown to correlate reasonably well with full physics solutions obtained from the CMG simulator. In Chapter 5, we will detail the formulation of the stress equilibrium equations, and demonstrate how field pressure is used as an input to estimate rock deformation.

CHAPTER 5: MODELING GEOMECHANICAL EFFECTS OF GEOLOGIC SEQUESTRATION OF CO2

5.1 Motivation

As CO_2 storage in the subsurface gains popularity, operators have investigated several techniques to monitor the movement of the plume in the aquifer. One technique that has been recently applied to monitoring CO_2 injection involves the use of remote sensing data to measure changes in the topography of the earth's surface. The remote sensors based on a satellite emit pulses towards the surface and receive reflected signal back from the earth. By differencing successive maps of the surface, surface deflections in the surface topography can be recorded. Topography changes, albeit minuscule, give a direct indication of the relative pressure build up in the aquifer. Pressurized regions reveal uplift at the surface; likewise, pressure-depleted regions result in slight subsidence. Onuma and Ohkawa [2009] investigated the applicability of satellite-borne InSAR (Interferometric Synthetic Aperture Radar) techniques to monitor surface deformations at the In Salah CO_2 injection site, Algeria (Figure 5.1). They present results that suggest relationships between the surface deformation patterns, the geologic features of the aquifer and the distribution of injected CO_2.

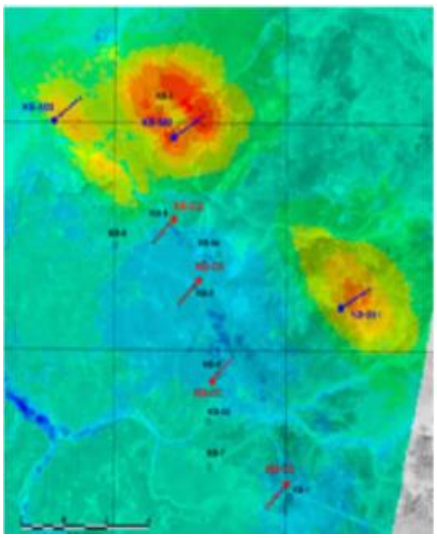

Figure 5.1: Surface deformation map for the Krechba formation in Algeria [Onuma et. al, 2008]

From a reservoir modeling perspective, one way to utilize information from remote sensing is to incorporate that information as an additional criterion for history matching. In addition to the bottom-hole pressures and injection rates, we can use a surface deformation map as a basis for selecting best-fit models. An immense benefit of implementing this strategy within a model selection framework is that the pressure field that propagates much faster from the injector than the actual CO_2 plume provides important early information about the migration of the plume. At early injection times, or in cases when the CO_2 cannot migrate far from the well, we can still obtain some information about the geologic structure of the entire reservoir, including areas that have not been directly contacted by the injected CO_2. Figure 5.2 shows an example of the field pressure response, predicted by CMG, at the very early stages of a CO_2 injection project. Clearly, the pressure field informs a much larger area of the reservoir than the fluid-swept region at the same instant in time.

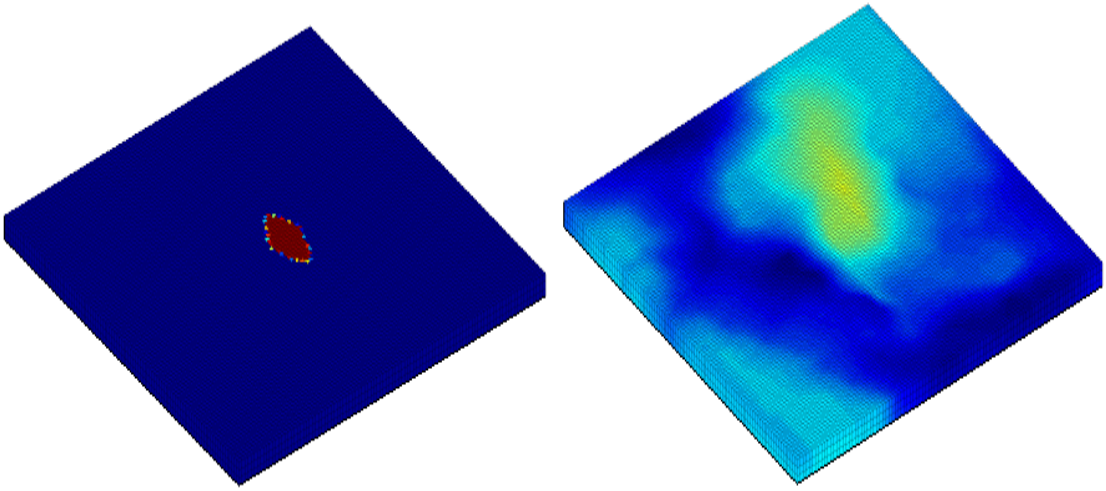

Figure 5.2: CO_2 saturation (left) and the corresponding field pressure (right) after 100 days of injection

5.2 Formulation of the Stress Analysis Equations

In chapter 2, we discussed some established techniques for coupling between flow and geomechanics simulations. We have used the one-way partial coupling technique for this

project because of the low computational cost involved, and the flexibility associated with the choice of simulators employed. In chapter 4, we demonstrated how the solution to the flow conservation equations can be estimated using a particle tracking proxy. We will now focus on implementing a finite element method solver to approximate the rock deformation, assuming the field pressure has been obtained. In this section, we present, in thorough detail, the mathematical formulation of the geomechanics simulation, and the development of the stress-analysis equations.

5.2.1 Momentum Balance

We start with the derivation of the momentum balance equation for an entity under the influence of surface and body forces.

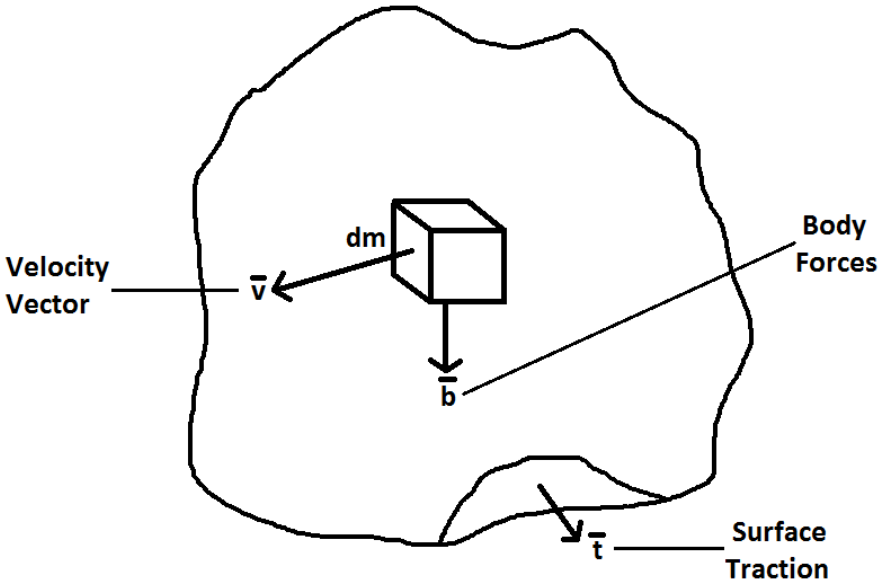

Figure 5.3: Entity under influence of body and surface forces

The momentum of the differential body within the shape shown in Figure 5.3 can be given as

$$d\boldsymbol{P} = \boldsymbol{v}dm = \rho \boldsymbol{v} dV \,, \tag{5.1}$$

where dm is the mass of the differential element, dV is its volume, ρ is the density, and $d\boldsymbol{P}$ and $\boldsymbol{v}$ are the momentum and velocity vectors, respectively. We can thus write the total momentum of the entire shape as

$$\boldsymbol{P} = \int \rho \boldsymbol{v} dV . \tag{5.2}$$

According to Newton's second law, the time rate of change of momentum is equal to the sum of the forces applied to a body. Applying this law to the shape of the element in Figure 5.3, we can write

$$\frac{d}{dt}\int \rho \boldsymbol{v} dV = \int \rho \boldsymbol{b} dV + \int \boldsymbol{t} dS, \tag{5.3}$$

where $\boldsymbol{t}$ is the stress tensor across an imaginary surface dS and $\boldsymbol{b}$ represents all body forces acting on the control volume. The first term on the right hand side reflects the body force acting on the element while the second term reflects the external force acting on the element. Using the Cauchy stress equation, we can relate $\boldsymbol{t}$ to the true stress tensor $\boldsymbol{\sigma}$ and a unit normal vector $\boldsymbol{n}$ by

$$\boldsymbol{t} = \boldsymbol{\sigma}^T \cdot \boldsymbol{n} . \tag{5.4}$$

We can thus rewrite Equation 5.3 as

$$\frac{d}{dt}\int \rho \boldsymbol{v} dV = \int \rho \boldsymbol{b} dV + \int \boldsymbol{\sigma}^T \cdot \boldsymbol{n} dS . \tag{5.5}$$

From the Reynolds Transport Theorem, the change in a quantity A within a body, corresponding to a change in the control volume of the body can be expressed as

$$\frac{d}{dt}\int \rho A dV = \int \rho \frac{dA}{dt} dV . \tag{5.6}$$

Applying this theorem to the left side of Equation 5.5, we get:

$$\int \rho \frac{d\boldsymbol{v}}{dt} dV = \int \rho \boldsymbol{b} dV + \int \boldsymbol{\sigma}^T \cdot \boldsymbol{n} dS \, . \tag{5.7}$$

Now, if we apply the Divergence Theorem to the last term, Equation 5.7 can be reconstructed as

$$\int \rho \frac{d\boldsymbol{v}}{dt} dV = \int \rho \boldsymbol{b} dV + \int \nabla \cdot \boldsymbol{\sigma}^T dV = \int [\rho \boldsymbol{b} + \nabla \cdot \boldsymbol{\sigma}^T] dV \, . \tag{5.8}$$

Understanding that the integrands must be equal for any *dV*,

$$\rho \frac{d\boldsymbol{v}}{dt} = \rho \boldsymbol{b} + \nabla \cdot \boldsymbol{\sigma}^T \, . \tag{5.9}$$

Finally, we realize that for angular momentum to be conserved, the Cauchy stress tensor has to be symmetric, so $\boldsymbol{\sigma} = \boldsymbol{\sigma}^T$. Equation 5.9 becomes

$$\rho \frac{\partial^2 \boldsymbol{u}}{\partial t^2} = \rho \boldsymbol{b} + \nabla \cdot \boldsymbol{\sigma} \, , \tag{5.10}$$

where the velocity has been replaced with the time derivative of displacement, with $\boldsymbol{u}$ being the displacement vector.

If we introduce the notation $\ddot{\boldsymbol{u}} = \partial \boldsymbol{u} / \partial t$, we can write the overall equilibrium or momentum balance as [Zienkiewicz et. al, 1999]

$$\nabla \cdot \boldsymbol{\sigma} + \rho \boldsymbol{b} - \rho \ddot{\boldsymbol{u}} = 0 \, . \tag{5.11}$$

5.2.2 Finite Element Discretization

Given a partial differential equation defined for a continuum within a domain Ω, enclosed by the boundary Γ

$$\boldsymbol{X}\ddot{\Phi} + \boldsymbol{Y}\dot{\Phi} + \mathrm{Z}\Phi = 0\,, \tag{5.12}$$

where $\boldsymbol{X}$, $\boldsymbol{Y}$ are matrices of constants, Z is a spatial differential operator, and Φ is a vector of dependent variables, say displacements and pressure, the finite element solution can be obtained by [Zienkiewicz et. al, 1999]:

1. Approximating the function by a set of parameters $\overline{\Phi}_k$ and shape functions N_k specified in spatial dimensions. The function thus takes the form

$$\Phi \cong \Phi^h = \sum_{k=1}^{n} N_k(x, y, z)\overline{\Phi}_k\,, \tag{5.13}$$

   where $\overline{\Phi}_i$ are the values of the unknown function at discrete points in space called nodes. The shape functions serve to interpolate the solution between the discrete values obtained at the nodes. Typically, low order polynomials are used to represent the form of the shape functions. However, the full form of the shape functions are dependent on the number of nodes specified within a single element in the finite element mesh.

2. Substituting the value of the approximating function back into the differential equation. By doing this, we seek to obtain a solution that is close enough to the actual solution such that the residual is approximately zero. The residual equation which we set equal to zero takes the form shown in Equation 5.14. Here we have integrated over the entire domain Ω, meaning that the sum, throughout the domain, of the weighted residuals should be approximately zero,

$$\int_{\Omega} \boldsymbol{W}_j^T \left(\boldsymbol{X}\ddot{\boldsymbol{\Phi}}^{\boldsymbol{h}} + \boldsymbol{Y}\dot{\boldsymbol{\Phi}}^{\boldsymbol{h}} + \mathbf{Z}(\boldsymbol{\Phi}^{\boldsymbol{h}})\right) d\boldsymbol{\Omega} = 0\,. \tag{5.14}$$

   The index *j* has the same meaning as the index *k* in Equation 5.13 and represents the node at which the residual exists. On integration, Equation 5.14 reduces to

$$\boldsymbol{M}\ddot{\bar{\Phi}} + \boldsymbol{C}\dot{\bar{\Phi}} + \mathbf{P}\bar{\Phi} = 0\,, \tag{5.15}$$

where $\boldsymbol{M}$, $\boldsymbol{C}$ and $\boldsymbol{P}$ are tensors whose sizes correspond to the set of parameters $\bar{\boldsymbol{\Phi}}_k$. A common choice for the weighting function W_j is to take them to be the same as the shape function N_j [Zienkiewicz et. al, 1999].

We can now achieve the spatial discretization involving displacements and pressure by using appropriate shape functions. Similar to Equation 5.13, the solution for $\boldsymbol{u}$ and p can be expressed as

$$\mathbf{u} \cong \mathbf{u}^h = \sum_{k=1}^{n} N_k^u \bar{\mathbf{u}}_k = N^u \bar{\boldsymbol{u}}\,, \tag{5.16}$$

$$\mathrm{p} \cong \mathrm{p}^h = \sum_{k=1}^{m} N_k^p \bar{\mathbf{p}}_k = N^p \bar{\boldsymbol{p}}\,, \tag{5.17}$$

where N^u and N^p are the shape functions for displacement and pressure respectively.

In three dimensions, the total stress has the components (recall that the stress tensor has only six unique elements due to symmetry):

$$\boldsymbol{\sigma} = \begin{pmatrix} \boldsymbol{\sigma_{xx}} \\ \boldsymbol{\sigma_{yy}} \\ \boldsymbol{\sigma_{zz}} \\ \boldsymbol{\sigma_{yz}} \\ \boldsymbol{\sigma_{zx}} \\ \boldsymbol{\sigma_{xy}} \end{pmatrix} \tag{5.18}$$

If we introduce the notation for the differential operator,

$$\boldsymbol{D} = \begin{bmatrix} \frac{\partial}{\partial x} & 0 & 0 \\ 0 & \frac{\partial}{\partial y} & 0 \\ 0 & 0 & \frac{\partial}{\partial z} \\ 0 & \frac{\partial}{\partial z} & \frac{\partial}{\partial y} \\ \frac{\partial}{\partial z} & 0 & \frac{\partial}{\partial x} \\ \frac{\partial}{\partial y} & \frac{\partial}{\partial x} & 0 \end{bmatrix} \tag{5.19}$$

the momentum balance given by Equation 5.11 can be re-written as

$$\mathbf{D}^T\boldsymbol{\sigma} + \rho\boldsymbol{b} - \rho\ddot{\boldsymbol{u}} = 0\,. \tag{5.20}$$

To obtain the equation discretized in space, we pre-multiply Equation 5.20 by the test function $(N^u)^T$ and then integrate the first term by parts, yielding [Zienkiewicz et. al, 1999]

$$\int_\Omega \boldsymbol{B}^T\boldsymbol{\sigma}d\Omega + \left[\int_\Omega (\boldsymbol{N}^u)^T\rho\boldsymbol{N}^u d\Omega\right]\ddot{\boldsymbol{u}} = \int_\Omega (\boldsymbol{N}^u)^T\rho\boldsymbol{b}d\Omega + \int_\Gamma (\boldsymbol{N}^u)^T\bar{\boldsymbol{t}}d\Gamma\,, \tag{5.21}$$

where Γ is the surface boundary, and $\bar{\boldsymbol{t}}$ represents the surface traction forces acting on the boundary. Note that the last term in Equation 5.21 was extracted as a result of integration by parts of the first term in Equation 5.20. **B** is a matrix given as

$$\boldsymbol{B} = \boldsymbol{D}\boldsymbol{N}^u\,. \tag{5.22}$$

The terms to the right of the equal sign in Equation 5.21 contains all the effects of the body forces and surface tractions, and constitutes what is known as the "load vector", $\mathbf{f}^u$.

$$\boldsymbol{f}^u = \int_\Omega (\boldsymbol{N}^u)^T\rho\boldsymbol{b}d\Omega + \int_\Gamma (\boldsymbol{N}^u)^T\bar{\boldsymbol{t}}d\Gamma\,. \tag{5.23}$$

Now, we introduce Terzaghi's effective stress principle written as [Terzaghi, 1936]:

$$\boldsymbol{\sigma} = \boldsymbol{\sigma}'' - \alpha \boldsymbol{m} p \,, \tag{5.24}$$

where $\boldsymbol{\sigma}''$ is the effective stress experienced by the rock matrix, α is the Biot's coefficient with $\alpha = 2/3$ being a fairly common value for calculation of rock deformation, and $\boldsymbol{m}$ is a vector written for three dimensional calculations as

$$\boldsymbol{m} = [1\ 1\ 1\ 0\ 0\ 0]^T \,. \tag{5.25}$$

We can now write Equation 5.21 in terms of the effective stress

$$\boldsymbol{M}\ddot{\boldsymbol{u}} + \int_{\Omega} \boldsymbol{B}^{\boldsymbol{T}} \boldsymbol{\sigma}'' d\Omega - \boldsymbol{Q}\overline{\boldsymbol{p}} - \boldsymbol{f}^{u} = 0 \,, \tag{5.26}$$

where **M** is known as the Mass Matrix of the system

$$\boldsymbol{M} = \int_{\Omega} (\boldsymbol{N}^{u})^{T} \rho \boldsymbol{N}^{u} d\Omega \,, \tag{5.27}$$

and **Q** is the coupling matrix

$$\boldsymbol{Q} = \int_{\Omega} \boldsymbol{B}^{T} \alpha \boldsymbol{m} \boldsymbol{N}^{p} d\Omega \,. \tag{5.28}$$

The strain tensor $\boldsymbol{\varepsilon}$ can be expressed as a function of displacement by the well-known equation [Inoue et. al, 2009]

$$\boldsymbol{\varepsilon} = \frac{\mathbf{1}}{\mathbf{2}} [\nabla \mathbf{u} + (\nabla \mathbf{u})^{T}] \,, \tag{5.29}$$

and in indicial notation as

$$\boldsymbol{\varepsilon}_{ij} = \frac{\mathbf{1}}{\mathbf{2}} \left[\frac{\partial \boldsymbol{u}_i}{\partial j} + \frac{\partial \boldsymbol{u}_j}{\partial i} \right] \,, \tag{5.30}$$

where the indices *i* and *j* are represent the three coordinates in space. As *i* and *j* go from x to z, the components of the strain tensor are

$$\begin{pmatrix} \boldsymbol{\varepsilon}_{xx} \\ \boldsymbol{\varepsilon}_{yy} \\ \boldsymbol{\varepsilon}_{zz} \\ \boldsymbol{\varepsilon}_{yz} \\ \boldsymbol{\varepsilon}_{zx} \\ \boldsymbol{\varepsilon}_{xy} \end{pmatrix} = \begin{pmatrix} \dfrac{\partial \boldsymbol{u}_x}{\partial x} \\ \dfrac{\partial \boldsymbol{u}_y}{\partial y} \\ \dfrac{\partial \boldsymbol{u}_z}{\partial z} \\ \dfrac{1}{2} \cdot \left(\dfrac{\partial \boldsymbol{u}_y}{\partial z} + \dfrac{\partial \boldsymbol{u}_z}{\partial y} \right) \\ \dfrac{1}{2} \cdot \left(\dfrac{\partial \boldsymbol{u}_x}{\partial z} + \dfrac{\partial \boldsymbol{u}_z}{\partial x} \right) \\ \dfrac{1}{2} \cdot \left(\dfrac{\partial \boldsymbol{u}_x}{\partial y} + \dfrac{\partial \boldsymbol{u}_y}{\partial x} \right) \end{pmatrix}. \tag{5.31}$$

If we modify the definition of the strain tensor, such that

$$\boldsymbol{\varepsilon} = \begin{pmatrix} \boldsymbol{\varepsilon}_{xx} \\ \boldsymbol{\varepsilon}_{yy} \\ \boldsymbol{\varepsilon}_{zz} \\ 2\boldsymbol{\varepsilon}_{yz} \\ 2\boldsymbol{\varepsilon}_{zx} \\ 2\boldsymbol{\varepsilon}_{xy} \end{pmatrix}, \tag{5.32}$$

and we let the displacements in be equal to their approximating terms, $\boldsymbol{u} = N^u \boldsymbol{u}$, then

$$\boldsymbol{\varepsilon} = \begin{pmatrix} \dfrac{\partial N^u \boldsymbol{u}_x}{\partial x} \\ \dfrac{\partial N^u \boldsymbol{u}_y}{\partial y} \\ \dfrac{\partial N^u \boldsymbol{u}_z}{\partial z} \\ \dfrac{1}{2} \cdot \left(\dfrac{\partial N^u \boldsymbol{u}_y}{\partial z} + \dfrac{\partial N^u \boldsymbol{u}_z}{\partial y} \right) \\ \dfrac{1}{2} \cdot \left(\dfrac{\partial N^u \boldsymbol{u}_x}{\partial z} + \dfrac{\partial N^u \boldsymbol{u}_z}{\partial x} \right) \\ \dfrac{1}{2} \cdot \left(\dfrac{\partial N^u \boldsymbol{u}_x}{\partial y} + \dfrac{\partial N^u \boldsymbol{u}_y}{\partial x} \right) \end{pmatrix}. \tag{5.33}$$

Using the differential operator introduced in Equation 5.19, we notice that Equation 5.33 reduces to

$$\boldsymbol{\varepsilon} = \boldsymbol{D} N^u \boldsymbol{u}\,, \tag{5.34}$$

which, by Equation 5.22, can also be written as

$$\boldsymbol{\varepsilon} = \boldsymbol{B}\boldsymbol{u}\,, \tag{5.35}$$

where the matrix $\boldsymbol{B}$ is of the same form as has been defined in Equation 5.22. The general stress-strain constitutive relationship is written as

$$\boldsymbol{\sigma}'' = \boldsymbol{C}\colon\boldsymbol{\varepsilon} = \boldsymbol{C}\boldsymbol{B}\boldsymbol{u}\,, \tag{5.36}$$

where $\boldsymbol{C}$ is the elasticity matrix containing the elastic properties of the continuum. Substituting the constitutive relationship into Equation 5.26, we get

$$\boldsymbol{M}\ddot{\boldsymbol{u}} + \boldsymbol{K}\boldsymbol{u} - \boldsymbol{Q}\overline{\boldsymbol{p}} - \boldsymbol{f}^{u} = 0\,, \tag{5.37}$$

where **K** is known as the Stiffness Matrix of the system, and takes the form

$$\boldsymbol{K} = \int_{\Omega} \boldsymbol{B}^{T}\boldsymbol{C}\boldsymbol{B}d\Omega\,. \tag{5.38}$$

Note the similarities between Equations 5.37 and 5.12. Finally, we can write Equation 5.37 for the static case, in which no quantities vary with time [Inoue et. al, 2009] and consequently we drop the first term in that equation:

$$\boldsymbol{K}\boldsymbol{u} - \boldsymbol{Q}\overline{\boldsymbol{p}} - \boldsymbol{f}^{u} = 0\,. \tag{5.39}$$

We have now derived the equation that will be used to solve for the quasi-static displacements $\boldsymbol{u}$ at specified nodes in the rock matrix given pressures $\boldsymbol{p}$. Because the equation 5.39 has been developed ignoring the time-variation in displacement, it is still a proxy solution for the reservoir stress equation.

Given any reservoir structure, we can construct the matrices **K** and **Q**. The solution can be obtained explicitly using a linear solver to invert the matrix **K**. The vector of displacements $\boldsymbol{u}$ is then obtained by

$$\boldsymbol{u} = \boldsymbol{K}^{-1} \cdot [\boldsymbol{Q}\overline{\boldsymbol{p}} + \boldsymbol{f}^{u}] \,. \tag{5.40}$$

5.3 Methodology for Implementing Flow and Geomechanics Coupling

Having developed the equations that will be solved for the stress analysis problem, we will now detail the procedure for coupling the particle tracking proxy and the FEM solver.

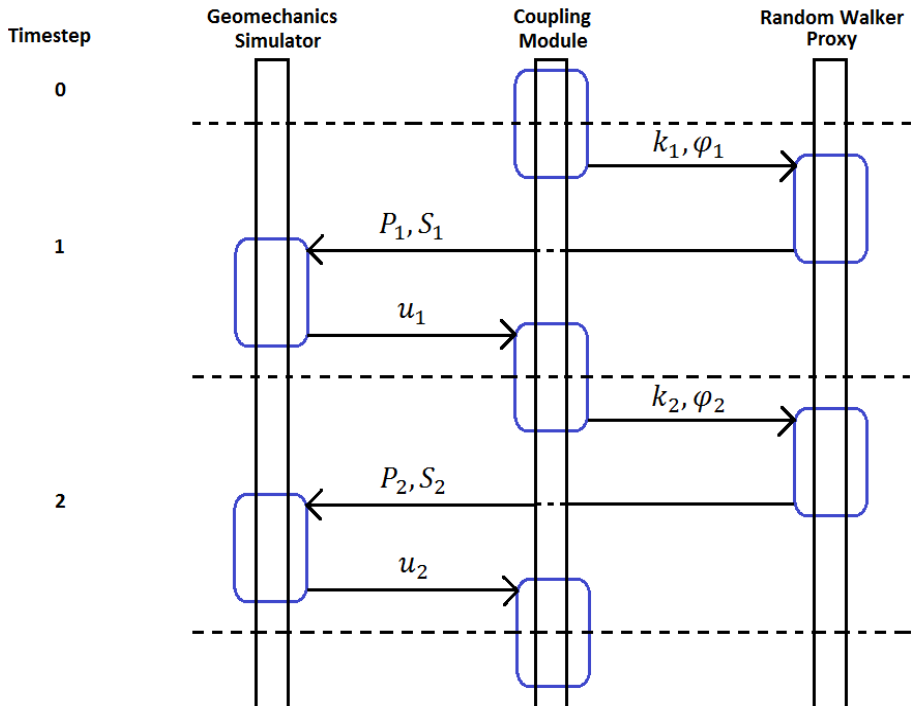

Figure 5.4: Scheme for the automated communication between flow and geomechanics proxies. The time step has to be selected to be the smaller than the relevant time step size for the flow and geomechanics problems

A module was developed in MATLAB with the capability of managing the entire coupling process in a fully automated manner. This module controls the flow of information between the two proxies. At the start of the first timestep, the initial values of the state variables needed for flow simulation (i.e. permeability, porosity etc.) are fed to the particle-tracking proxy where the saturation and pressure responses are evaluated. The produced estimates for pressure and saturation cannot be sent directly to the FEM solver as they must first be manipulated by the coupling module. The reason for this is because of the capability for the proxies to execute simulations on different grid configurations. Thus, input to the

geomechanics grid structure must be interpolated and mapped from its corresponding location in the flow simulation grid structure and vice versa. This task is automatically handled by the created module. The remapped pressures are then sent to the FEM solver, where estimates for displacements are calculated based on the equations formulated in section 5.2, and returned to the module. Here, the displacement estimates are processed and used to re-compute the volumes, porosity and permeability of the flow simulation grid blocks. To compute these changes, we first rebuild the grid structure by relocating the nodes on the original grid according to the displacement solution. With the aid of the MATLAB Reservoir Simulation Toolbox, we can compute the volumes of the elements in the restructured grid. We can now compute the new porosity in each element by multiplying its old porosity by the ratio of the new volume to the old volume:

$$\phi_{new} = \phi_{old} \frac{V_{new}}{V_{old}}, \tag{5.41}$$

where ϕ is porosity and V is the volume of an element. The new permeability is calculated using the Kozeny-Carman relationship and can be represented as follows:

$$k_{new} = \frac{k_{old} {\phi_{new}}^3 (1-\phi_{old})^2}{{\phi_{old}}^3 (1-\phi_{new})^2}. \tag{5.41}$$

The new pore space information is then sent to the particle tracking proxy, and this cycle is repeated until the final timestep.

A benefit of this coupling scheme is that the geomechanics simulation does not have to be invoked at every timestep. The stress calculations need only be carried out when the cumulative pressure variation is significant enough to cause an appreciable change in the structure of the rock. A common practice is to carry out the stress calculations when a 5% pressure change has been observed since the last timestep in which stress calculations

occurred [Amirlatifi, 2013]. This results in a further reduction of the computational costs required for execution.

5.4 Methodology for Variable Mapping Between Flow and Geomechanics Grids

Throughout this report, emphasis has been placed on minimizing the computational expense for evaluating the developed proxies, in order to render the model selection process efficient. In order to further optimize on the computational costs, it would be desirable to use a coarser grid configuration for the geomechanics simulation while maintaining a finer grid refinement level for the particle tracking proxy. This reduces the number of nodes where the displacement changes must be calculated, consequently reducing the matrix dimensions and complexity of the matrix operations to be carried out. In order to allow for this capability, a computationally efficient scheme must be implemented to map variables between the flow and geomechanics grids.

This implementation is best illustrated by providing an example. Figure 5.5(a) shows a color coded variable contained in a two dimensional 5 by 5 grid (the Original grid). The objective is to average the values in this grid to a coarser 4 by 3 grid (the Target grid), while preserving the overall spatial distribution and gradient of the variable in question. A similar technique to downscale and upscale reservoir properties was implemented by Singh in 2014, and by Singh and Srinivasan [2014a; 2014b]. The procedure is detailed in the following steps:

1. Create an intermediate $(m_1 \cdot m_2)$ by $(n_1 \cdot n_2)$ grid where m_1-by-n_1 and m_2-by-n_2 are the dimensions of the original and target grid respectively.
2. Assign variable values to the intermediate grid based on the corresponding locations in the original grid. The creation of the intermediate grid is synonymous to dividing

each grid block in the original grid into an m_2-by-n_2 grid while retaining the variable values.

3. Assign values to each grid block in the target grid, where each value is calculated as the arithmetic average of all values contained within the corresponding space in the intermediate grid.

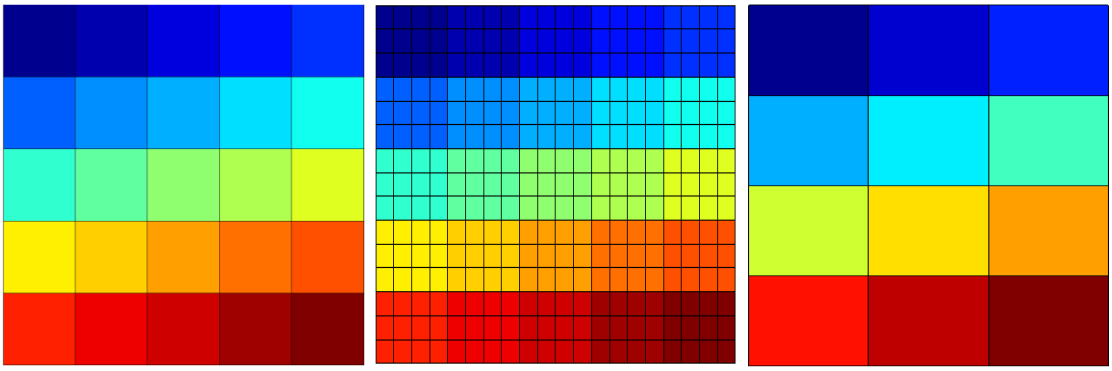

(a)***Original grid*** (b)***Intermediate grid*** (c)***Target grid***

Figure 5.5: Mapping of a color coded variable between 5-by-5 and 4-by-3 grid configurations

The methodology above is illustrated for mapping between two-dimensional grids; however, extension of this procedure to three dimensional grids and with arbitrarily shaped elements is fairly straightforward.

5.5 Validation of Coupled Flow and Geomechanics Proxies

We tested the validity of the FEM solver by comparing the surface deformation response obtained using the proxy to full-physics simulations results obtained using the GEM (CMG®) simulator. We will present the comparisons for both two and three dimensional reservoir grids. The synthetic model used for the two dimensional case is a 100 x 100 grid with a network of high-permeability vertical channels embedded in a low permeability matrix. The CO_2 injector is placed within a channel near the center of the reservoir. Details of the 2D simulations are given in Table 5.1.

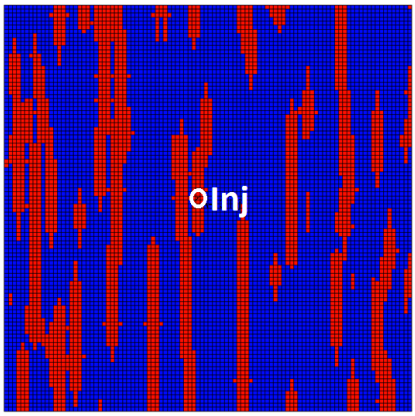

Figure 5.6: Synthetic model showing high permeability channels in a low permeability matrix, with a CO_2 injector at the center of the reservoir

Table 5.1: Coupled flow and geomechanics simulation details

	CMG Geomechanics	Proxy
Grid Size	100 x 100	100 x 100
Elastic Modulus (GPa)	30 (Sand); 20 (Shale)	30 (Sand); 20 (Shale)
Poisson's Ratio	0.15	0.15
Biot Coefficient	2/3	2/3
Coupling Scheme	Iterative Coupling	One-Way Partial Coupling
Finite Elements	8-node Hexahedra	8-node Hexahedra

Surface deformation results are shown in Figure 5.7. The variable plotted in the figures is the magnitude of the vertical displacement at the top of the reservoir, with red regions signifying areas of higher displacement. It is clear that regions of higher connectivity experience greater deformation, and the maximum displacement occurs in regions very close to the well. The comparison shows that the shape of the surface deformation response is reasonably similar between the two simulations. One major difference is that the gradient from high deformation to low deformation regions is much more gradual in the proxy response. An explanation for this is that the particle tracking proxy overestimates the tendency for the CO_2 plume to diffuse outside the main migration pathways, as was discussed in chapter 4. This in turn is because in the particle tracking proxy the pressure estimate is

purely assessed in terms of the proximity of particles to the injection locations, thus, the effects of reservoir connectivity is underestimated.

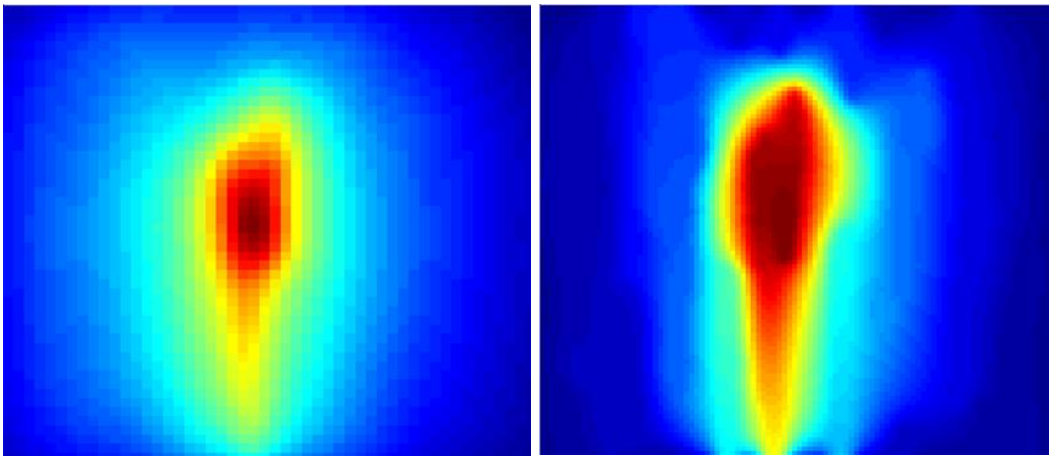

Figure 5.7: Simulation results showing the top vertical displacement for the coupled proxies (left) and CMG geomechanics simulator (right)

It was assumed in the example above that the reservoir was homogeneous in terms of the structural properties of the rock; that is, similar elastic properties were assigned to the entire grid. In the next example, we validate the results for a 2D heterogeneous case. We assigned unique elastic properties to each facies in the model shown in Figure 5.6 and re-executed the simulation using the coupled proxies; results are shown in Figure 5.8. It is evident that there are sharp decreases in the vertical displacement that can be traced along the high permeability channels. This response indicates that the sand channels are more resistant to deformation than the surrounding mudstone matrix, as should be expected based on their elastic properties.

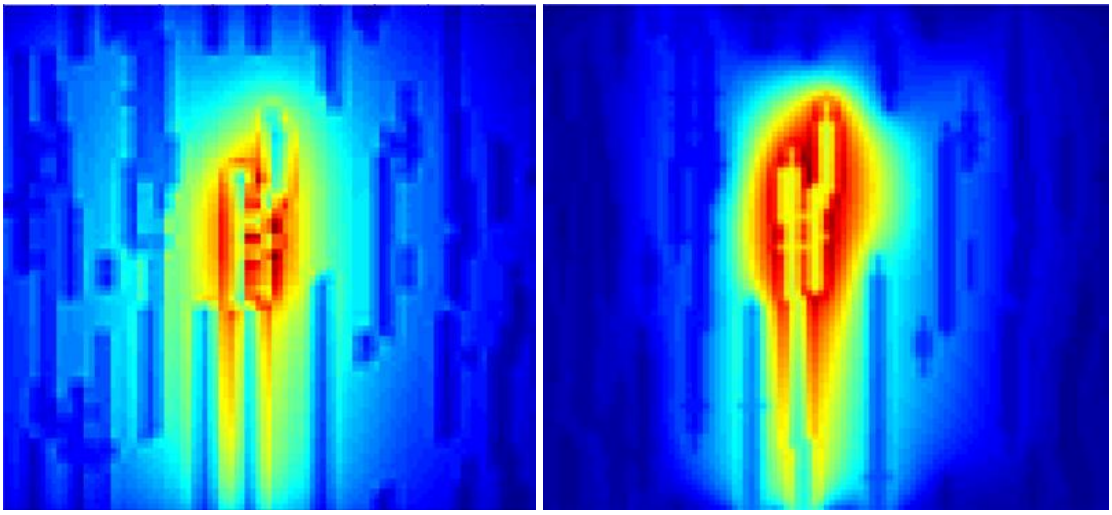

Figure 5.8: Heterogeneous case - simulation results showing the top vertical displacement for the coupled proxies (left) and CMG geomechanics simulator (right)

Finally, we compare simulation results for the three dimensional 55 x 50 x 4 grid shown in Figure 5.9. Instead of an idealistic model with sharply contrasting permeability streaks, we used a more realistic model generated using a Sequential Gaussian Simulation (SGSIM). The permeability field is more dispersed and the gradient between high and low permeability regions is more gradual. We have placed two CO_2 injectors A-12 and A-13 in the model, both connected to the bottom layer of the reservoir. The mechanical properties are homogeneous throughout the domain, and the elastic properties used are the same as those shown in Table 5.1.

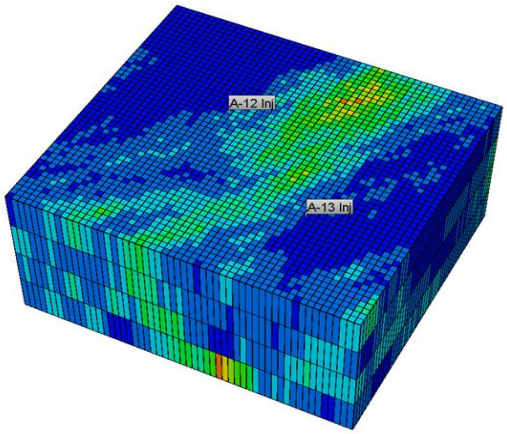

Figure 5.9: Three-dimensional permeability model generated using SGSIM, with two CO_2 injectors connected to the bottom layer of the reservoir

The surface deformation response map shows two peaks at the well locations, as expected. The response looks similar to a superposition of two deformation fields, where each one is produced from the displacement induced by each injector. A more thorough examination of the result produced by CMG shows that the deformation at the A-13 injector is more suppressed. This is a direct consequence of the boundary conditions imposed in the full-physics simulation. In most CO_2 injection simulations, infinite volume boundaries are assumed at the edges of the grid to simulate the effect of a connected boundary aquifer. Thus in the CMG simulation, some of the pressure generated from the A-13 injector close to the reservoir boundary is accommodated by the connected aquifer. In the simulation of the saturation response, the boundary effects could be represented by simulating a sink along the edges that does not allow the particle count to increase. However, in the formulation of pressure estimation by the particle tracking proxy, these boundary effects cannot be easily represented because the pressure front migrates to the boundary much faster than the saturation front. Because of this, the induced displacement could sometimes be overestimated when the injector is influenced by boundary conditions.

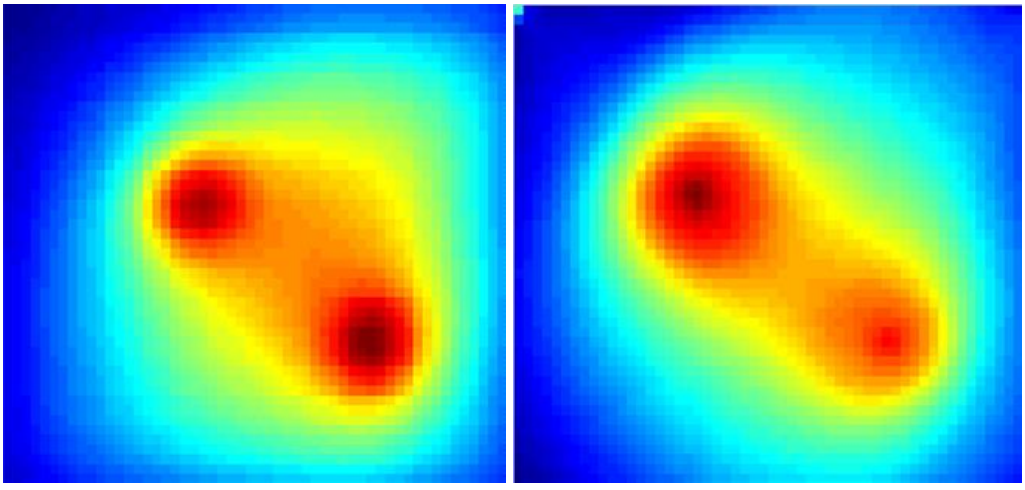

Figure 5.10: Vertical displacement at the top layer of a three dimensional grid for the coupled proxies (left) and CMG geomechanics simulator (right)

Table 5.2: Comparison of Execution Times for Proxy and Full Physics Geomechanics Simulations

	PROXY (seconds)	CMG (seconds)
2D	**6**	**64**
3D	**76**	**4978**

Table 5.2 shows the computational time expended to generate the results presented in this chapter. It is clear that the proxy offers a significant advantage over full physics simulation in terms of computational time, while reasonably reproducing the effects of the unique rock structure and connectivity on the geomechanical response.

5.6 Chapter Summary

In this chapter, we presented the formulation of the stress equilibrium equations necessary to obtain the solution for the displacements in the reservoir when a change in pore pressure is imposed. These equations were built into an FEM solver, and coupled with the particle tracking proxy developed in Chapter 4. Comparisons of proxy solutions with full physics results show that the proxy offers an advantage in terms of computational time, while producing reasonable solutions. In Chapter 6, we will use a synthetic model to demonstrate how proxy solutions can be integrated into the model selections scheme, and used to group models with similar geologic characteristics.

CHAPTER 6: HISTORY MATCHING AND INTEGRATION OF REMOTE SENSING DATA WITHIN THE MODEL SELECTION FRAMEWORK

In this chapter, we will demonstrate the application of the overall model selection scheme for history matching and integration of remote sensing data for a synthetic reservoir. Our goal is to compare the accuracy and uncertainty of the performance forecast obtained for the prior and posterior model ensembles. If the implementation of model selection is to be deemed advantageous, the forecasts from the posterior ensemble should be more representative of the reference model, and exhibit uncertainty that is significantly reduced relative to the prior ensemble.

6.1 The Reference Model

In this section, we present features of the reference model shown in Figure 6.1. We explore its topography and geologic characteristics, and how they affect the response and selection of posterior models. The model was constructed on a 100-by-100-by-3 grid, with high permeability channels emplaced in a low permeability matrix. A CO_2 injector is placed within a channel at the center of the grid and connected to the bottom layer.

Figure 6.1: The reference model is a channelized system with complex topography. Note that the vertical axis has been exaggerated here for visualization

6.1.1 Topography

The topography of a potential aquifer is consequential to the direction of flow and the eventual spatial distribution of the CO_2 plume. As CO_2 is less dense than aquifer brine, buoyancy effects cause the plume to migrate towards areas of higher elevation. This migration is the result of the complex interplay between the effects of gravitational and viscous forces. The dominance of one force over the other is dependent primarily on the structure and geology of the reservoir in question. With the exception of regions in the immediate vicinity of wells, we should expect the effects of viscous forces to be far more pronounced in the reference model, due to the sharp contrast in permeability between the channels and the matrix. If the model were more homogeneous however, flow could occur preferentially towards regions of higher topography, depending on the magnitude of the vertical permeability. In this chapter, we utilize the same rock structure and topography for all models, and we will focus on updating only the permeability and porosity fields.

6.1.2 Channel Orientation

The orientation of the channels primarily dictates the shape of the CO_2 plume and rock deformation response map. As expected, the contribution of these effects vary spatially based on proximity to the injection well; channels closer to the well have a higher contribution than those further away. By mapping accurately, the orientation of channels, the model selection algorithm should be able to reproduce the general shape of the main migration path in the reference. Additionally, models that have similar connectivity patterns in regions closer to the well should be considered more credible than those that appear similar in regions further away from the well. In the reference model shown in Figure 6.1, the primary channel runs across the injector towards the top left and bottom right corners of the grid. We should thus expect the selected models to exhibit similar characteristics.

6.1.3 Full Physics Simulation: Saturation and Surface Deformation Results.

Figure 6.2 shows the results of the full physics simulation after 1100 days of injection in the reference model. Both the saturation and surface deformation responses conform to expectations based on the orientation of the main migration path depicted in Figure 6.1. These results illustrate how the major reservoir heterogeneity controls the main migration paths and how the surface deformation map should provide sufficient information to select the most appropriate group of reservoir models. The results also indicate that the surface deformation map by itself cannot be used to delineate the crisp geometry of channels. Instead that map has to be combined with prior geologic information in order to delineate the channels so that future migration of the CO_2 plume can be predicted accurately.

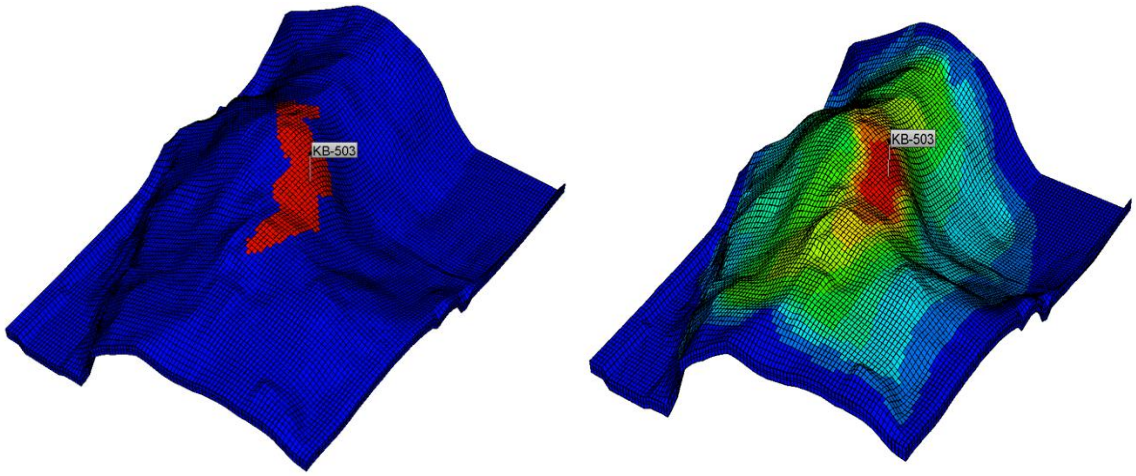

Figure 6.2 CMG simulation results for saturation (left) and surface vertical displacement (right) in the reference model

6.2 Model Generation

This is the first step in the model selection scheme shown in Figure 3.3 (reproduced in Figure 6.3 for convenience). As discussed in Chapter 3, the initial model set must be generated such that it reflects the current uncertainty in reservoir geology, while being conditioned to prior available data. In this example, no conditioning data was used to constrain the permeability at any point in the reservoir. The models were however created

using a Sequential Normal Equation Simulation and a training image to create channelized pathways in the matrix. The channels had a high permeability of 250 md and the matrix had a much lower permeability of 1 md. Other factors such as the shape, size, orientation and frequency of the embedded channels cannot be ascertained based on the sparse conditioning information retrieved from the reference and thus, these parameters vary significantly across the models. Three sample realizations out of 300 generated models are shown in Figure 6.4; notice the variations in channel characteristics.

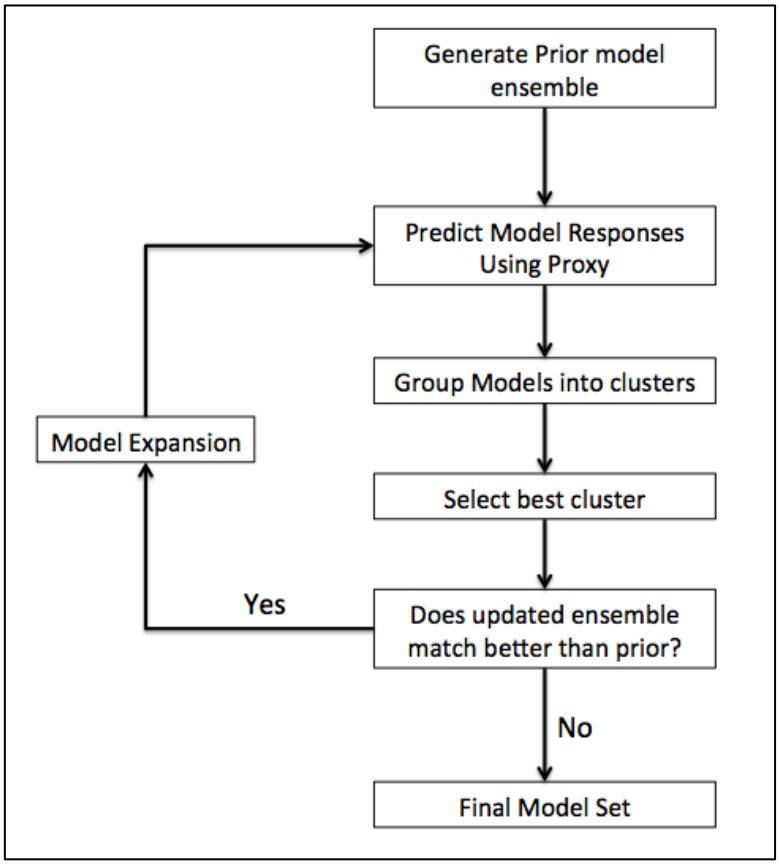

Figure 6.3: Schematic of the model selection algorithm

Figure 6.4: Sample realizations generated as part of the prior suite of models

6.3 Response Prediction

The next step is to produce a fast approximation of saturation, pressure and surface deformation using the proxies we have developed. We performed proxy simulations for all 300 models in the prior ensemble, with an average execution time of about 30 seconds per model; in comparison, the time taken to obtain simulation results for the reference model was 6695 seconds. Figure 6.5 shows the saturation and top surface vertical displacement responses for the sample models presented in Figure 6.4. It can be observed that the models exhibit a wide variation in plume and vertical displacement characteristics.

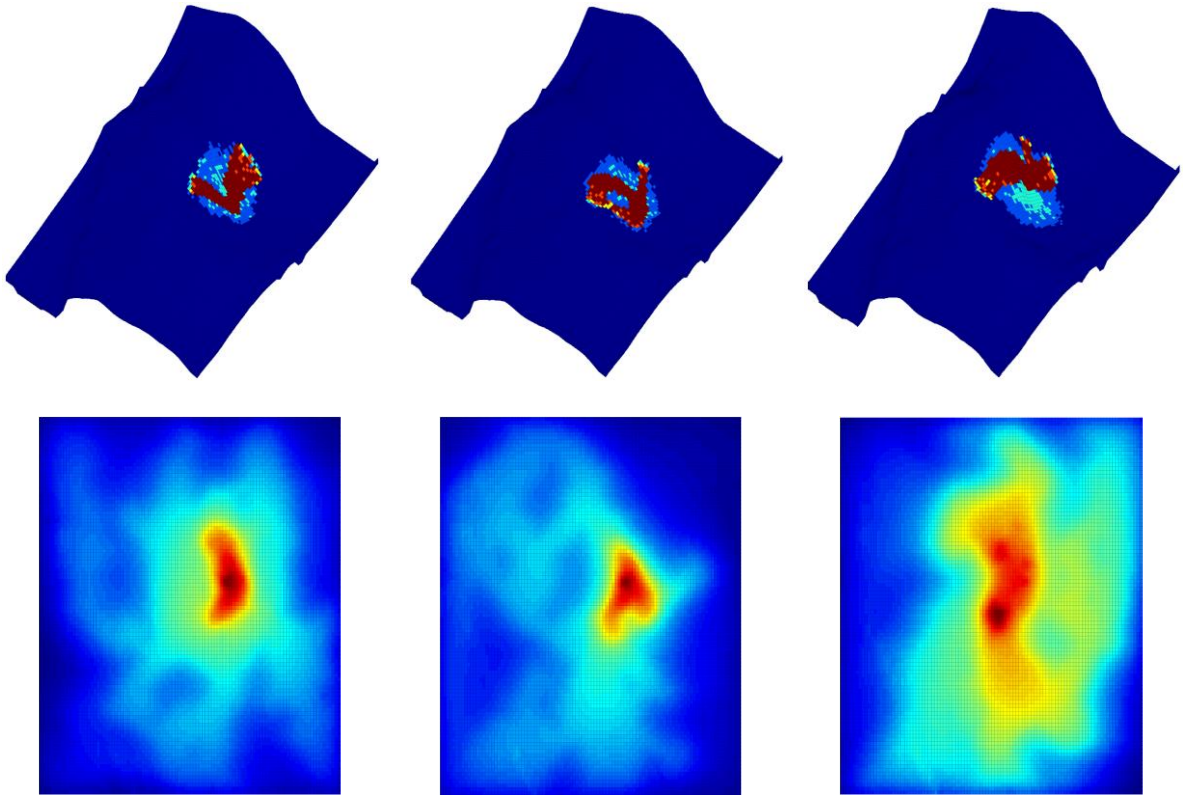

Figure 6.5: Proxy simulation results for saturation (top) and surface vertical displacement (bottom) for the sample models shown in Figure 6.4

6.4 Multidimensional Scaling and Clustering of Model Responses

As discussed in Chapter 3, multidimensional scaling (MDS) is a way to reduce the dimensionality of model responses such that they can be projected and visualized on an orthogonal set of axes. For each model in this example, we have 30000 responses for saturation and 10000 for surface deformation (we consider vertical displacement for only the grid blocks on the top layer). Note that while the exhaustive saturation map was used to cluster the models, to select the best models, we will only use measures that can be routinely obtained in the field such as well bottom-hole pressures and surface deformation. By invoking the MDS algorithm, we reduce this 40000 dimensional parameter space to three equivalent metric dimensions and the response of each model is plotted in this 3 dimensional space.

Having projected the models in 3D space, we used the k-means clustering algorithm (detailed in Chapter 3) to group models based on proximity to optimally specified centroid locations. Recall that the centroid locations were established by solving an optimization problem according to the following algorithm:

The algorithm proceeds as follows:

6. Choose *n* initial centroids.
7. Compute point-to-cluster-centroid distances for all observations in each centroid.
8. Assign each observation to the cluster with the closest centroid.
9. Recompute the cluster centroids as the average of the observations in each cluster.
10. Repeat steps 2 to 4 until cluster assignments do not change.

According to the rule of thumb presented in Equation 3.2, the number of clusters should be equal to the square root of half the number of observations. Thus, for the 300 model observations, the prescribed number of clusters is 12. Figure 6.6 shows the model responses projected in 3D space and their cluster assignments visualized by color. For better visualization, we also show the clustering results as viewed from the x-y, x-z and y-z planes.

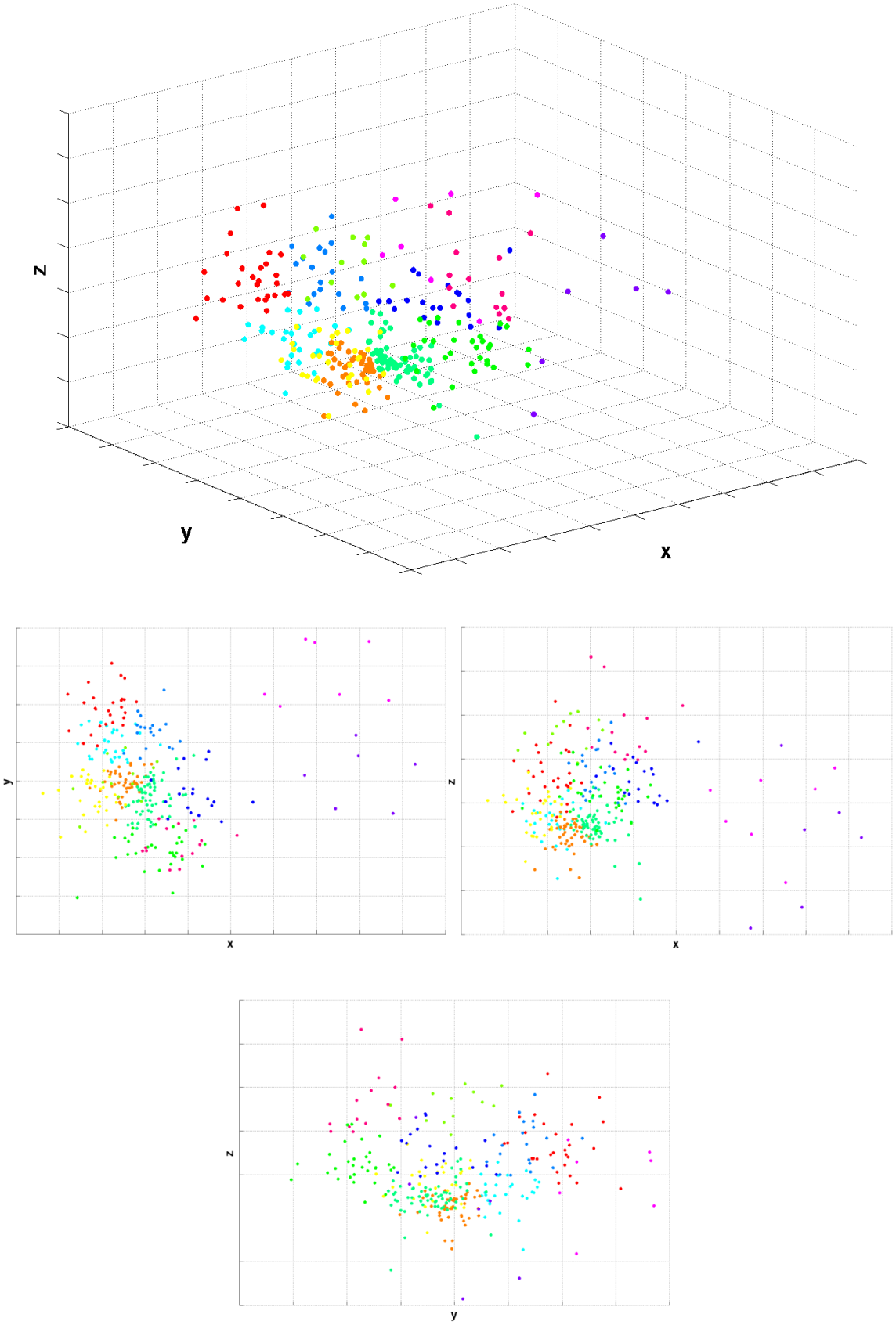

Figure 6.6: Results of MDS and clustering of 300 model observations, viewed from 4 different angles

6.5 Selection of best-fit Cluster

Having grouped models into clusters, we must now select the cluster that is most characteristic of the reference model. First, we select a representative model from each cluster, determined as the one whose projected response is closest to the cluster centroid (Note that the cluster centroid is just a point in space and not a model). Next, we must accurately produce forecast from these representative models so that they can be compared to the reference data. For this purpose, we performed full-physics simulations for the 12 cluster representatives, generating output data for bottom-hole pressures and surface deformation. Injection rates weren't compared because we used rate constraint specifications for the simulation; however, it is possible to compare rate data in cases where fluctuations in injection rates are the well measurements and the wells are operated at constant bottom-hole pressure. Selecting the best-fit model is straightforward: we choose the model that minimizes the squares of the forecast errors summed through time and space. This requires the computation of the objective function written in Equation 6.1

$$Objective\ function = \sum_{i=1}^{N} \frac{\left(d_{sim,i} - d_{ref,i}\right)^2}{var\left(d_{sim,i}\right)}, \tag{6.1}$$

where *d* is the comparable data (surface deformation and bottom-hole pressure), and the subscript *i* is a spatial or temporal index of the data. d_{sim} is the simulated response of the cluster representative computed by a full physics simulator, d_{ref} is the observed response for the reference model, and $var(d_{sim,i})$ is the variance of $d_{sim,i}$. The best-fit cluster is the one that yields the lowest objective function value.

Figure 6.7 shows the surface deformation results for the full-physics simulation of the 12 representative models. For visual comparison, the reference model is also shown at the top of the figure. An interesting observation can be made if we examine the shape of the

deformation region at the bottom right of the figure (highlighted in red): just like the reference model, the region of highest deformation runs from the injection location towards the top left and bottom right corners of the grid. As discussed in Chapter 5, the surface deformation map could give an indication of the pressurized regions, and hence, orientation of the main migration pathways in the reservoir. This suggests that the main migration path in the reference and Cluster 12 models are similar in term of their orientation. Figure 6.8 shows a comparison of the bottom-hole pressure solutions between the reference model and the 12 cluster representatives. Again, Cluster 12 provides the best match with the reference solution.

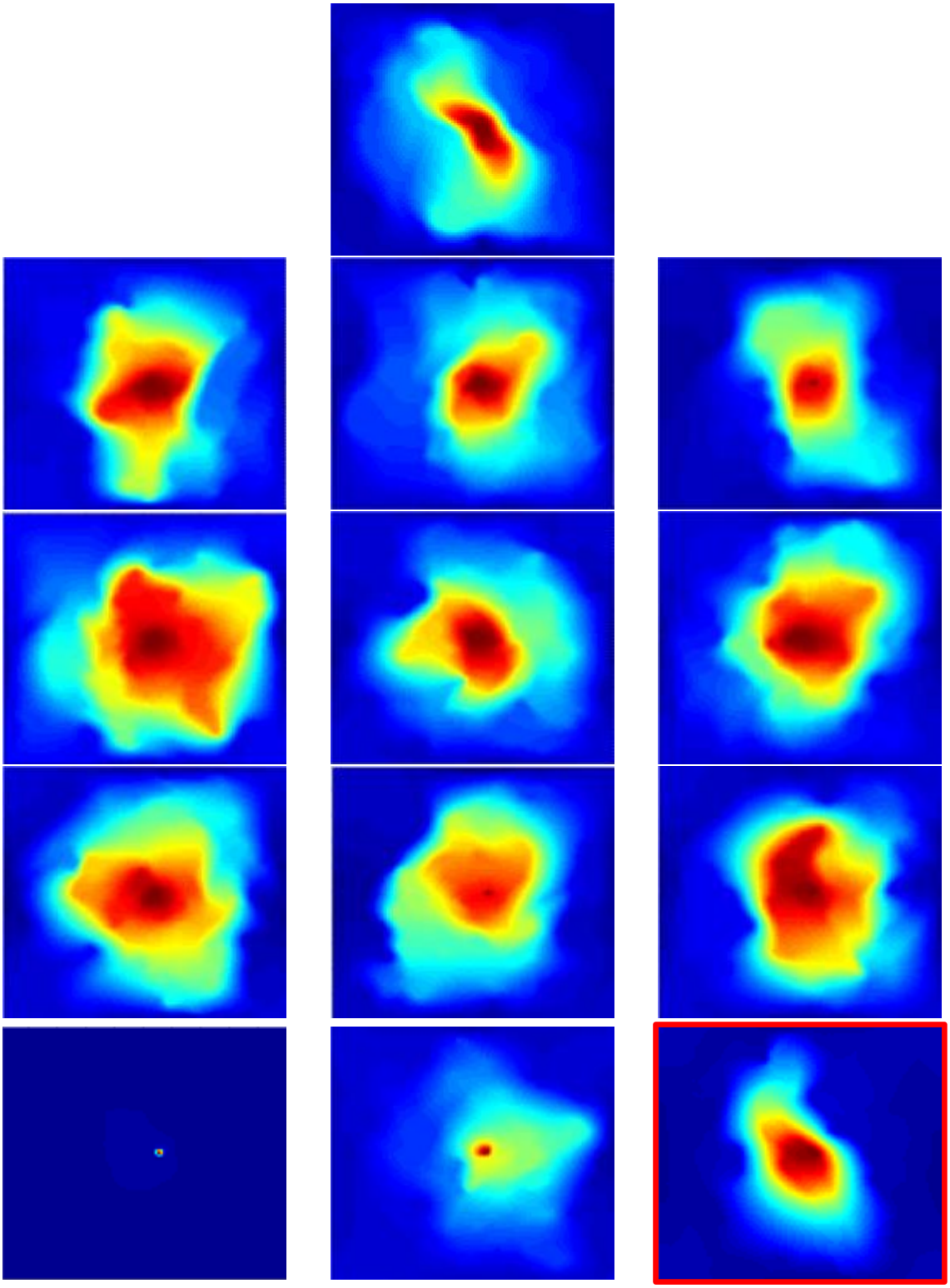

Figure 6.7: Full physics simulation of surface deformation for 12 cluster representatives. Solution for the reference model is shown at the top of the figure. The representative for the selected cluster (Cluster 12) is highlighted in red

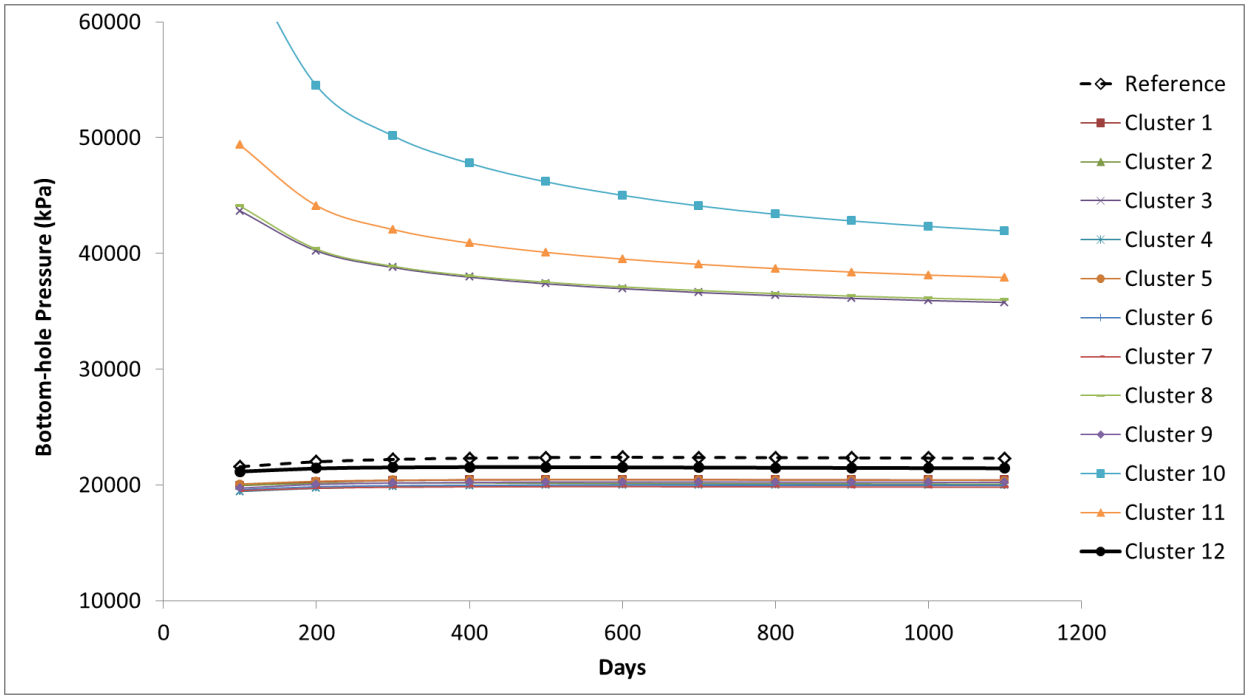

Figure 6.8: Comparison of bottom-hole pressures

So far, visual comparisons suggest that Cluster 12 yields responses closest to the reference model. For a mathematically-based conclusion however, we calculated the objective function for all representative models. Figure 6.9 shows the normalized objective function value for the 12 clusters. As expected, Cluster 12 produces a value of 0, meaning that it exhibits the least deviation from the reference solution. This however does not mean that it matches exactly with the reference data. The objective function values are normalized from 0 to 1, such that the cluster with the lowest deviation is assigned a value of 0 and that with the highest gets a value of 1. We now have adequate justification to select Cluster 12 as the posterior ensemble.

Selection of the 12th cluster means that all models grouped into cluster 12 are members of the posterior set that are equally likely to reflect the observed response characteristics. Figure 6.10 shows the selected cluster models responses projected in 3D space. To investigate whether the main migration pathways in the selected cluster run along the same orientation as that in the reference model, we plot the corresponding permeability

fields of the models in cluster 12 in Figure 6.11. It is evident that near the injector, the selected models exhibit a similar channel orientation to the reference.

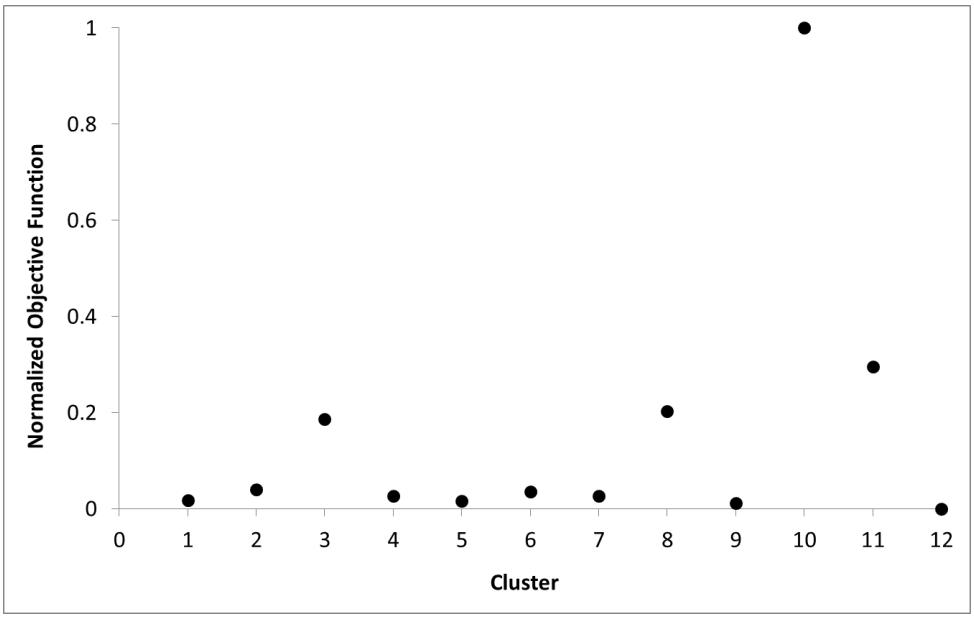

Figure 6.9: Normalized objective function values for 12 clusters. Cluster 12 is selected, as it yields the minimum value

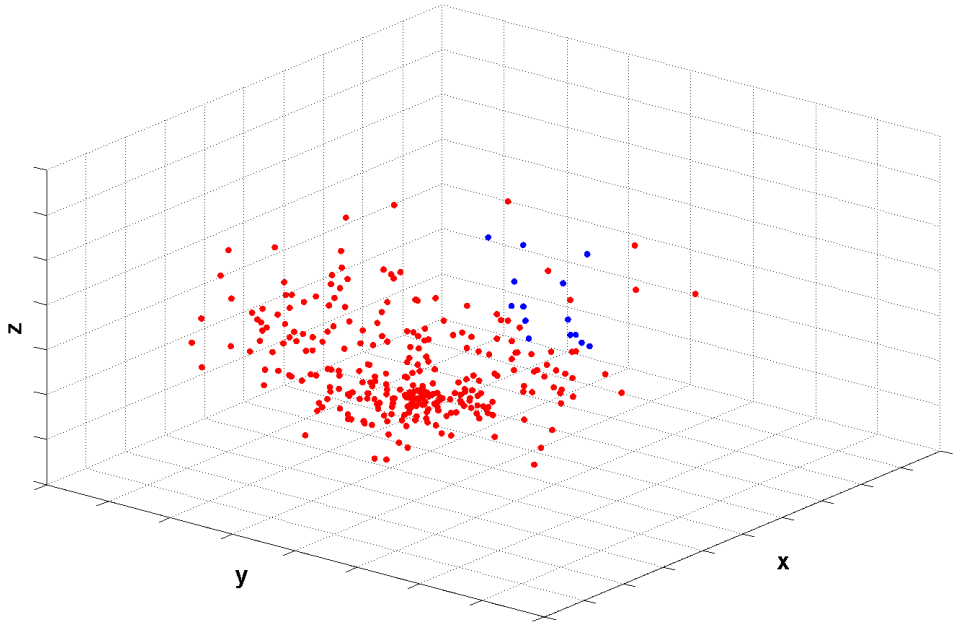

Figure 6.10: The selected cluster (shown in blue) projected in 3D space with all other models (red)

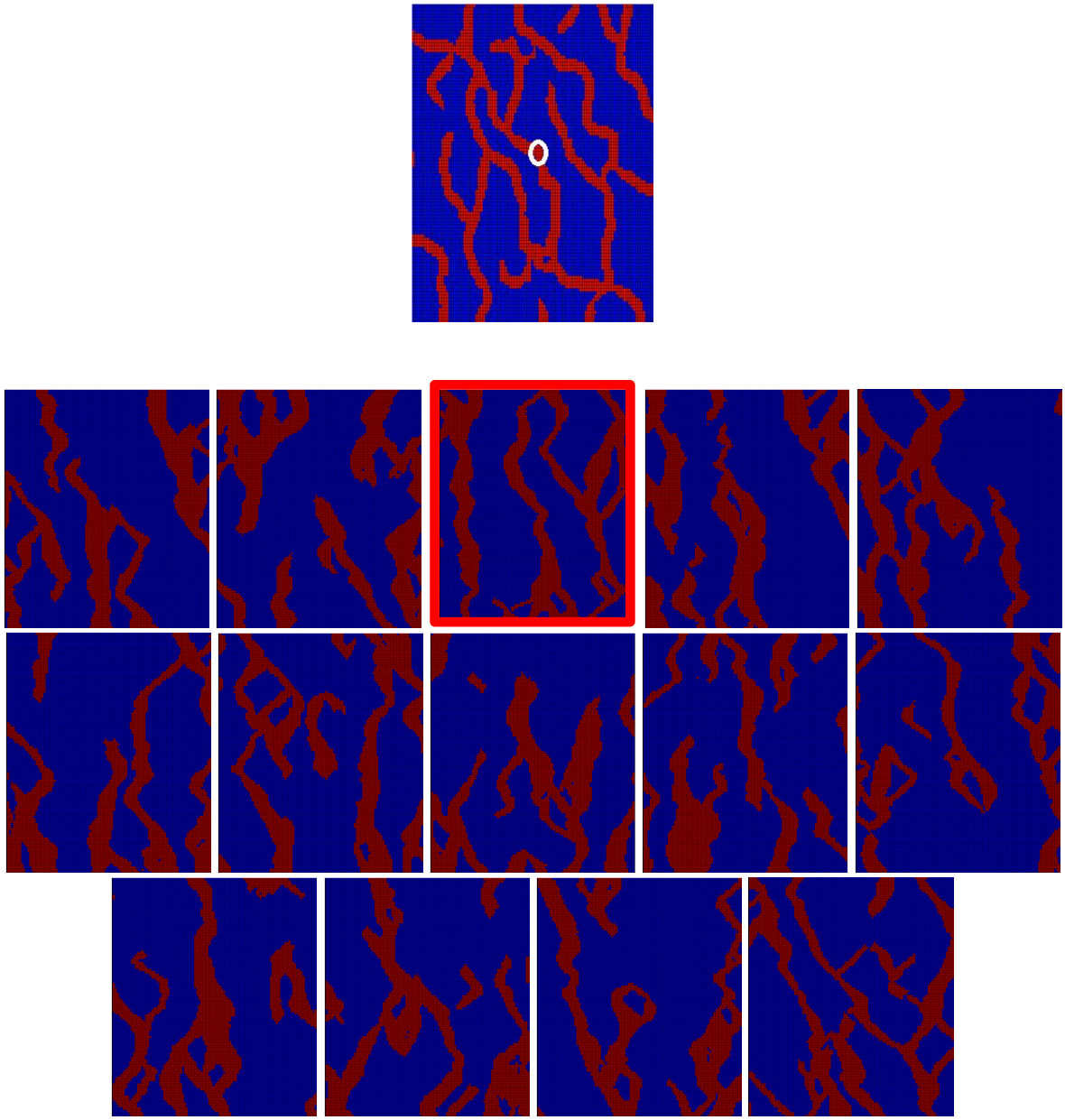

Figure 6.11: Top layer of the permeability field for 14 selected models. Main migration paths in the posterior ensemble (bottom) exhibit similar orientation to reference model (top). White circle indicates the injector location. The representative model is highlighted in red

The mean permeability field of the posterior models shown on the left in Figure 6.12 corroborates our conclusion regarding the representation of the main permeability channel in the members of the posterior set. At the injection location, the permeability streak is oriented towards the top left and bottom right corners of the grid. For comparison, the ensemble mean for the prior model population is also shown on the right.

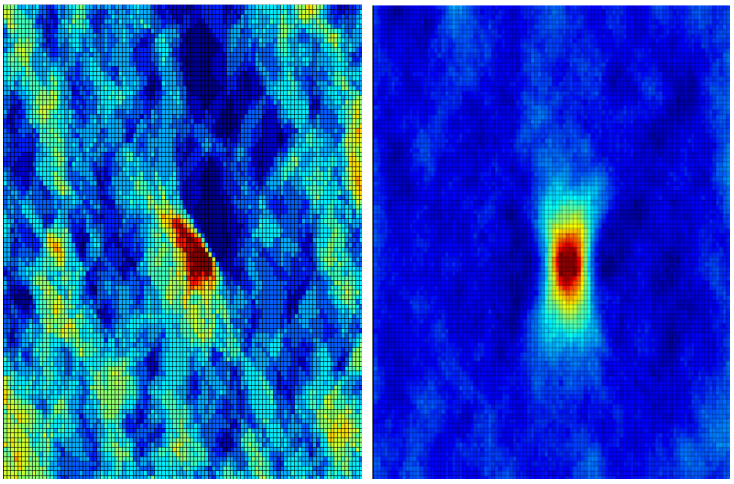

Figure 6.12: Top layer of the mean permeability field of the posterior (left) and prior (right) ensembles

6.6 Chapter Summary

In this chapter, we demonstrated the application of the model selection scheme to the history matching of a synthetic model with complex topography. To make up the prior ensemble, channelized models were generated with varying orientations and spatial distributions. By applying model selection, we showed that we were able to discriminate and select a subset of models which exhibit similar characteristics to the reference model. It is important to realize that it is impossible to characterize the channels based solely on the deformation data obtained from the reference solution. Rather, we achieved this by grouping models based on their flow characteristics, and then history matching with both the deformation data with injection data.

CHAPTER 7: FIELD CASE APPLICATION: IN SALAH PROJECT, ALGERIA.

This chapter will demonstrate the application of the overall model selection scheme to an ongoing CO_2 sequestration project at In Salah Algeria. Each section will provide sufficient detail on specific components of the model selection scheme, starting from the development of prior models, to the selection of posterior models. We will compare results obtained by constraining models using only the well data, to those obtained by incorporating geomechanical information into the model selection scheme. We then attempt to predict observations detected in the field by examining the geological information in the selected models.

7.1 Description of the Project

The In Salah Gas Joint Venture in Algeria is an ongoing CO_2 storage project that has been operating since August 2004. The Krechba field is part of the In Salah gas field development, and is currently the largest onshore CO_2 storage site in the world [Iding and Ringrose, 2009]. At Krechba, CO_2 from several gas fields is removed from the production stream and injected into the deep saline carboniferous formation away from the producers. Figure 7.1 shows an aerial view of the project, featuring three horizontal CO_2 injectors (KB-501, KB-502 and KB-503, noted by blue dots and lines) and four gas producers (in red).

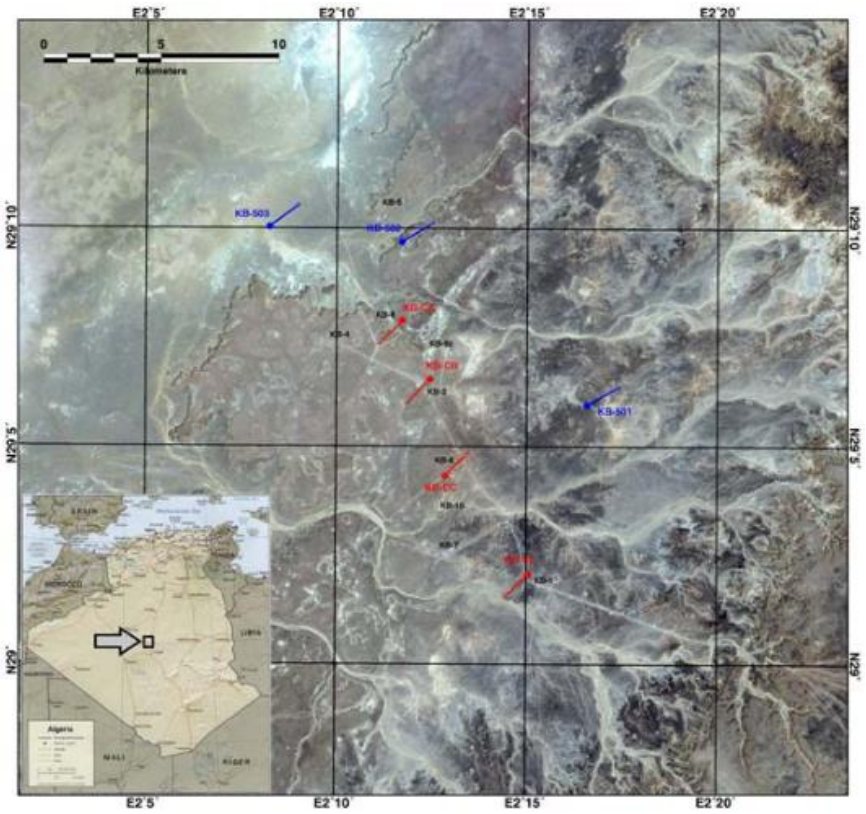

Figure 7.1: Image of the In Salah project showing CO_2 injection wells (blue) and gas production wells (red) [Onuma et al., 2008]

The use of satellite air-borne radar interferometry (InSAR) has been valuable in the detection of subtle ground deformation above the injection wells [Mathieson et al., 2009]. Data was acquired to characterize the magnitude of subsidence and uplift above the injectors and producers spanning from July 2003 to May 2008 [Onuma et al., 2008]. These time-varying surface deflection maps play a key role in our efforts to characterize the permeability field of the Krechba formation and predict the future migration of the CO2 plume, as we will see later in this chapter.

Reports from drilling studies in 2002 suggest the existence of fractures in the Krechba formation that could play a dominant role in plume migration [Iding and Ringrose, 2009]. In this chapter, we travel back in time to December 2006 when the first remote sensing information was gathered and consider the spatial distribution and orientation of these fractures as unknown parameters; thus, these factors will be unconstrained in the prior

ensemble. Our objective is to test whether the model selection algorithm can produce posterior models that will adequately predict:

1. The early arrival of CO_2 at an abandoned well, KB-5, northwest of KB-502 in June 2007.
2. The downwards migration of CO_2 around KB-502.
3. The prevailing NW-SE orientation of the CO_2 plume throughout the field.

We will use the surface deflection map (Figure 7.2) acquired in December 2006 as the reference data for history matching. Notice the preferential NW-SE orientation of deformation in the vicinity of the injector wells.

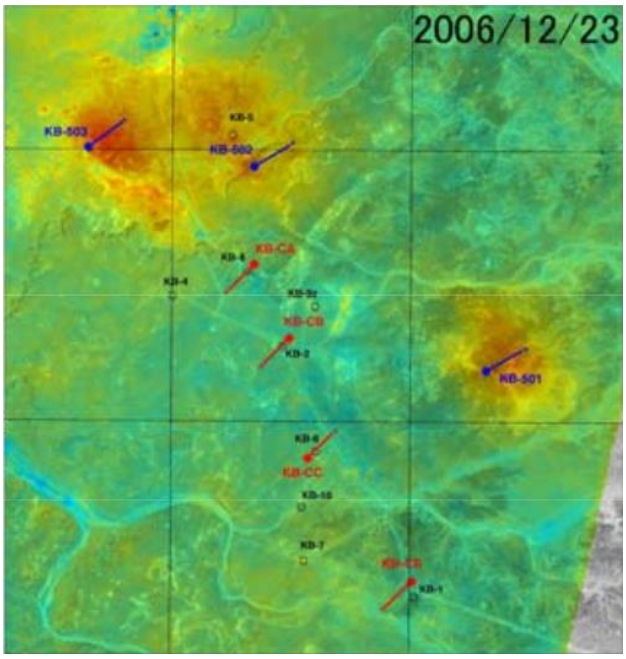

Figure 7.2: Surface deformation map at the site in December 2006 [Onuma et al., 2008]

7.2 Generation of Initial Model Set

Topography

Figure 7.3 shows the reservoir topography built on a non-orthogonal corner point 100 x 100 x 3 grid structure, using the surface contour map shown on the left.

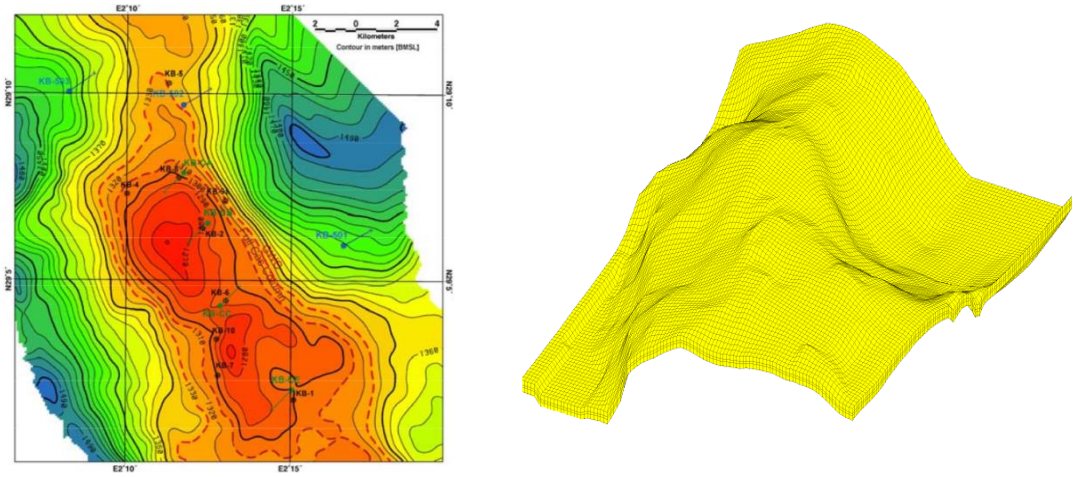

Figure 7.3: Reservoir topography contour map (left) and the resulting grid structure (right) [Wright, 2007]

Permeability

As discussed earlier, the initial model set must be able to capture the uncertainty in the spatial distribution and orientation of fractures. We generated 400 models using Sequential Indicator Simulation (SISIM), with thin permeability streaks to mimic the placement of fractures within the reservoir. The orientation of the fractures and their length distribution are assumed to be unknown. Since flow through the fracture occurs much faster than flow through the matrix, we assumed a very high permeability within the streaks relative to the matrix. Figure 7.4 shows some samples of the generated models.

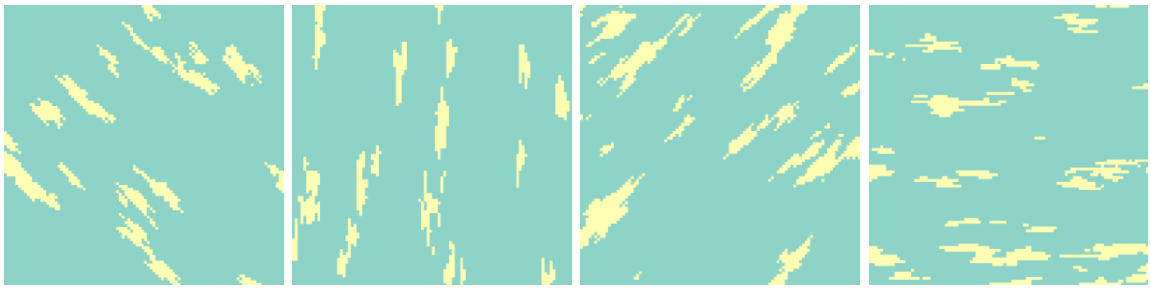

Figure 7.4: Sample models generated using SISIM

7.3 Simulation Inputs

In this section, we present the inputs used to perform the full physics and proxy simulations.

7.3.1 Initial Conditions

The initial reservoir saturations were established by performing gravity-capillary equilibrium calculations (built in CMG). A reference pressure of 17485 kPa was established at a depth of 1300 m and used to calculate the initial reservoir pressures using the hydrostatic gradient. The water-oil and gas-oil contacts were set at depths of 2000 m and 1300 m respectively, and a water saturation of 100% was established both below the water-oil contact and in the oil zone, indicating a brine-filled aquifer. The gas cap was set to contain 100% CH_4.

7.3.2 Relative Permeability

The water-gas relative permeability chart used for the simulation is shown in Figure 7.5.

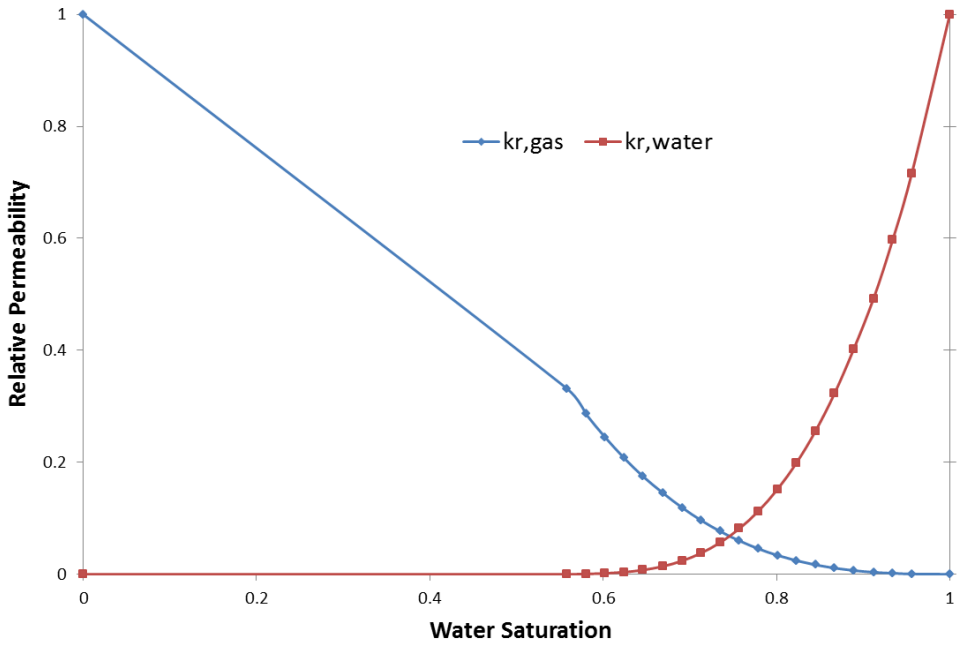

Figure 7.5: Water-gas relative permeability chart

7.3.3 Geomechanics Inputs

The reservoir was assumed to be homogeneous in terms of its elastic properties. Specific details used for the geomechanical simulation are given in Table 7.1.

Table 7.1: Geomechanics simulation details

	CMG Geomechanics	Proxy
Grid Size	100 x 100 x 3	100 x 100 x 3
Elastic Modulus (GPa)	30	30
Poisson's Ratio	0.15	0.15
Biot Coefficient	2/3	2/3
Coupling Scheme	Iterative Coupling	One-Way Partial Coupling
Finite Elements	8-node Hexahedra	8-node Hexahedra

7.3.4 Injection Data

A summary of the CO_2 injection schedule for the three injectors is shown in Figure 7.6.

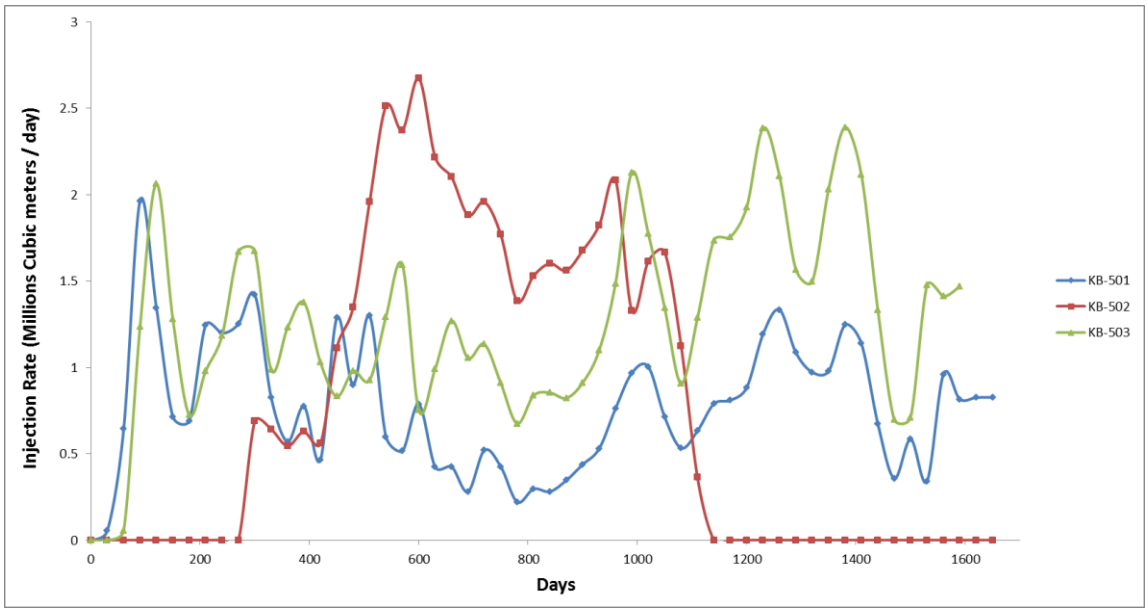

Figure 7.6: CO_2 injection schedule starting May 1st 2004

7.4 Response prediction and Model Clustering

Flow and geomechanics responses from the prior models were obtained using the coupled proxy developed in Chapters 4 and 5. Once again, the model responses were projected onto a three dimensional space, and this time around, we sought to group the models into 14 clusters, which is the recommended number based on the rule of thumb

introduced in Chapter 3. Figure 7.7 presents a visualization of the 400 models projected onto a three dimensional space, with cluster assignments specified by color.

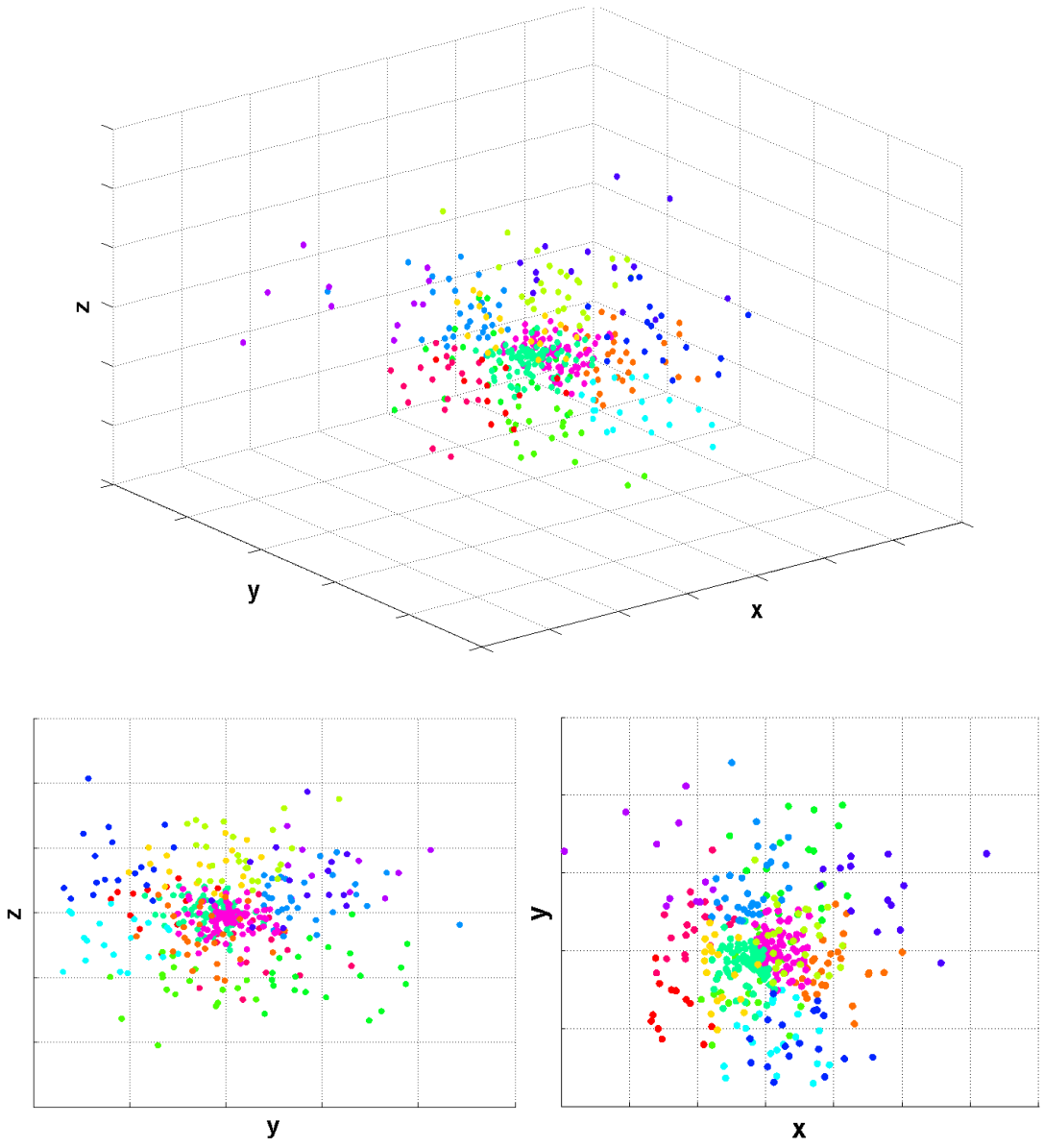

Figure 7.7: Results of MDS and clustering of 400 model observations in three-dimensional space. Two additional angles included for clarity

7.5 Cluster Selection Using Only Injection Data

The representative models from each cluster were analyzed using a full physics simulator (CMG Geomechanics) to produce output for both well bottom-hole pressures and surface deformation. First, we attempt to perform the next step in model selection by

matching only the well information between the field and the candidate models. By doing this, we aim to demonstrate that the posterior model set cannot be sufficiently constrained to reproduce all field observations using only injection data. By introducing the use of surface deflection measurements, we obtain a better reproduction of the geological characteristics in the actual reservoir. The bottom-hole pressures histories for 14 clusters, along with the observed field measurements, are shown in Figure 7.8 for the three injector wells.

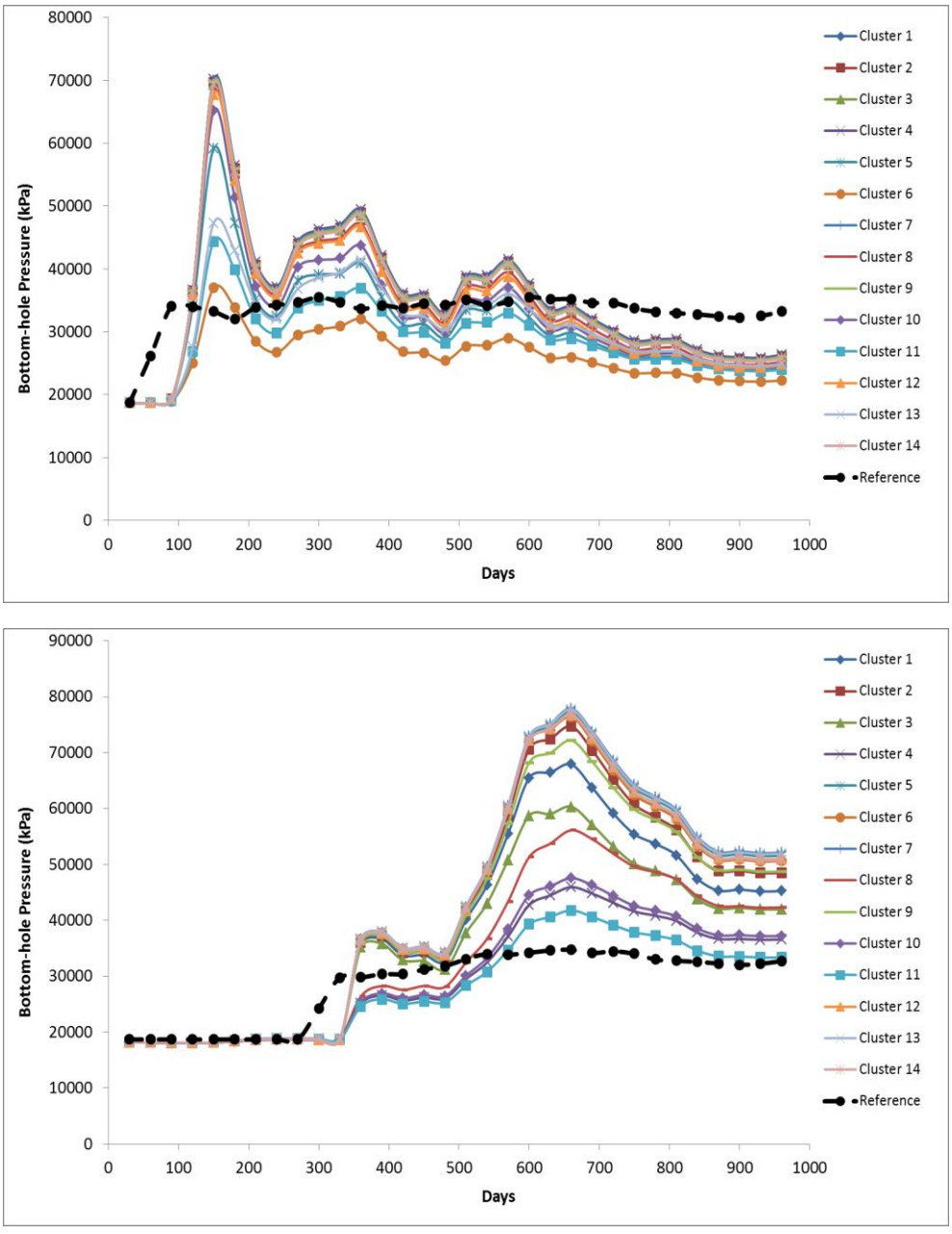

Figure 7.8: Comparison of bottom-hole pressures for wells KB-501 (top), KB-502 (center), KB-503 (bottom)

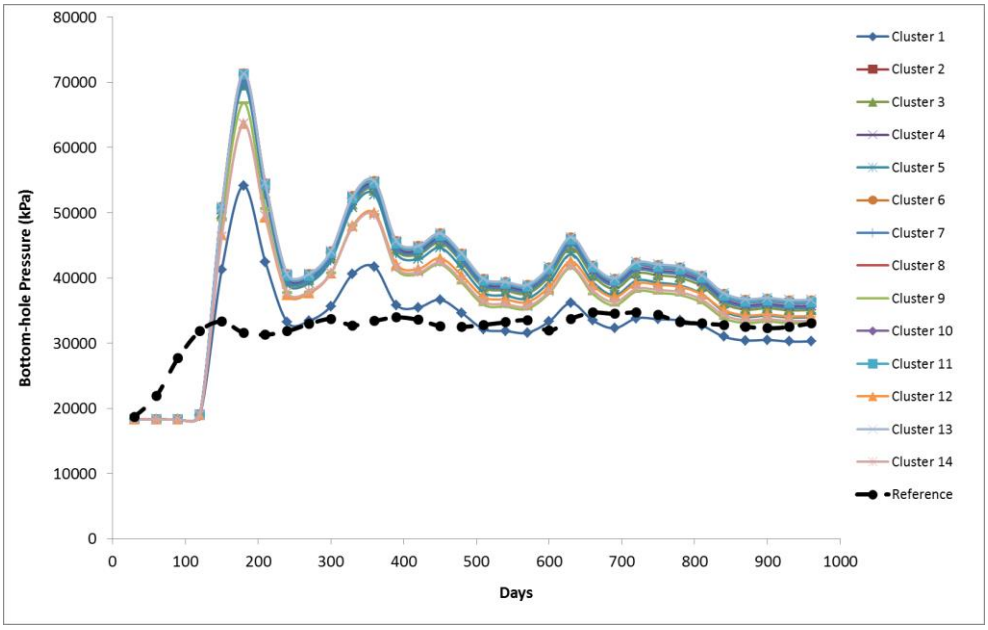

Figure 7.8, cont.

The formulation of the objective function used to select the best-fit cluster is

$$Objective\ function = \sum_{i=1}^{N} \frac{\left(d_{sim,i} - d_{ref,i}\right)^2}{var\left(d_{sim,i}\right)}, \tag{7.1}$$

where d is the comparable data (bottom-hole pressure in this case), and the subscript i is the temporal index of the data. d_{sim} is the estimation for d in the cluster representative computed by CMG, d_{ref} is the solution from the field data, and $var(d_{sim,i})$ is the variance of $d_{sim,i}$. The result of this computation is shown in Figure 7.9. Cluster 10 produces the least deviation from the injection data, and should thus is selected as the posterior ensemble.

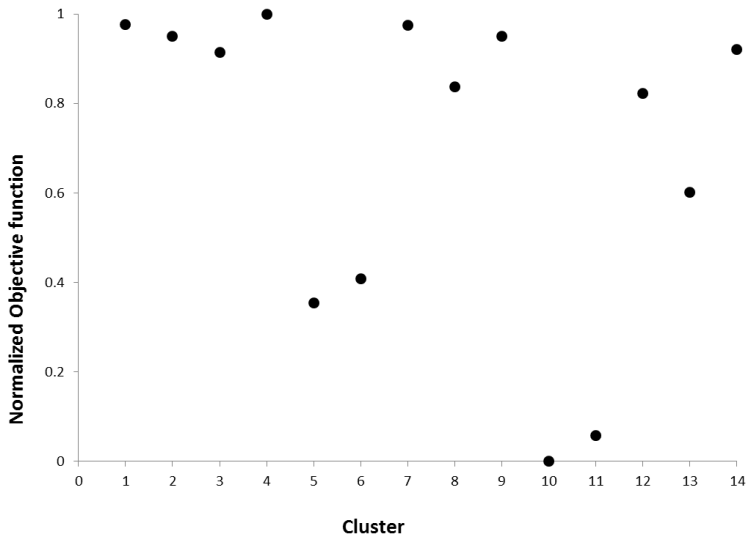

Figure 7.9: Normalized objective function values for 14 clusters. Based on injection data only, Cluster 10 should be selected as the posterior ensemble

To determine whether model selection constrained solely to well data is sufficient, we examine the ensemble mean permeability field for cluster 10 shown in Figure 7.10. The model set does a satisfactory job of reproducing the spatial distribution of permeability. There is a high permeability region close to well KB-502, which might explain the rapid migration to abandoned well KB-5. Additionally, there are no streaks connecting wells KB-502 and KB-503 to the higher elevation regions near the center. The models are however unable to reproduce the orientation of the migration pathways observed in the field using tracer tests and surface deflection measurements. The general orientation of permeability in the ensemble mean is E-W, in contrast to the NW-SE orientation observed in the field. The orientation of the main migration pathways is consequential in predicting the destination of injected CO_2; in the next section, we examine whether the incorporation of surface deflection data helps to predict the correct orientation of the permeability field.

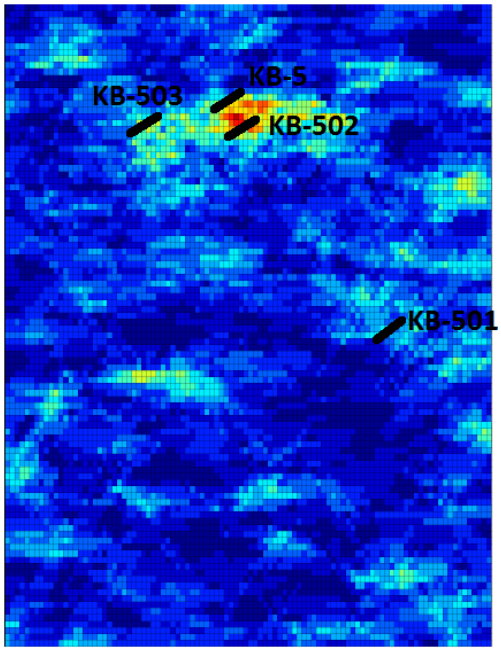

Figure 7.10: Ensemble mean permeability of the resulting models

7.6 Cluster Selection by Combining Injection and Surface Deflection Data

We now perform cluster selection by matching both the well data and the surface deformation measurements. Our goal is to discern whether the incorporation of geomechanical information can produce a better representation of the field geology, by selecting models that will predict field observations in terms of spatial distribution of permeability, as well as the orientation of the permeability streaks. As discussed earlier, we only use information prior to December 2006 (when the first remote sensing data was acquired) for the history match. To select the best cluster, we modify the objective function used in Equation 7.1.

$$Objective\ function = r \cdot \sum_{i=1}^{N} \frac{\left(d_{sim,i} - d_{ref,i}\right)^2}{var\left(d_{sim,i}\right)} + (1-r) \cdot \sum_{j=1}^{N} \frac{\left(V_{sim,j} - V_{ref,j}\right)^2}{var\left(V_{sim,j}\right)}, \qquad (7.2)$$

where d is the comparable well data (bottom-hole pressure), V is the vertical displacement, the subscript i is a temporal index, and the subscript j is a spatial index. The subscript sim signifies the estimation computed by CMG, the subscript ref is the solution from the field

data, and var is the variance. r (used as 0.5 here) is an optional weighting parameter chosen by the modeller to apply preferential weighting to either the well data or the surface deformation. The result of this computation, normalized from 0 to 1 for 14 clusters is shown in Figure 7.11.

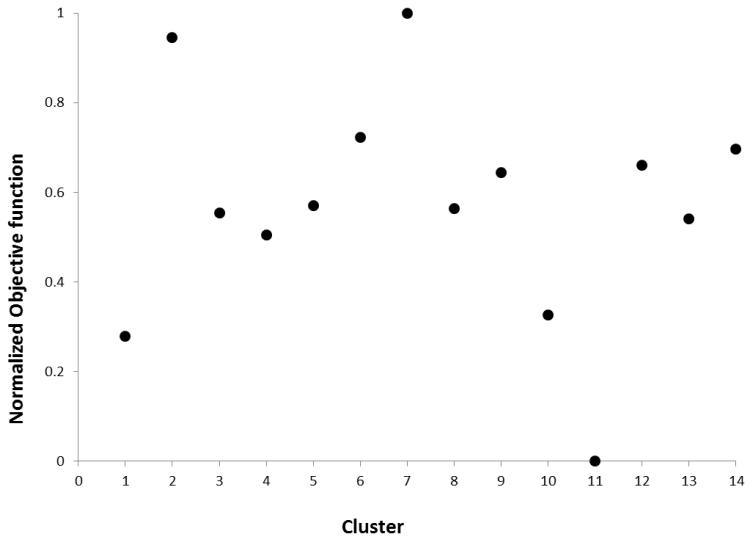

Figure 7.11: Normalized objective function values for 14 clusters. Cluster 11 is selected

To validate the results, we now analyze the posterior model set to ensure that it adequately predicts the field observations as stated earlier in the chapter. Sample models along with the ensemble mean from the selected cluster are shown in Figure 7.12 (a) and (b).

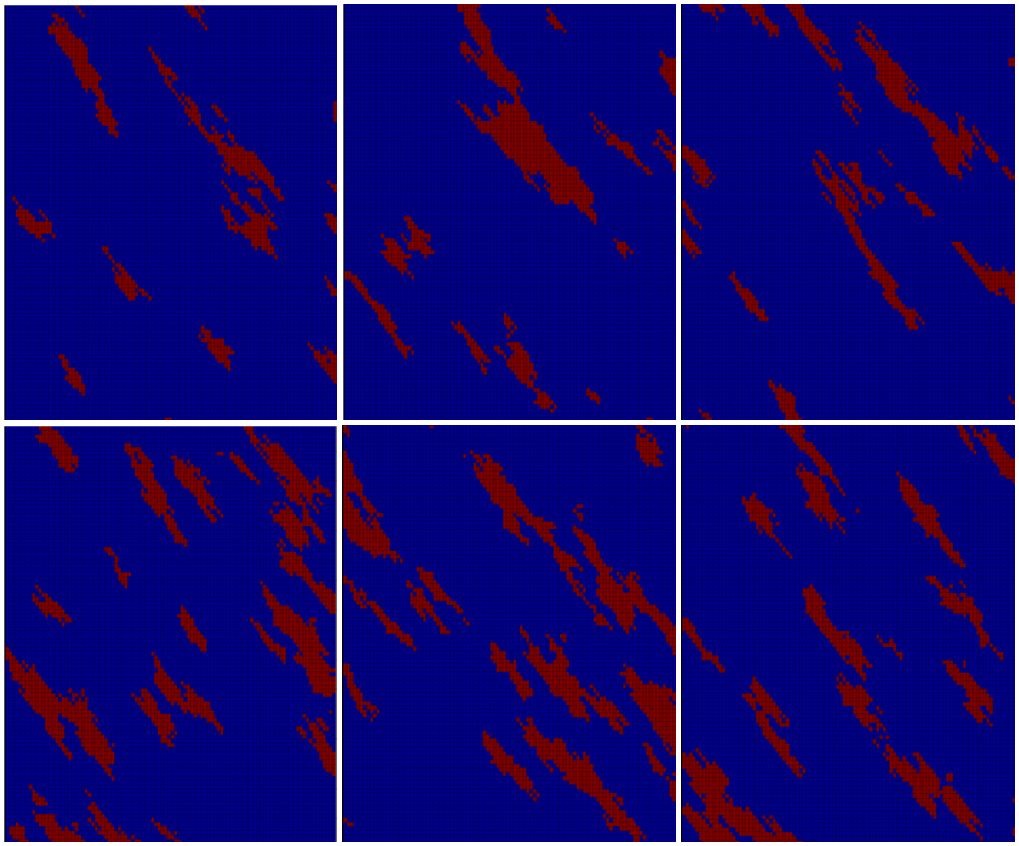

(a)

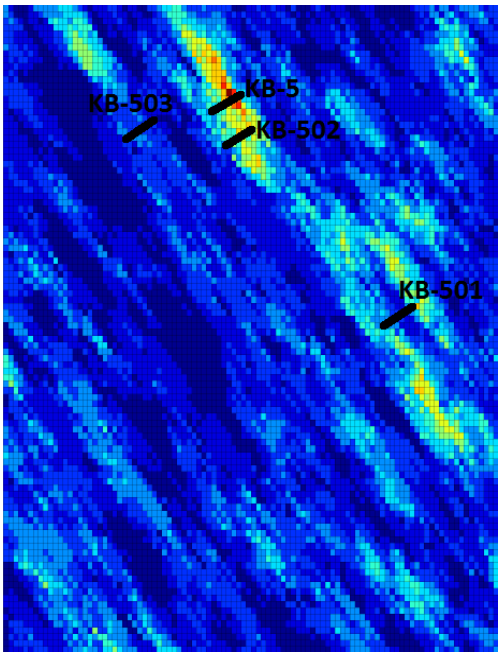

(b)

Figure 7.12: (a) Sample models from the selected cluster (b) Ensemble mean of the permeability field

Most of the models in the selected cluster contain permeability streaks that run along the NW-SE direction, which corroborates field observations. It is evident that the algorithm, when complemented with surface deformation data, is able to discriminate and select models that conform to field observations in terms of orientation.

We now focus of the spatial distribution of the permeability streaks. As mentioned earlier in the chapter, regulators, using tracer tests, observed the arrival of CO_2 at an abandoned well KB-5, just northwest of injector KB-502 (in the down-dip direction) at a time much earlier than expected. Since it was already known at the time that the formation contained fractures and faults that could dominate flow, the explanation for the early arrival of CO_2 was that one of such fractures connected the two wells. It is clear from examining the mean permeability field in Figure 7.12(b), that the posterior ensemble supports this reasoning. There is a high permeability streak that runs directly along wells KB-5 and KB-502, which means that most models in the selected cluster exhibit high permeability features in that vicinity.

Finally, it was observed from field measurements that some of the injected CO_2 plume from KB-502 and KB-503, instead of flowing up dip towards the producer wells, migrated northwest away from the center of the reservoir. This would happen if the wells were drilled close to fractures that were connected to areas away from the producers. Additionally, there should be no significant migration pathways or fractures connecting the wells to regions in the center where the topography is higher. To visually analyze if the models represent such a scenario, the mean permeability field is shown again in Figure 7.13, this time emplaced in a map showing the spatial variations in topography. While there are still some high permeability streaks present in the center, the streaks are preferentially distributed in regions away from the center. Moreover, there are no visible fractures that directly connect wells KB-502 and KB-503 to the regions of higher elevation in the center of the grid.

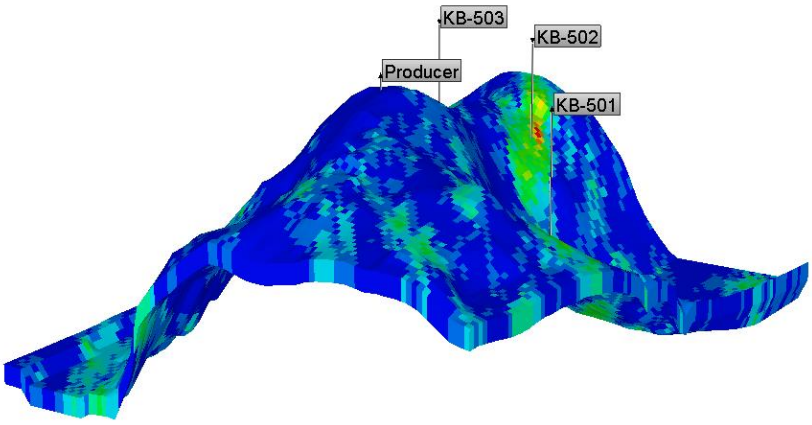

Figure 7.13: Ensemble mean of the permeability field shown superimposed on the topography of the reservoir

It is instructive to compare the prediction from the posterior ensemble for surface deflection for the period after the history match and compare those predictions to the field observations at the corresponding time. We compare the full physics solution of surface deformation for the selected models to the surface deflection measured by InSAR in 2008. Figure 7.14 shows the ensemble mean of the predicted surface deformation solution obtained by CMG and the actual measurements obtained in the field. We can see that the predictions from the selected models reproduce the field observations to a reasonable extent.

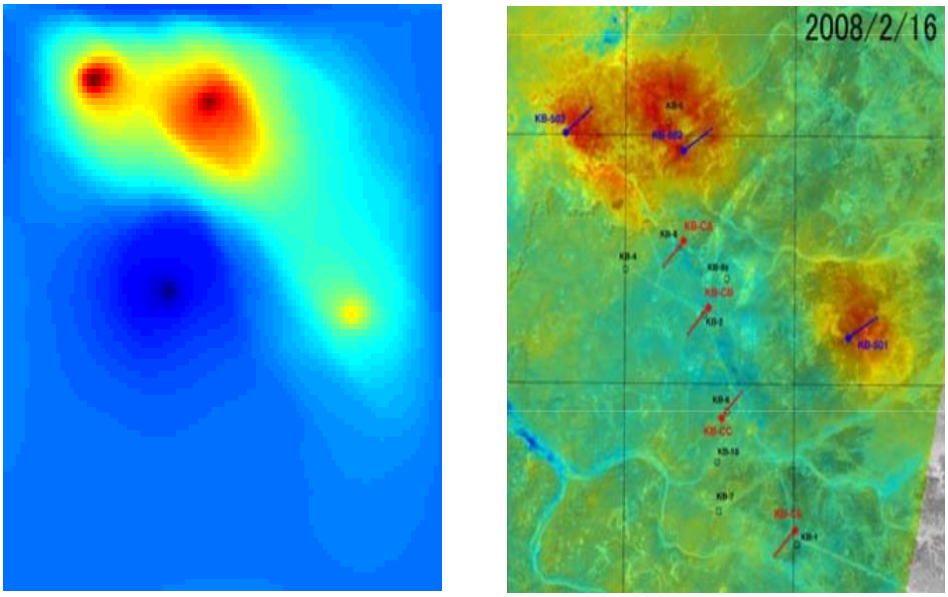

Figure 7.14: Ensemble mean of the predicted surface deformation (left) with the observed surface measurements (right) [Onuma et al., 2008]

7.7 Chapter Summary

In this chapter, we demonstrated the application of the model selection algorithm to the history matching of a CO_2 sequestration field at In Salah, Algeria. We presented the results by matching using (1) only injection data, and (2) a combination of well data and surface deflection measurements. It was seen that the incorporation of the surface deflection data imposed an additional constraint on the geology of the posterior of model set. Validation of the scheme was done by examining the geology of the selected models. It was observed that the selected models conform to the field observations in terms of spatial distribution and orientation of the migration pathways. In Chapter 8, we provide a summary of this project, and offer some recommendations for future work and improvements.

CHAPTER 8: SUMMARY AND CONCLUSIONS

We implemented a history matching scheme to select models from an initial suite of candidate models for predictive purposes during CO_2 sequestration. In addition to being more representative of the reservoir in question, the selected models should exhibit similar geologic characteristics, and thus produce forecast with reduced uncertainty.

We started by generating candidate models that have been constrained based on prior knowledge, but retain some variability in the geology and structure of the reservoir; these models constitute the prior ensemble. We recognized the need to develop programs to produce a fast approximation of the flow and geomechanics response for all the candidate models. This resolved the problem of having to invoke a full physics simulator for numerous models in the prior ensemble.

To approximate the flow response, we developed a particle tracking proxy to simulate the migration of the CO_2 plume in the reservoir. This proxy was able to reproduce results from full physics simulators with reasonable accuracy. To ensure that buoyant effects of the plume were well represented by the proxy, we attached a calibration factor to the gravity term in the proxy formulation. Because of our emphasis on efficiency of execution, it might be prudent to develop a scheme to automatically tweak the calibration factor to achieve desired results.

To approximate the geomechanics, we presented the formulation of the finite element discretization of the stress analysis problem, and implemented an FEM solver to predict the surface deformation response for the candidate models. We employed the explicit coupling scheme due to its advantages in lower computational expense, and greater flexibility in the choice of simulators. A module was created in MATLAB to handle the handling and transfer

of information between the particle tracking proxy and the FEM solver in a fully automated manner.

Multidimensional scaling and k-means clustering algorithms were effective in projecting model responses onto lower dimensional spaces, and grouping the models into clusters based on proximity in space. We showed that this scheme was adequate to discriminate models based on geologic characteristics, and that the models within each cluster exhibited similar geology close to the CO_2 injection wells.

Models that were most representative of the geology within each cluster were chosen, and we illustrated a method to select the best-fit cluster by the minimization of an objective value proportional to the error in the predicted forecast from the representative models.

We demonstrated the application of the overall model selection scheme to two cases: (1) a synthetic case, in which the full physics solution for a reference model was used as data for history matching, and (2) a field case using data and observations from the In Salah CO_2 storage project in Algeria. In both cases, we showed that the model selection algorithm was capable of generating a posterior model ensemble that was representative of the actual reservoir while reducing the uncertainty in the geological characteristics of the models.

Future Work

- In addition to validating with CMG, the stress analysis problem can be validated by inputting the observed pressure changes into a stress solver, such as Abaqus®. The rationale behind this exercise is that for any given situation, it would be useful to compare the accuracy of the approximations between the flow and geomechanics proxies. That is, we would often like to know whether the majority of the error in the proxy solution originates from the particle tracking proxy or the FEM solver.

- We also seek to implement the entire model selection scheme in a fairly automated, user-friendly, computational framework. Due to the emphasis on speed and efficiency, it is preferred to develop this program with an in-built capability of operating in a parallel computing structure. The ability to utilize parallel computing will enable a user to run simulations for different models in the prior ensemble at the same time, thereby significantly reducing the overall time required to predict the response for multiple models.
- We will explore more mathematically-sound avenues for calculating the pressure response in the prior ensemble. Currently, the pressure solution is developed from a radial solution around each particle in the saturation map. This could often lead to inaccuracies, especially in cases where the permeability field is strongly heterogeneous. Moreover, this implicitly suggests that model clustering is indirectly dominated by the flow response from the proxy. We have investigated different methods for this purpose, an example of which is the fast marching method. This method offers an upwinding solution to the Eikonal equation derived from the single phase diffusivity equation. Zhang et. al [2014] employed this technique to derive the propagation time of the pressure front in shale gas reservoirs. However, because we seek a two-phase solution, we are precluded from utilizing this method. An effort to derive a fast marching solution to the two-phase case will result in complexities that approach commercial simulators in terms of computational expense.

REFERENCES

Aanonsen, Sigurd I., Geir Nævdal, Dean S. Oliver, Albert C. Reynolds, and Brice Vallès. "The Ensemble Kalman Filter in Reservoir Engineering--a Review." *SPE Journal* 14.03 (2009): 393-412. Web.

Amirlatifi, Amin. "Coupled Geomechanical Reservoir Simulation." Dissertation. Missouri U of Science and Technology, 2013. Print.

Bhowmik, Sayantan. *Particle Tracking Proxies for Prediction of CO2 Plume Migration within a Model Selection Framework*. Dissertation. The U of Texas at Austin, 2014. Print.

Bhowmik, Sayantan. "Predicting the Migration of CO2 Plume in Saline Aquifers Using Probabilistic History Matching Approaches." Thesis. The University of Texas at Austin, 2012. Print.

Bhowmik, Sayantan, Sanjay Srinivasan, and Steven L. Bryant. "Inferring Migration of CO2 Plume Using Injection Data and a Probabilistic History Matching Approach." *Energy Procedia* 4 (2011): 3841-848. Web.

Caers, Jef. "Comparing the Gradual Deformation with the Probability Perturbation Method for Solving Inverse Problems." *Mathematical Geology Math Geol* 39.1 (2007): 27-52. Web.

Caers, Jef. "History Matching Under Training-Image-Based Geological Model Constraints." *SPE Journal* 8.03 (2003): 218-26. Web.

Dean, Rick H., Xiuli Gai, Charles M. Stone, and Susan E. Minkoff. "A Comparison of Techniques for Coupling Porous Flow and Geomechanics." *SPE Journal* 11.01 (2006): 132-40. Web.

Emerick, Alexandre A., and Albert C. Reynolds. "Combining the Ensemble Kalman Filter With Markov-Chain Monte Carlo for Improved History Matching and Uncertainty Characterization." *SPE Journal* 17.02 (2012): 418-40. Web.

Evensen, G. "The Ensemble Kalman Filter for Combined State and Parameter Estimation." *IEEE Control Syst. Mag. IEEE Control Systems Magazine* 29.3 (2009): 83-104. Web.

Evensen, Geir. *Data Assimilation: The Ensemble Kalman Filter*. Berlin: Springer, 2007. Print.

Evensen, Geir. "Sequential Data Assimilation with a Nonlinear Quasi-geostrophic Model Using Monte Carlo Methods to Forecast Error Statistics." *J. Geophys. Res. Journal of Geophysical Research* 99.C5 (1994): 10143. Web.

Gardiner, Crispin W. *Handbook of Stochastic Methods for Physics, Chemistry and the Natural Sciences*. Berlin: Springer, 1990. Print.

Geir, Nævdal, Liv Johnsen, Sigurd Aanonsen, and Erlend Vefring. "Reservoir Monitoring and Continuous Model Updating Using Ensemble Kalman Filter." *Proceedings of SPE Annual Technical Conference and Exhibition* (2003). Web.

Hirsch, L.m., and J.f. Schuette. "Graph Theory Applications to Continuity and Ranking in Geologic Models." *Computers & Geosciences* 25.2 (1999): 127-39. Web.

Hotho, Andreas, Alexander Maedche, and Steffen Staab. "Ontology-based Text Document Clustering." Web. 2002.

Hu, Lin Y. "Gradual Deformation and Iterative Calibration of Gaussian Related Stochastic Models." *Mathematical Geology* 32.1 (2000): 87-108. Web.

Iding, Martin, and Philip Ringrose. "Evaluating the Impact of Fractures on the Long-term Performance of the In Salah CO2 Storage Site." *Energy Procedia* 1.1 (2009): 2021-028. Web.

Inoue, Nelson, and Sergio Fontoura. "Answers to Some Questions About the Coupling Between Fluid Flow and Rock Deformation in Oil Reservoirs." *SPE/EAGE Reservoir Characterization and Simulation Conference* (2009). Web.

Jafarpour, Behnam, and Dennis B. Mclaughlin. "History Matching with an Ensemble Kalman Filter and Discrete Cosine Parameterization." *Comput Geosci Computational Geosciences* 12.2 (2008): 227-44. Web.

Johansen, Kent. *Statistical Methods for History Matching*. Dissertation. Technical U of Denmark, 2008. Print.

Journel, A. G. "Combining Knowledge from Diverse Data Sources: An Alternative to Traditional Data Independence Hypothesis." *Mathematical Geology* 34.1 (2002): 105-07. Web.

Kashib, Tarun, and Sanjay Srinivasan. "Iterative Integration of Dynamic Data in Reservoir Models." *SPE Annual Technical Conference and Exhibition* (2003): n. pag. Web.

Kruskal, J. B. "Nonmetric Multidimensional Scaling: A Numerical Method." *Psychometrika* 29.2 (1964): 115-29. Web.

Lichtner, Peter C., Sharad Kelkar, and Bruce Robinson. "New Form of Dispersion Tensor for Axisymmetric Porous Media with Implementation in Particle Tracking." *Water Resources Research Water Resour. Res.* 38.8 (2002): n. pag. Web.

Longuemare, P., M. Mainguy, P. Lemonnier, A. Onaisi, C. Gérard, and N. Koutsabeloulis. "Geomechanics in Reservoir Simulation: Overview of Coupling Methods and Field Case Study." *Oil & Gas Science and Technology - Rev. IFP Oil & Gas Science and Technology* 57.5 (2002): 471-83. Web.

Mantilla, Cesar A., and Sanjay Srinivasan. "Feedback Control of Polymer Flooding Process considering Geologic Uncertainty." *SPE Reservoir Simulation Symposium* (2011). Web.

Mathieson, Allan, Iain Wright, David Roberts, and Philip Ringrose. "Satellite Imaging to Monitor CO2 Movement at Krechba, Algeria." *Energy Procedia* 1.1 (2009): 2201-209. Web.

Mikelić, Andro, and Mary F. Wheeler. "On The Interface Law Between A Deformable Porous Medium Containing A Viscous Fluid And An Elastic Body." *Math. Models Methods Appl. Sci. Mathematical Models and Methods in Applied Sciences* 22.11 (2012): 1250031. Web.

Minkoff, Susan E., C.mike Stone, Steve Bryant, Malgorzata Peszynska, and Mary F. Wheeler. "Coupled Fluid Flow and Geomechanical Deformation Modeling." *Journal of Petroleum Science and Engineering* 38.1-2 (2003): 37-56. Web.

Onuma, Takumi, and Shiro Ohkawa. "Detection of Surface Deformation Related with CO2 Injection by DInSAR at In Salah, Algeria." *Energy Procedia* 1.1 (2009): 2177-184. Web.

Onuma, Takumi, Kinya Okada, and Shiro Ohkawa. "Surface Heave Detection Related with CO2 Injection by DInSAR at In Salah, Algeria." *International Petroleum Technology Conference* (2008): n. pag. Web.

Rousseeuw, Peter J. "Silhouettes: A Graphical Aid to the Interpretation and Validation of Cluster Analysis." *Journal of Computational and Applied Mathematics* 20 (1987): 53-65. Web.

Settari, A., and Dale A. Walters. "Advances in Coupled Geomechanical and Reservoir Modeling With Applications to Reservoir Compaction." *SPE Journal* 6.03 (2001): 334-42. Web.

Settari, Antonin, and Dale Walters. "Advances in Coupled Geomechanical and Reservoir Modeling With Applications to Reservoir Compaction." *Proceedings of SPE Reservoir Simulation Symposium* (1999). Web.

Settari, Antonin, and F.m. Mourits. "*A Coupled Reservoir and Geomechanical Simulation System*." *SPE Journal* 3.03 (1998): 219-26. Web.

Singh, H., Assessing Reservoir Performance and Modeling Risk Using Real Options. Thesis. The University of Texas at Austin, 2012. Print.

Singh, H., and Srinivasan, S. Uncertainty Analysis by Model Selection Technique and its Application in Economic Valuation of a Large Field, *Society of Petroleum Engineers*. (2013). Web.

Singh, H., Scale up of Reactive Processes in Heterogeneous Media. Dissertation. The University of Texas at Austin, 2014. Print.

Singh, H., and Srinivasan, S., Some perspectives on Scale-up of Flow and Transport in Heterogeneous Media. Gussow 2014, *Canadian Society of Petroleum Geologists* (2014a). Web.

Singh, H., and Srinivasan, S., Scale up of Reactive Processes in Heterogeneous Media – Numerical Experiments and Semi-analytical Modeling. *Society of Petroleum Engineers* (2014b). Web.

Tavakoli, Reza, Sanjay Srinivasan, and Mary F. Wheeler. "Rapid Updating of Stochastic Models by Use of an Ensemble-Filter Approach." *SPE Journal* (2013). Web.

Terzaghi, K. (1936) "The shear resistance of saturated soils." Proceedings for the 1st. International Conference on Soil Mechanics and Foundation Engineering (Cambridge, MA), 1, 54 -56.

Zafari, Mohammad, and Albert Coburn Reynolds. "Assessing the Uncertainty in Reservoir Description and Performance Predictions With the Ensemble Kalman Filter." *SPE Journal* 12.03 (2007): 382-91. Web.

Zhang, Yanbin, Neha Bansal, Yusuke Fujita, Akhil Datta-Gupta, Michael J. King, and Sathish Sankaran. "*From Streamlines to Fast Marching: Rapid Simulation and*

Performance Assessment of Shale Gas Reservoirs Using Diffusive Time of Flight as a Spatial Coordinate." SPE Unconventional Resources Conference (2014). Web.

Zienkiewicz, O. C., A. H. C. Chan, M. Pastor, B. A. Schrefler, and T. Shiomi. *Computational Geomechanics with Special Reference to Earthquake Engineering*. Chichester: Wiley, 1999. Print.